Master thesis and internship[BR]- Master's thesis : Rebuilding Optical Emission Spectroscopy Measurements in a Low Density Plasma Facility using a Collisional-Radiative Model[BR]- Integration Internship : von Karman Institute for Fluid Dynamics

Auteur : Fontaine, Bruno
Promoteur(s) : Hillewaert, Koen
Faculté : Faculté des Sciences appliquées
Diplôme : Master en ingénieur civil en aérospatiale, à finalité spécialisée en "aerospace engineering"
Année académique : 2022-2023
URI/URL : https://www.vki.ac.be/index.php/facilities-other-menu-148/50-research-and-consulting/facilities/plasma
http://hdl.handle.net/2268.2/17845

Master's Thesis
for the degree of Master of Science in Aerospace Engineering

University of Liège — School of Engineering

Rebuilding Optical Emission Spectroscopy Measurements in a Low Density Plasma Facility using a Collisional-Radiative Model

---

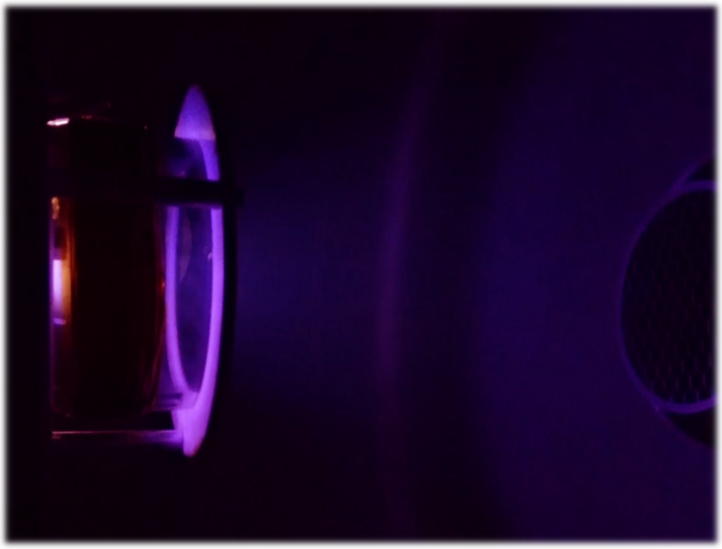

Supervisors

Professor Koen Hillewaert
University of Liège

Professor Thierry Magin
von Karman Institute for Fluid Dynamics

Author

Bruno Fontaine

Academic year 2022–2023

Abstract

In recent years, Air Breathing Electric Propulsion (ABEP) has emerged as a promising technology for the efficient exploitation of Very Low Earth Orbits (VLEO) for Earth observation satellites. In the context of the development and performance assessment of this technology, the DRAG-ON facility (Dual-chamber for RArefied Gases and ON-ground testing) was constructed at the von Karman Institute for Fluid Dynamics. It has the purpose to replicate on-ground the rarefied flow conditions encountered by a satellite flying at VLEO, in order to test the efficiency of intakes specifically designed for ABEP. This flow is generated by a Particle Flow Generator (PFG), which generates a partially ionized plasma plume with ions reaching orbital speeds.

The present work implements a first iteration of a non-invasive diagnostics method for the characterization of the rarefied plasma encountered in DRAG-ON, specifically for the PFG running on Argon gas. The employed method is Optical Emission Spectroscopy (OES), complemented with a Collisional-Radiative (CR) model for the prediction of emission line intensities in chemical non-equilibrium conditions, based on a set of plasma parameters. The main objectives are to assess the degree of non-equilibrium of the plasma in DRAG-ON, and to provide insight on how to improve the fidelity of the CR modelling.

The work is divided into three main parts. The first consists of the construction of the CR model and the identification of the key plasma parameters influencing the relative populations of the energy levels of Argon. The electron temperature and density stand out as the parameters of interest. The second part corresponds to the experimental measurement of the radiative signature of the plasma in the DRAG-ON facility, and the extraction of emission line intensities related to Argon atomic transitions. The last step in the developed methodology consists of comparing the experimental and predicted line intensities. Through this comparison, the electron temperature and density leading to the minimum discrepancy between the experimental and predicted results can be found.

The developed method is applied to early experimental results. This first experiment allowed to identify the sensibilities of the experimental intensities to the setup, showing that the robustness of the setup can be improved with automatization. The results obtained for the best fitting parameters between the CR model predictions and experimental intensities show the highly out-of-equilibrium plasma conditions encountered in the facility. The apparent overestimation of the plasma parameters also suggests that the usual assumption of a Maxwellian electron energy distribution function might not be applicable to the studied rarefied plasma. The results of this work lead to the construction of a roadmap to refine the method for higher fidelity results and more robustness in the experimental setup.

Keywords: Optical Emission Spectroscopy — Collisional-Radiative Model — Low density plasma — Electron temperature — Electron density — Non-equilibrium

Acknowledgements

Upon the termination of this work, I would like to express my sincere gratitude towards Pr. Thierry Magin for giving me the opportunity to carry out this project at the von Karman Institute in such a unique experimental facility, but also for his guidance, expertise and constructive feedback given throughout the semester. I would also like to express my gratitude to Pr. Koen Hillewaert for his interest in this work, as well as his insightful questions and advice.

I would also like to thank Pedro Jorge for his valuable suggestions, guidance and support given all along this work. Our long discussions have greatly helped me grasp the concepts, and have largely contributed to the construction and review of this project. I am equally grateful to Damien Le Quang for his precious help with the experimental setup and calibration method, as well as his extensive advice on the processing and interpretation of the experimental results. Many thanks to the rest of the RPF team for the interactions which, every time, lead to new learnings and perspectives.

I would like to take this opportunity to recognize the contribution of all professors and teachers met along the way.

Last but not least, I reserve the most heartful thanks to my friends, family and loved ones for their love and support, and for the inspiration they all have been for my entire life. Merci pour tout ce que vous représentez.

Contents

List of Symbols

S.I. (International System of Units) units and abbreviations for units are used in this work, except if stated otherwise. For quantum energy values, the electron-volt [eV] is used as a convenient alternative. The same unit is used for electron temperatures.
Vector quantities are denoted by bolded symbols.

Acronyms

ABEP	Air-Breathing Electric Propulsion
AETHER	Air-breathing Electric THrustER
BSR	B-Spline R-matrix
CCD	Charged Coupled Device
CR	Collisional-Radiative
DRAG-ON	Dual-chamber for RArefied Gases and ON-ground testing
n-D	n dimensions
EEDF	Electron Energy Distribution Function
EO	Earth Observation
ESA	European Space Agency
GOCE	Gravity field and steady-state Ocean Circulation Explorer
HITRAN	HIgh-resolution TRANsmission molecular absorption database
HWHM	Half width at half maximum
JAXA	Japan Aerospace Exploration Agency
LIF	Laser Induced Fluorescence
ND	Neutral Density filter
NIST-ASD	National Institute of Standards and Technology — Atomic Spectral Database
OES	Optical Emission Spectroscopy
PFG	Particle Flow Generator
RF power	Forward power minus Reflected power
RMS	Root Mean Square
STD	Standard Deviation
VKI	von Karman Institute for Fluid Dynamics
VLEO	Very Low Earth Orbit

Roman symbols

a	Distance	[m]
A_{ul}	Einstein-A coefficient for emissions	[s^{-1}]
A	Generic constant	
b	Impact parameter	[-]

B	Magnetic field	[T]
B_{lu}	Einstein-B coefficient for absorption	[s^{-1}]
c	Speed of light	[m/s]
c_s	Speed of sound	[m/s]
C_i	Wavelength calibration coefficient of the spectrometer	[nm/pixel^i]
D	Diameter	[m]
Da	Damköhler number	[-]
e	Electron charge	[C]
E	Energy	[J]
$\mathcal{E}$	Electric field	[V/m]
f	Distribution function in the phase space	[s^3/m^6]
f^v	Distribution of speeds	[s/m^4]
f^E	Distribution of thermal kinetic energy	[$J^{-1}\cdot m^{-3}$]
$\hat{f}$	Normalized distribution of speeds/energy	[J^{-1}] or [s/m]
F	Force	[N]
g	Degeneracy	[-]
G	Gaussian constant	
h	Planck's constant	[Js]
H	Optical setup response	[-]
i	Current	[A]
I_λ	Spectral radiance	[$W\cdot sr^{-1}\cdot m^{-3}$]
I	Emission line intensity	[a.u.]
$\hat{I}$	Normalized emission line intensity	[-]
J	Total angular momentum quantum number	[-]
k_B	Boltzmann constant	[J/K]
Kn	Knudsen number	[-]
$\mathcal{K}^{rad}$	Radiative decay rate coefficient	[s^{-1}]
$\mathcal{K}^{ee}$	Electron impact rate coefficient	[m^3/s]
l	Orbital angular momentum quantum number	[-]
l^*	Total orbital angular momentum quantum number	[-]
L	Length	[m]
$\mathcal{L}$	Set of usable, comparable lines	
m	Mass	[kg]
m_l	Magnetic quantum number	[-]
m_s	Spin quantum number	[-]
m_s^*	Total spin angular momentum quantum number	[-]
n	Number density	[m^{-3}]
n_e^*	Electron number density minimizing ξ	[m^{-3}]
$\mathcal{N}$	Number of particles	[-]
N	Number of objects in a set	[-]
N_A	Avogadro number	[mol^{-1}]
p	Principal quantum number	[-]
$\#p$	Pixel index	[-]
P	Pressure	[Pa]
q	Electric charge	[C]
r_L	Larmor radius	[m]

r_m	Distance of closest approach for particle collisions	[m]
r	Position, distance, radius	[m]
$\hat{r}$	Normalized radial position	[-]
RH	Relative humidity	[-]
s	Standard deviation of the Gaussian fitting	[nm]
$\mathcal{S}$	Set of species included in the CR model	
t	Time	[s]
t^*	Integration time	[s]
T	Temperature	[K]
T_e^*	Electron temperature minimizing ξ	[K]
T_λ	Spectral transmittance	[-]
U	Potential energy	[J]
v	Velocity	[m/s]
V	Electrostatic potential	[V]
x, y, z	Spatial coordinates	[m]
X	Molar fraction	[-]
Z	Number of positive charges $\lvert e \rvert$	[-]
$\hat{z}$	Normalized vertical position	[-]

Greek symbols

α_λ	Spectral absorption coefficient	[m^{-1}]
γ	Design parameter of a blazed grating	[rad]
Γ	Particle flux	[$\mathrm{m}^{-2}\cdot\mathrm{s}^{-1}$]
δX	Uncertainty on variable X	
ε	Relative error	[-]
ε_0	Vacuum permittivity	[F/m]
η	Fitting coefficient for the Arrhenius form	[-]
θ, ϕ	Spherical coordinate agles	[rad]
λ	Wavelength	[m]
λ_D	Debye length	[m]
$\overline{\lambda}$	Mean free path	[m]
μ	Reduced mass	[kg]
μ_0	Vacuum magnetic permeability	[$\mathrm{N/A}^2$]
ν	Frequency	[s^{-1}]
ξ	Objective function for the comparison of CR model to experiment	[-]
ξ'	Alternative objective function	[-]
σ	(Total scattering) cross section	[m^2]
σ_d	Differential scattering cross section	[m^2]
χ	Collision deflection angle	[rad]
ω_p	Plasma frequency	[rad/s]
ω_c	Cyclotron frequency	[rad/s]
$\dot{\omega}$	Net production rate	[$\mathrm{m}^{-3}\cdot\mathrm{s}^{-1}$]

Subscripts

b	Backward (for rate coefficients)
coll	Value relative to collisional processes
coil	Value relative to the PFG's coil
CR	Value computed with the Collisional-Radiative model
e	Value relative to electrons
eq	Equilibrium value
exp	Experimental value
f	Forward (for rate coefficients)
HS	Value computed under the hard sphere model assumption
H_2O	Value relative to water vapor
i	Value relative to ions
i, j	Index
mp	Most probable
r	Reaction index
rms	Root mean square
n	Value relative to neutrals
p	Value relative to a photon
t	Value relative to the transparent tube
u, l	Upper and lower energy levels
x, y, z	Value relative to spatial coordinates
$\perp$	Perpendicular

CHAPTER 1

Introduction

In the process of selecting the optimal orbit for Earth observation satellites, mission planning engineers must strike a compromise between the numerous advantages of proximity to Earth's surface, and the cost that comes with the increasing drag encountered at low altitudes. This compromise implies that Very Low Earth Orbits (VLEO), or orbits with altitudes lower than 400 km, remain largely unexploited. Several instances of VLEO satellites have however shown the exceptional results that can be obtained at low altitudes, such as GOCE (Gravity field and steady-state Ocean Circulation Explorer) [1, 2], launched by the European Space Agency (ESA) in 2009. Thanks to its exceptionally low altitude of 260 km, it provided measurements of the static gravity field of our planet with unprecedented precision. The mission was a success, but because of the required low orbit, its end-of-life was ultimately determined by the termination of the onboard 40 kg of propellant, which was consumed continuously during the 4 years duration of the mission for drag compensation.

Now, what if the remaining air at VLEO could be used to the advantage of these missions, instead of being their main drawback? Air Breathing Electric Propulsion (ABEP), also called RAM-EP in the literature, is an emerging concept that has the objective of collecting the incident rarefied air and using it as propellant for an ion thruster. This allows to continuously compensate drag, while not relying on a limited source of propellant, therefore untying the current link between the lifetime of the mission and stored propellant.

1.1 Advantages and challenges of flying at VLEO

Earth observation satellites have impactful applications, including environmental, agricultural, meteorological, maritime, and disaster monitoring. ABEP would enable to enhance the performance of these missions by making VLEO accessible for long-term missions. The advantages of low orbits include [3]

- **Enhanced resolution for imaging**, or reduction of the optical payload required for a similar resolution. The effectiveness of VLEO for imaging was shown in practice by the Super Low Altitude Test Satellite (SLATS) "Tsubame" from the Japan Aerospace Exploration Agency (JAXA) [4], launched end of 2017. This test satellite gave promising results for reaching good ground resolutions with small optical systems by exploiting VLEO to its limits, with an orbital altitude between 271.5 km and 167.4 km.
- **Improved pointing accuracy:** Angular uncertainties in the satellite's attitude and position have a lower impact on the pointing accuracy, since the distance between the camera and the target is smaller than at higher orbit. This reduces the stress on the design of the attitude control system.

- **Aerodynamic attitude control:** The aerodynamic forces can be used to the advantage of the attitude control of the spacecraft, with fins for example, for an aerodynamic attitude control. The GOCE satellite used such fins for enhanced stability.

- **Improved radiometry:** The signal power density varies with $1/d^2$, with d [m] the distance between the source and detector. At low altitudes, less signal power is therefore lost, lowering the need for powerful emitters and large antennas.

- **Low latency:** The proximity to the ground also lowers the time it takes for a signal to be transmitted from orbit to the ground, increasing the potential for fast satellite communication with constellations. This, along with the previous point, has been shown in a study conducted by ESA's programme of Advanced Research in Telecommunications Systems (ARTES) [5], showing that VLEO has the potential of supporting data rates of the order of Gigabits per second, with only a few Watts of power.

- **Low radiation levels:** VLEO satellites are protected by the Earth's magnetic sphere, lowering the radiation levels that can damage hardware or, for manned missions, be a health hazard.

- **Fulfillment of deorbiting requirements:** In recent years, space agencies have set standards for the decommissioning of satellites, to avoid the accumulation of space debris that can put at risk future missions. The standard rule is to endure deorbiting within 25 years after the termination of the satellite's mission. The higher the orbit, the lower the drag thus the longer the lifetime of the satellite in its orbit. Active deorbiting systems therefore have to be implemented, increasing the cost of the mission. VLEO satellites do not have this problem, as the lifetime of a satellite at these altitudes is of the order of a few days to a few weeks, depending on the altitude and geometry of the satellite, totally clearing these altitudes of space debris.

- **Low risk of collision:** This advantage of VLEO is a direct consequence of the previous point. Since the orbits naturally decay quickly, there is no accumulation of space debris therefore highly reducing the risk of collision.

- **Reduction of launch price:** Due to the lower altitudes to reach, the kinetic energy to give per unit mass is lower at VLEO than at conventional orbits. This reduction of launch price however only holds if the mass of the spacecraft is not increased by the additional mass of propellant needed at low orbit.

On the other hand, the remnants of atmosphere at these altitudes have been the main drawback for the exploitation of VLEO. The aerodynamic drag dominates any other aspect of the satellite design, greatly complicating the realization of such projects. The continuous drag, of the order of a few millinewtons, has to be continuously compensated by thrust. This either leads to very short mission lifetimes if this thrust is not provided (a few days or weeks, as for early satellites such as Sputnik), or to the necessity of large amounts of propellant and capable propulsion systems (such as the 40 kg of propellant consumed during the GOCE mission). This last option greatly increases the launch mass thus cost.

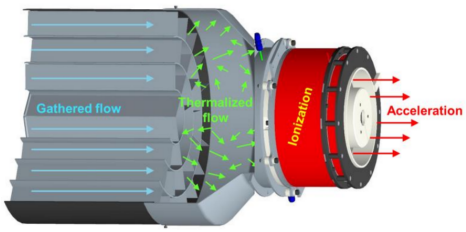

Figure 1.1: ABEP system design by SITAEL, from [8]

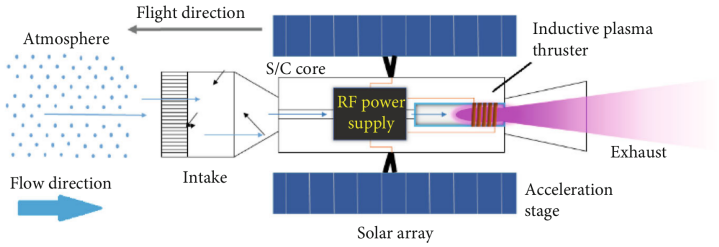

Figure 1.2: ABEP system design by DISCOVERER, from [7]

Emergence of ABEP as a research subject

The continuous improvements in ion thrusters efficiency steadily lower the altitude limit for commercially viable spacecraft, but only a radical change in the approach for spacecraft propulsion design can effectively make VLEO accessible in the long run. ABEP provides a solution that has the potential of completely changing the market. In addition to all the advantages cited in Section 1.1, the current strong correlation between the amount of propellant that the mission can afford to bring onboard and the lifetime of the mission would be eliminated, extending the duration of VLEO missions.

Because of its revolutionary potential, ABEP has become an active research subject in recent years. In Europe alone, two major research projects are being funded by the European Union's Horizon 2020 research and innovation programme to investigate different designs of ABEP systems: the Air-breathing Electric THrustER (AETHER) project [6] and the DISCOVERER project [7]. The design proposed by SITAEL, in the context of the AETHER project, is represented in Figure 1.1, and the one designed for DISCOVERER is illustrated in Figure 1.2. The main difference between the two approaches is the thruster, which is a Hall thruster in the case of AETHER, and an Inductive Plasma Thruster for the DISCOVERER project.

Several comprehensive reviews have been carried out to assess the maturity of ABEP [9, 10, 11]. Although the technology is promising, a lot of research still has to be done to tackle the challenges that come with the design of such a system, concerning both the intake and utilization of atmospheric propellant in ion thrusters.

Concerning the intake, the design is driven by the low densities encountered at VLEO. The incoming air is in free molecular flow, meaning that the flow is governed by gas/surface interactions. Molecules reflect on the intake's surfaces, making it hard to efficiently collect air. Designs have been tested numerically with direct Monte Carlo simulations [12], predicting intake efficiencies of about 25% for diffusive intakes such as the one represented in Figure 1.1. The efficiencies however still have to be assessed experimentally. For this purpose, the DRAGON facility (Dual-chamber for RArefied Gases and ON-ground testing) was constructed at the von Karman Institute (VKI), as part of the AETHER project.

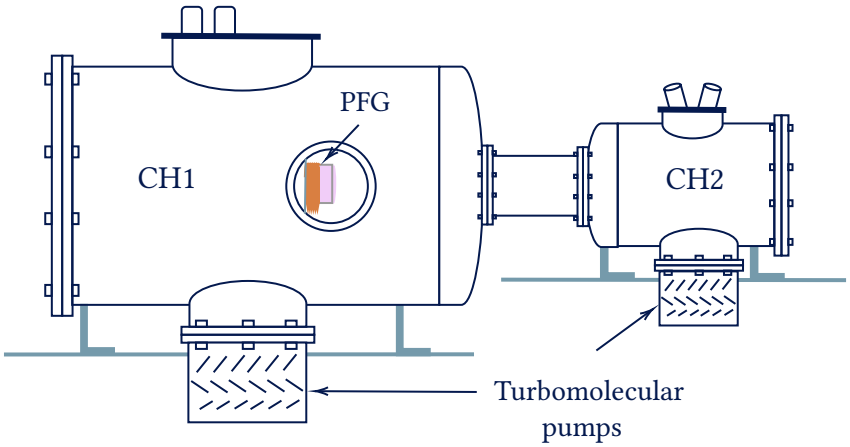

Figure 1.3: Schematic of the DRAG-ON facility's vacuum chambers and main components (side view)

1.2 The DRAG-ON facility

The DRAG-ON facility was commissioned at the start of 2023. It is designed to reproduce, on ground, the conditions of the high speed rarefied flow encountered by a satellite flying at VLEO. The flow is generated by a Particle Flow Generator (PFG). It generates a particle flow at about 8 km/s, corresponding to the orbital speeds at VLEO. To reach such speeds, the particles are ionized in the PFG, and accelerated with an electric field. The resulting plume is therefore in the plasma state of matter. The PFG is designed to run both on Argon and oxygen. To best simulate the flow conditions, the pressure in the facility is pumped down to pressures of the order of 10^{-3} Pa. At these pressures, the density inside the facility is low enough to be in the free molecular flow regime, meaning that there are only few collisions between the particles.

The rarefied atmospheric plasma flow encountered in DRAG-ON makes it a unique facility. Because of its recent commissioning, the particle flow generated by the PFG still has to be characterized. This characterization process is carried out both with invasive (electrostatic probes) and non-invasive (spectroscopy) diagnostics, complemented by numerical simulations. The present work contributes to the characterization process of the plasma flow with non-invasive diagnostics. The objectives of the thesis are given in more detail in Section 1.4.

In this section, we present the main components of the DRAG-ON facility. The installation consists of two chambers (CH1 and CH2), as shown in Figure 1.3. They are linked by a duct, which hosts the ABEP intake to be tested. The vacuum chambers were manufactured by Pfeiffer Vacuum [13], as well as the pumping system and pressure sensors.

Materials

The chambers are made out of stainless steel, because of its high corrosion resistance, and its low outgassing rate. Outgassing can indeed be a problem for high or ultra high vacuum chambers. The more porous a material is, the more gas it contains. Once very low pressures are reached inside the chamber, the gas contained in the material can contaminate the chamber with undesired chemical components. To lower further the outgassing rate, the surfaces are

fine glass bead blasted, as form of surface treatement, sealing any microscopic crack.

Pumping system

The pumping system is composed of two stages of pumping. The first stage contains a *rotary vane mechanical pump*, pumping down both chambers from atmospheric pressure to approximately 1 Pa. This pump consists of a rotor in a rotary motion in a stator. The rotation motion creates a temporary vacuum, higher than that of the chamber, therefore pulling gas in the rotating system. Further in the rotation, that pocket of gas is pushed out of the pump, leading to a decrease in the pressure inside the chamber it is pumping from.

Two *turbomolecular pumps* (one for each chamber) do the additional work of bringing the chambers down to ultra-high vacuum. They can only work once the rotary vane pump has already lowered the pressure significantly (down to 0.1 Pa), because in order to work efficiently, the mean free path needs to be larger than the distance between the pump's blades for the particle motion to be governed by the collisions with the blades, and not with each other. These pumps work by repeated collisions between the blades and particles. Since the blades are moving, they transfer momentum to the particles at each collision, directed toward the next stage of the chamber. With enough particle-blade collisions, there is a net flow rate towards the exit of the pump, therefore reducing the chamber's pressure. This can only work if most collisions are between blades and particles, and not between particles themselves, justifying the need for the rotary vane pump to carry out a first pressure decrease before turning on the turbomolecular pumps. They are capable of reaching very low pressures: the ones installed at in the DRAG-ON facility can reach an ultimate pressure of 10^{-6} Pa. These extremely low pressures allow to reach free molecular flow in the entire vacuum chamber, with mean free paths larger than the length of the main chamber.

Particle Flow Generator

The PFG is provided by ThrustMe [14], and is located in the largest chamber, placed on a horizontal rail. This degree of freedom allows to place the source in front of the window for spectroscopic measurements. The PFG takes as inputs a net amount of power, called the RF power (forward minus reflected), a mass flow rate of gas, either Argon or O_2, a voltage for ion acceleration, and a coil current for ion beam focusing. The output of a PFG is a partially ionized gas, with a stream of positive ions accelerated to speeds close to 8 km/s. The neutral particles on the other hand are not accelerated, therefore constituing a slow plume of neutrals. A picture of the PFG running on air is shown in Figure 1.4.

1.3 State of the art in plasma diagnostics and modelling

A plasma is a collection of charged particles. It is the most common state of matter, representing more than 99% of the matter in the observable universe. In addition to being abundant, plasmas have many applications. To cite a few, they are used for satellite propulsion, bacterial sterilization, welding, lasers, and neon tubes, and are also the basis for the current attempts at energy production by nuclear fusion. Understanding their behaviour is therefore crucial for

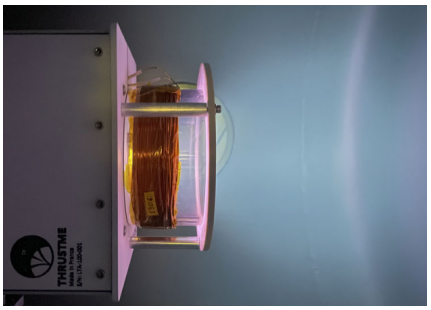

Figure 1.4: PFG running on atmospheric gas, from [15]

many fields of science. Plasma physics is therefore an active field of research, with more advanced experimental facilities and modelling methods being developed continuously. In this section, we review the main experimental plasma diagnostics and modelling methods, as this work will build upon them for the investigation of the plasma conditions in the DRAG-ON facility.

1.3.1 Facilities

Plasma research relies on facilities designed to generate plasmas under controlled conditions, for specific applications. They allow to study plasmas or plasma/materials interactions in a range of conditions. The results obtained in such facilities can be used as validation for numerical models. For space applications, they allow to perform tests on-ground, drastically reducing the cost of thruster performance testing. In this subsection, we highlight notable plasma facilities with a focus on space applications.

One of these facilities the VKI Plasmatron facility [16, 17]. It is ESA's reference laboratory for the reproduction of atmospheric re-entry conditions. It is used to investigate high temperature plasma interactions with ablative materials [18]. The plasma source consists of a 1200 kW inductive plasma torch. A high current coil is inductively coupled to current loops of mobile charged particles in the plasma, creating a high enthalpy, highly dissociated subsonic gas flow that can be made of any gas mixture, including air. The pressure inside the chamber can be varied between atmospheric and pressures of the order of 1 Pa at the lowest.

In addition to atmospheric plasma facilities, ion thruster facilities are crucial for the development and characterization of space propulsion systems. To best replicate the operating conditions of the tested thrusters, these facilities are usually pumped down to a high vacuum, for the background gas to be in the molecular flow regime, reducing the number of interactions with the ionized plume. Examples include the Space Propulsion Centre Singapore [19], testing electric propulsion systems in vacuum chambers that operate in pressures of the order of 5×10^{-4} Pa, and the SITAEL facility for testing of their RAM-EP concept [8], which also operates in extremely low background pressures. This last facility consists of a PFG which can run both on Xenon and air mixtures, sending an ion plume towards an ABEP system similar to the one shown in Figure 1.1.

1.3.2 Diagnostics

The facilities discussed above provide a diverse range of plasma conditions, from high density and high temperature regimes to low temperature and low density plasmas. Depending on the conditions, different techniques are used for the characterization of the plasma parameters. Plasma diagnostics refers to the set of methods that allow such measurements. Parameters of interest for the characterization of plasma are

- **Densities:** The number densities n_e, n_i, n_n [m^{-3}] of electrons, ions, and neutrals respectively give insight on the ionization ratio of the plasma. Because plasma sources work by ionizing a neutral gas, plasmas are quasi-neutral such that the ion and electron densities are equal and only one of these densities must be measured.

- **Temperatures:** The definition of temperature is linked to the velocity distribution of particles. The hotter the gas or plasma, the larger the range of speeds the particles are distributed in. The electron, ion, and neutral temperatures T_e, T_i, T_n [K][1] are therefore strongly linked to the kinetic energy distribution of the particles.

- **Degree of equilibrium:** Plasmas can be in different states of equilibrium. Thermal equilibrium refers to a plasma described by a unique temperature. Out of thermal equilibrium, electrons, ions, and neutrals can display large temperature differences. Another notion of equilibrium is chemical equilibrium. At chemical equilibrium, all chemical reactions are balanced. The concentrations of the different species can therefore be obtained with equilibrium relations.

- **Spatial profiles and bulk dynamics:** The way the plasma plume expands or flows, and at which speeds, is also of interest for many applications.

Plasma diagnostics methods are subdivided in two main categories: *invasive* and *non-invasive* diagnostics.

Invasive diagnostics

Invasive diagnostics include all probes that are placed inside the plasma. They most often measure electric currents due to the interactions between the conductive material of the probe and the charged particles in the plasma. The characteristic curves of these currents in function of the applied voltage give insight on the composition of the plasma, but also on the kinetic energy of the charged particles.

A commonly used probe is the *Langmuir probe* [20]. It consists of a conductor, usually a cylindrical wire, that is placed in the plasma and that can be tuned to a given voltage. It collects an electron current in response to that voltage, leading to an $i - V$ characteristic curve (with i [A] the current, and V [V] the voltage). Based on plasma theories and relating the kinetic energies of electrons to their temperature, this curve can be used to extract the electron temperature and density, but also their kinetic energy distribution. For plasmas out of equilibrium, this can be a valuable insight on the actual conditions inside the plasma. Information can also be

[1] Because of the high temperatures often involved in plasmas, they are often expressed in electron-volts with 1 eV $\simeq$ 11600 K.

extracted about the flow velocity of ions, their temperature, and density.

Another commonly used invasive diagnostics method is the *Faraday probe*. It consists of a collector plate of given surface area, with the normal of the plate pointing opposite to the plasma flow direction. The ion (or electron) flux therefore collides with the probe's surface. This results in a measurable current from the probe, which can be related to the ion/electron flux. Another version of this type of probe is the gridded energy analyser [21], which works by the same principle, but with the collector plate protected by a set of grids at a given potential. The electric field generated by the grids segregates the ions by kinetic energy: only the ions or electrons at selected energy get past the grids and are neutralized by the collector plate. By carrying out current measurements for different grid voltages, the energy distribution function of electrons or ions can be obtained. Although this probe can give valuable measurements, they are often large and therefore disturb the plasma flow downstream.

Non-invasive diagnostics

Non-invasive diagnostics techniques include all methods that do not require the placement of a physical probe in the plasma. They are based on the interactions of plasmas with electromagnetic waves. They have the major advantage of not perturbing the plasma flow, which is necessary for facilities such as DRAG-ON and the VKI Plasmatron, where the plasma is used as an incident flow on an intake or an ablative material. Perturbing this flow to make measurements upstream the interaction of interest can have important impacts on the final results, which is why non-invasive diagnostics are used in both these facilities.

Active non-invasive diagnostics include *Laser Induced Fluorescence* (LIF) [21]. It consists of sending a laser beam through a plasma, with the wavelength of the laser tuned to an electronic transition of the ions to analyze. The ions are therefore excited by absorption of the laser photons, and will therefore emit in all directions when being de-excited by radiative decay. By analysis of these emissions, the ion temperature can be extracted from the width of the emission lines.

Another form of non-invasive diagnostics is *Optical Emission Spectroscopy* (OES) [21]. This method is passive, as it does not require actively exciting the plasma. It relies on the measurement of the emission spectrum of the plasma. Indeed, atoms and ions in plasmas are excited by energetic collisions, which place them in higher energy levels that spontaneously decay to lower levels. This results in emissions at precise emission lines that depend on the nature of the emitting particles. By measuring the emission spectrum of the plasma, information can be extracted about the plasma conditions. OES refers to a family of methods to extract these plasma parameters. The number of parameters that can be extracted, as well as the reliability of the results, highly depend on the actual conditions of the plasma, the accuracy of the spectrometer, and the assumptions that are made. OES can be a standalone method to extract plasma parameters only if the plasma is in chemical equilibrium, in which case the measured emission lines can be compared to those predicted by equilibrium relations. For plasmas out of equilibrium, OES must be used with a chemical model of the plasma to predict the emissions based on plasma parameters.

1.3.3 Modelling

Plasma modelling refers to any set of equations that are used to predict the behaviour of a plasma based on a limited set of parameters. The model fitted for an application highly depends on the conditions of the plasma, the level of fidelity required, and the available computational resources. Modelling plays a crucial role alongside experimental measurements, as it allows to complement them by giving insight on the parameters that are more challenging to access directly.

For plasmas at high densities, in which particle interactions dominate, the plasma can be modeled as a continuous medium. In this case, they are described by the Navier-Stokes equations, coupled with the Maxwell equations for the interactions of the plasma with electric and magnetic fields. For chemically active plasmas, chemical models can also be coupled with the previous sets of equations [22]. This is the set of equations used for plasmas such as the one encountered in the VKI Plasmatron facility.

At lower densities, when the mean free path of the particles rises, the continuum assumption loses its validity. The plasma must be seen as a set of particles distributed in space with a velocity distribution. The governing equation for a low density gas or plasma is the Boltzmann equation, discussed in Chapter 2. It predicts the evolution of the velocity distribution of the particles, based on the collisions inside the plasma. For the prediction of plasma characteristics, the Boltzmann equation can be solved numerically, but this comes at a high computational cost because of the large number of dimensions of this equation and the large range of scales involved [23].

The previously mentioned methods are often computationally expensive to solve. In some cases, simpler models can be used to provide the needed information without solving the kinetic equations. Collisional-Radiative (CR) models serve that purpose. Tallents [24] provides a comprehensive description of CR models, as well as tools to build them for a variety of cases. CR models aim to describe the chemical processes inside plasmas where the collisions between charged particles and/or neutral particles tend to transfer kinetic energy to the internal energy of the atoms or molecules, raising the energy levels of the colliding species. It consists of a set of rate equations for excitation and de-excitation reactions, where the rates are obtained from prior knowledge of the kinetic energy of the colliding particles, their density and nature. They allow the determination of population densities of excited states, from which the radiative signature of the plasma can be predicted. Such models are widely used in the literature, often as a complement of OES: the measured line intensities are compared to those predicted by the CR model, and the plasma parameters are obtained by the best match between the predicted intensities and the experimental intensities. This method is widely used in the literature [25, 26, 27, 28, 29], but highly depends on the accuracy of the model.

1.4 Objectives and methodology

The present work has the objective of implementing a first iteration of a non-invasive method for the characterization of the plasma conditions in the DRAG-ON facility, for an Argon plasma flow. The preferred method is Optical Emission Spectroscopy. Because of the extremely low

density plasma encountered in the facility, the plasma is expected to be out of chemical equilibrium. A Collisional-Radiative model is therefore required for the prediction of the level populations based on plasma parameters.

To achieve this goal, several sub-objectives are defined:

1. **Construction of a CR model for Argon, adapted for the non-equilibrium conditions met in DRAG-ON**. It must be able to predict the populations of the excited states of Argon for a given set of plasma parameters. This prediction is done by solving a constructed system of coupled rate equations of the form $dn_i/dt = \dot{\omega}_i$ with n_i the number density of energy level i, and $\dot{\omega}$ $[\mathrm{m}^{-3}\cdot\mathrm{s}^{-1}]$ the net production rate of level i. After a detailed discussion of the physics involved and reactions to consider, the CR model construction is carried out in Chapter 2. First tests of the behaviour of the CR model allow to identify the plasma parameters that influence the CR model results.

2. **Measurement of the emission spectrum in the DRAG-ON facility.** This sub-objective requires an experimental setup, the calibration of this optical setup and the numerical tools for the extraction of the line intensities. The possibility of measuring spatial distributions is also investigated. The details of this second building block of the methodology is discussed in Chapter 3.

3. **Definition of a comparison method for experimental and CR intensities.** A comparison criterion ξ must be defined to compare the experimental intensities and the synthetic intensities predicted by the CR model. This comparison criterion is defined as a measure of the error between the experimental and synthetic line intensities. By performing a parametric minimization of this objective function, we find the plasma parameters that best replicate the measured spectrum. This minimization process is carried out in Chapter 4, along with an uncertainty analysis of the obtained results.

A flowchart of the developed methodology is represented in Figure 1.5.

At this early stage of the investigations on the conditions in the DRAG-ON facility, the modelling will have to rely on assumptions that can not necessarily be verified at first. From the preliminary results obtained with the present exploratory work, main research questions therefore arise:

- **To what extent does the plasma inside the DRAG-ON facility deviate from chemical and thermal equilibrium conditions?**

- **From the investigation of the plasma conditions, are typical CR assumptions valid for the plasma generated by DRAG-ON's PFG? If not, how to increase the fidelity of the model?**

Answering these questions will allow a review of the assumptions made for the construction of the CR model. This will allow to have higher fidelity results in the future, which can then be used to assess the actual conditions in the facility with non-invasive diagnostics.

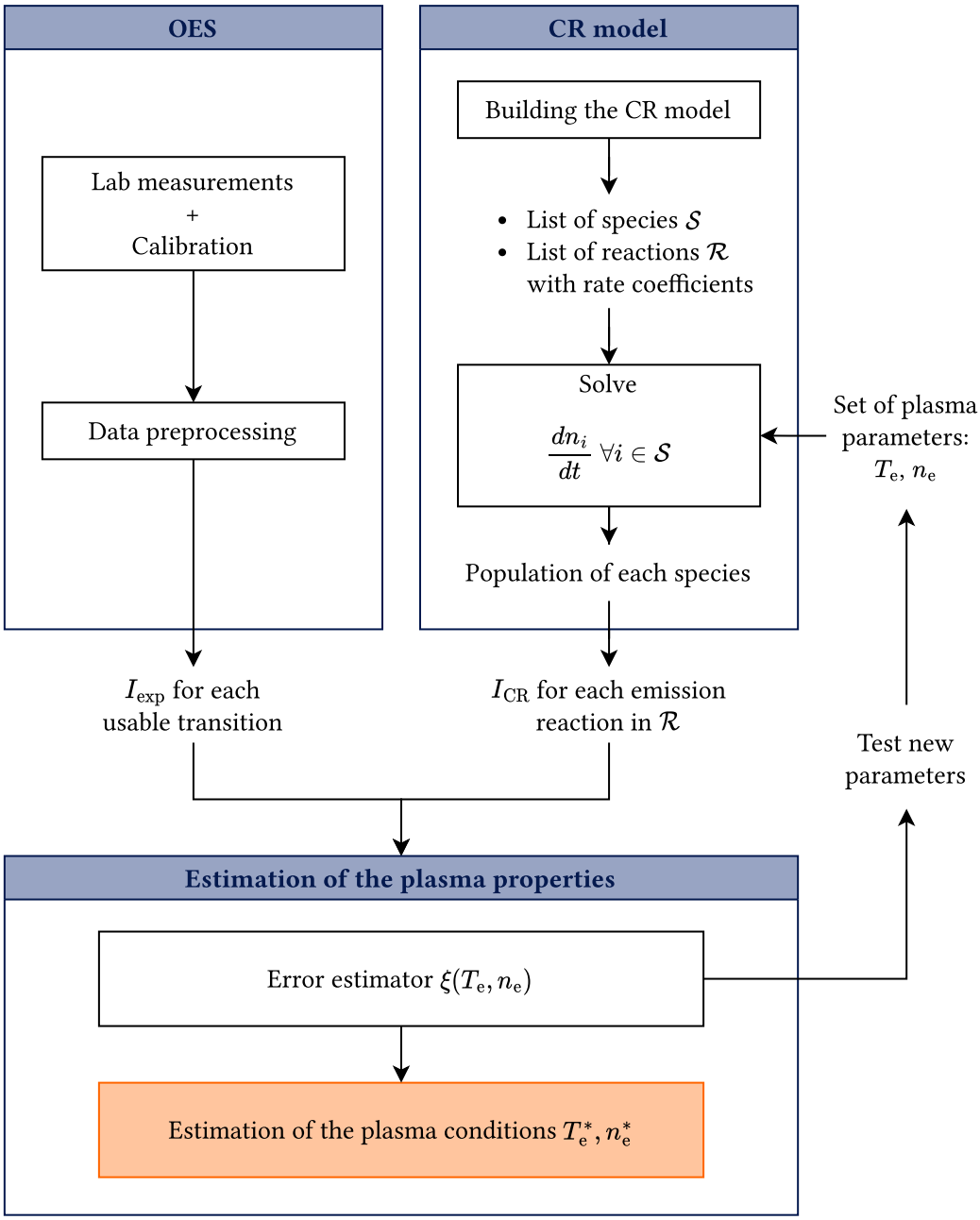

Figure 1.5: Methodology flowchart

CHAPTER 2

Plasma Physics and Modelling

This chapter has the objective of providing a fundamental understanding of the physics involved in the DRAG-ON facility, and based on this theory, to provide predictive a model for the emission of the plasma. The first step will be to introduce the basic concepts of plasma physics, including the main properties of plasmas and the behaviour of charged particles in electric and magnetic fields. Next, an introduction to the kinetic theory for gases is provided, to give a framework for understanding the behaviour of particles in gaseous state, and their interactions. In order to explain the origin of the later measured emission of excited gases, electronic levels of atoms will then be introduced, along with the excitation and de-excitation mechanisms.

Several sources provide a thorough description of these concepts, including Chen and Chang's lecture notes on plasma processing [21], Bittencourt's book on plasma physics [30], Tallents' book with a focus on radiation in plasmas [24], and Boyd and Schwartzentruber's book on gas dynamics [31]. We will draw upon these sources to provide a comprehensive overview of the relevant concepts.

Once the fundamentals have been addressed and put into equations, a 0-D Collisional-Radiative model is constructed for Argon, based on all the concepts addressed in this chapter. This model corresponds to the numerical predicting block in the methodology, allowing the computation of the composition of the plasma based on several plasma parameters. This will be key to determining the plasma parameters that correspond to the emission spectra measured in the DRAG-ON facility, discussed in Chapter 3.

2.1 Notions of plasma physics

A gas at ambient temperature consists of particles flying around, each at a given speed in a given direction. This leads to collisions between these particles, of which the frequency depends on the density, speeds and nature of the particles. The way particles are distributed across all possible velocities will be discussed in more detail in Section 2.2. At ambient temperature, these collisions lead mainly to momentum transfer at a the microscopic level. This allows for a variety of observable phenomena at macroscopic level, such as the diffusion of heat when hotter regions of a gas, containing higher velocity particles, transfer their momentum to colder regions. Another manifestation of this momentum transfer is the propagation of pressure (sound) waves when denser regions tend to expand into thinner regions.

When heating a gas, the speed distribution of the particles changes, increasing the number of particles at higher speeds. This increases the strength of the collisions between particles.

Gradually, some collisions can start to have an impact on the electronic structure of atoms themselves, exciting electrons to higher levels of energy. At some point (of the order of 10000 K), some collisions become energetic enough to rip electrons from atoms. When this ionization process becomes significant, the gas obeys new laws as it is now a collection of neutral and charged particles, making it able to interact with electric and magnetic fields. This is the *plasma* state of matter. In the following, some aspects of plasma physics are discussed, giving a better insight on the additional considerations to have when dealing with a collection of mobile, charged particles.

Debye length

In a large scale, plasmas are neutral by definition, since all free electrons come from the ionization of a neutral atom. An important parameter to characterize a plasma is the length scale at which the plasma can be said to be neutral. This scale is called the Debye length λ_D [m]. It can be derived from Poisson's equation [21, 24]. For two plates at earth potential separated by a distance $2a$ [m] filled with an electron number density n_e [m^{-3}], the electrostatic potential V [V] at each x position is given by

$$\nabla^2 V(x) = \frac{d^2V(x)}{dx^2} = \frac{n_e e}{\varepsilon_0} \tag{2.1}$$

with $\varepsilon_0 = 8.854 \times 10^{-12}$ F/m the vacuum permittivity and $e = -1.602 \times 10^{-19}$ C the charge of the electron. At the center point ($x = a$), the potential is

$$V(a) = \frac{n_e e a^2}{2\varepsilon_0} \tag{2.2}$$

The potential energy at this point, or energy needed to move an electron from ground potential to $x = a$, is $U(a) = eV(a)$ [J]. On the other hand, the average kinetic energy of an electron at temperature T_e [K] is $1/2 \cdot k_B T_e$ [J], with $k_B = 1.381 \times 10^{-23}$ J/K the Boltzmann constant. The average electron will therefore have enough energy to escape from the ground potential if

$$\frac{1}{2} k_B T_e = \frac{n_e e^2 a^2}{2\varepsilon_0} \tag{2.3}$$

The Debye length λ_D corresponds to distance a at which the ground potential plates stop influencing the average electron. It is therefore expressed as

$$\lambda_D^2 = \frac{\varepsilon_0 k_B T_e}{n_e e^2} \tag{2.4}$$

Plasma frequency and speed of sound

Several types of waves can travel within a plasma. Two interesting types of waves in this medium are the *plasma waves* and *ion acoustic waves*. The first type corresponds to a group motion of electrons: if a collection of electrons are moved slightly in one direction, they will leave a positively charged region behind them, attracting them back to place in an oscillatory motion. The frequency of these oscillations is called the plasma frequency ω_p [rad/s]. It can

be derived from the law of motion of the electrons, with the electric force being derived from Gauss' law [24]

$$m_e \frac{d^2x}{dt^2} = e\mathcal{E} = -\frac{n_e e^2}{\varepsilon_0} x \tag{2.5}$$

with $m_e = 9.109 \times 10^{-31}$ kg, the mass of the electron, and $\mathcal{E}$ [V/m] is the electric field. This leads to an oscillatory motion with frequency

$$\omega_p^2 = \frac{n_e e^2}{m_e \varepsilon_0} \tag{2.6}$$

The ion acoustic waves behave differently. When moving a group of ions to one direction, the much lighter electrons will follow them, partially neutralizing the movement of the ions. However, since the electrons have a non-zero velocity distribution due to their temperature T_e, the shielding will not be perfect, leading to a small electric field being propagated through the plasma. These ion acoustic waves propagate at the ion speed of sound c_s [m/s]. For low density plasmas verifying $T_e \gg T_i$, with T_i the ion temperature, the ion speed of sound is given by the Bohm velocity [32]:

$$c_s^2 = \frac{k_B T_e}{m_i} \tag{2.7}$$

showing the dependency of the propagation of these waves to the electron temperature T_e.

If the plasma is partially ionized, the neutral atoms also have their characteristic speed of sound, defined by the speed of the pressure waves inside this neutral gas.

Larmor radius

When a plasma is submitted to a magnetic field $\mathbf{B}$, its charged particles' motion is affected. Charged particles embedded in a magnetic field are subject to the Lorentz force $\mathbf{F} = q\mathbf{v} \times \mathbf{B}$, with q their charge and $\mathbf{v}$ their velocity vector. This force being always perpendicular to the velocity of the charged particles and to the magnetic field, it will have no effect on the velocity component parallel to the magnetic field. The component $v_\perp$ in the plane perpendicular to $\mathbf{B}$ however is subject to a force perpendicular to its direction, forcing it to a circular motion of given radius: the Larmor radius

$$r_L = \frac{v_\perp}{\omega_c} \tag{2.8}$$

where ω_c [rad/s] is the cyclotron frequency

$$\omega_c = \frac{|qB|}{m} \tag{2.9}$$

with m [kg] the mass of the charged particle of interest. It is therefore clear that the Larmor radius of the ions is orders of magnitude larger than that of the electrons. In most practical cases, only the electrons' motion will be affected significantly by the applied magnetic field. An illustration of this circular motion can be found in Figure 2.1.

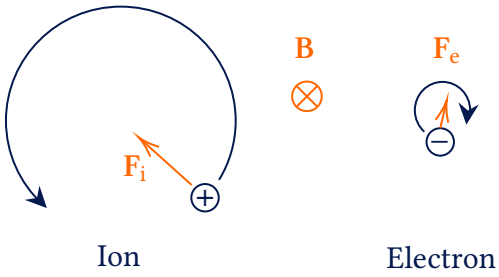

Figure 2.1: Representation of the Larmor radius

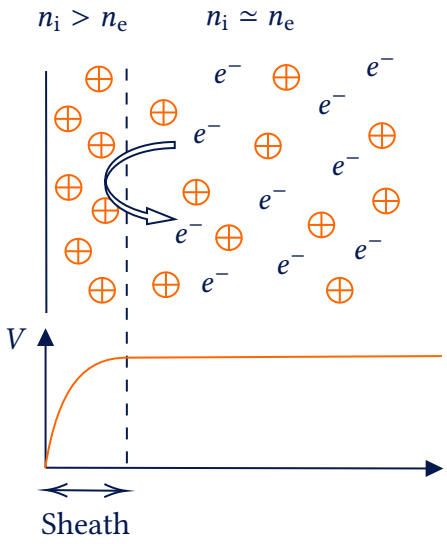

Figure 2.2: Sheath layer and related potential

Plasma sheath

When a plasma is in contact with a physical boundary, a sheath layer is created. This sheath layer is thick of a few Debye lengths, and is a region populated with more positive ions than electrons, thus violating the quasineutrality of the plasma locally as shown in Figure 2.2. This layer appears because of electrons, usually hotter and faster than the ions, escaping the plasma and colliding with the boundary, charging it negatively, until this wall is charged negatively enough to repel the electrons from the plasma. Because of the negative charge of the surface, positive ions migrate to this surface, such that there appears a layer of given thickness (usually around $5\lambda_D$) with mostly positive ions and neutral atoms shielding the plasma from the negative potential of the wall. This layer is called the Debye sheath.

An important characteristic of such a sheath is the *Bohm criterion* for the velocity of the ions: for the sheath to have the described shape and shielding effect, the ions must enter the sheath with a velocity at least greater than the Bohm speed c_s. For the ions to achieve such velocities, there must be a region in the plasma called the *presheath* with momentum transfer mechanisms such as collisions, or a small electric field accelerating some ions towards the sheath edge.

This concept of sheath shows the importance of determining the electron temperature T_e in a plasma, because it affects the thickness of the sheath layer by affecting the Debye length, but also the ion acoustic velocity. This layer can have an effect on the measured intake efficiency in the DRAG-ON facility.

2.2 Basics of kinetic theory for elastic interactions

As introduced in Section 2.1, plasmas and gases contain a very large number of particles that interact with each other by means of collisions. The state of a gas at instant t could be described completely by the position and velocity vectors of each particle. It is however more

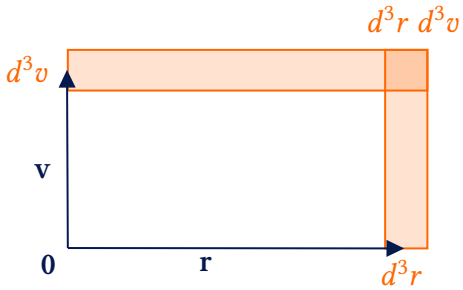

Figure 2.3: Differential element around $(\mathbf{r}, \mathbf{v})$ in the phase space. Reproduced from [30]

convenient to use a statistical approach for the description of the state of the particles. From this statistical knowledge of the position and velocity of the particles constituting the gas, macroscopic quantities can be computed. The equation governing the time evolution of this statistical knowledge of the state of particles is called the *Boltzmann equation*, and will be derived in this section after the introduction of the necessary concept of *distribution function*.

2.2.1 Phase space and distribution function

Kinetic theory places particles in a 6-dimensional space, called the *phase space*, with 3 dimensions corresponding to the spatial position of the particle, and 3 others corresponding to the position of the particle in the velocity space

$$\mathbf{r} = x\hat{\mathbf{x}} + y\hat{\mathbf{y}} + z\hat{\mathbf{z}} \tag{2.10}$$

$$\mathbf{v} = v_x\hat{\mathbf{x}} + v_y\hat{\mathbf{y}} + v_z\hat{\mathbf{z}} \tag{2.11}$$

The position of a particle in the phase space is therefore entirely represented by the two vectors $\mathbf{r}$ and $\mathbf{v}$. Small variations about this position can be denoted by the differential element $d^3r\ d^3v$ in this 6-dimensional space, as shown in Figure 2.3. In this figure, the segments of the 6-D differential element correspond to cubes in the position and velocity spaces.

By denoting $d^6\mathcal{N}_j(\mathbf{r}, \mathbf{v}, t)$ the number of particles of type j (ion, electron or neutral atoms) in the element $d^3r\ d^3v$, the *distribution function* can be defined by

$$f_j(\mathbf{r}, \mathbf{v}, t) = \frac{d^6\mathcal{N}_j(\mathbf{r}, \mathbf{v}, t)}{d^3r\ d^3v} \tag{2.12}$$

It represents the number density of particle type j in the phase space (density in the volume generated by all 6 dimensions, not only the spatial dimensions). The time evolution of this distribution function is described by the evolution of the velocities of each particle constituting the gas or plasma, either due to an external force, or by collisions between the particles, transferring momentum. The equation describing the effects of these factors on the distribution function is the *Boltzmann equation*.

2.2.2 Boltzmann equation

Let there be a gas, out of equilibrium, containing particles of different types. Following the notations used in Equation 2.12, the number of particles of type j contained in the phase space

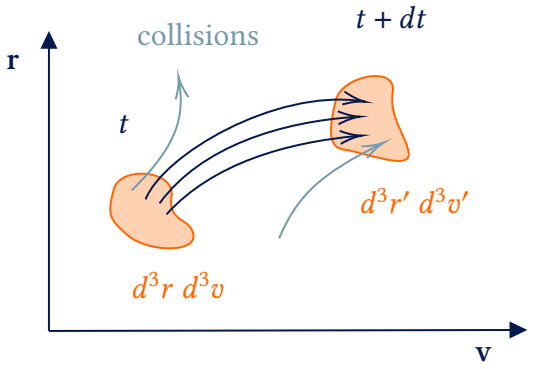

Figure 2.4: Evolution of an infinitesimal volume between t and $t + dt$ in the phase space (reproduced from [30])

volume $d^3r\ d^3v$ around position $(\mathbf{r}, \mathbf{v})$ at instant t is $d^6\mathcal{N}_j(\mathbf{r}, \mathbf{v}, t)$. If a force $\mathbf{F}$ is applied to all particles of type j, they are accelerated with an acceleration $\mathbf{F}/m_j$, such that at time $t+dt$ these same particles now occupy a new volume $d^3r'\ d^3v'$, around position $(\mathbf{r}', \mathbf{v}')$ defined by

$$\mathbf{r}'(t + dt) = \mathbf{r}(t) + \mathbf{v}(t)dt \tag{2.13}$$

$$\mathbf{v}'(t + dt) = \mathbf{v}(t) + \frac{\mathbf{F}}{m_j}dt \tag{2.14}$$

Since we are following the same set of particles, it can be said that the number of particles in the second volume is equal to the number of particles in the first volume

$$d^6\mathcal{N}_j(\mathbf{r}', \mathbf{v}', t) = d^6\mathcal{N}_j(\mathbf{r}, \mathbf{v}, t) \tag{2.15}$$

This equality holds only for collisionless cases. In general, this is not the case. Some particles are pushed out of the volume, and some are pushed in between instants t and $t + dt$, such that we can define a net variation of the number of particles with time, as illustrated in Figure 2.4. Adding this collision term, and using the definition of the distribution function from Equation 2.12, we can therefore write

$$f_j(\mathbf{r}', \mathbf{v}', t)\ d^3r'\ d^3v' = f_j(\mathbf{r}, \mathbf{v}, t)\ d^3r\ d^3v + \left(\frac{\partial f_j}{\partial t}\right)_{\text{coll}} d^3r\ d^3v\ dt \tag{2.16}$$

The last term in the right-hand side accounts for the net variation of the number of particles due to collisions. It can be shown that the Jacobian of the transformation between the two elements of volume is unitary, such that we can write $d^3r'\ d^3v' = d^3r\ d^3v$. After a Taylor expansion of Equation 2.16, the Boltzmann equation can be written as

$$\frac{\partial f_j}{\partial t} + \mathbf{v} \cdot \frac{\partial f_j}{\partial \mathbf{r}} + \frac{\mathbf{F}}{m_j} \cdot \frac{\partial f_j}{\partial \mathbf{v}} = \left(\frac{\partial f_j}{\partial t}\right)_{\text{coll}} \tag{2.17}$$

For this equation to be complete, there needs to be a model for the collision term. This model depends on the type of collisions considered: they can be elastic, transferring momentum only, or inelastic. Inelastic collisions occur when part of the kinetic energy from the collision is transferred to the internal energy of the colliding species. For molecules, this can be rotational or vibrational energies, or even chemical bounds, but for the purpose of this work, only atoms are considered (Argon gas). Inelastic collisions can therefore only transfer energy to the bound electrons of the atoms, increasing the energy level or ionizing the atoms. This will be further discussed in Section 2.3.

2.2.3 Mean free path and Knudsen number

A simple dimensional analysis of the Boltzmann equation allows the introduction of an important adimensional number for the characterization of low density flows: the *Knudsen number* Kn [-]. It appears by taking the ratio of the right-hand side with the left-hand side of Equation 2.17.

- The right-hand describes the evolution of the distribution function by the transport processes. Its dimensions are therefore the dimensions of a distribution function f_0 [s^3/m^6], divided by the typical flow time $t_0 = L/v_0$ [s], where L [m] and v_0 are respectively a reference length and speed.
- The left-hand side describes the evolution of the distribution function due to collisional processes. It obviously has the same dimensions as the right-hand side, but for collisional processes, the reference time is $t_{\text{coll}} = \overline{\lambda}/v_0$ [s], with $\overline{\lambda}$ [m] the mean free path (or average length covered by a particle before a collision with another particle).

The ratio therefore evolves according to

$$\frac{\text{right}}{\text{left}} = \frac{\text{collisional processes}}{\text{transport processes}} \propto \frac{f_0/t_{\text{coll}}}{f_0/t_0} = \frac{L/v_0}{\overline{\lambda}/v_0} = \frac{L}{\overline{\lambda}} = \frac{1}{\text{Kn}}$$

with the Knudsen number Kn [-] defined as

$$\text{Kn} = \frac{\overline{\lambda}}{L} \tag{2.18}$$

This non-dimensional number therefore provides an indication of how rarefied a flow is, with respect to its reference length scale. It is an important consideration when modelling a gas or plasma, as it defines the boundary between continuous and rarefied media. It is generally accepted that for $\text{Kn} < 0.01$, the fluid can be considered to be continuous. This means that the Navier-Stokes equations for the macroscopic quantities are a good model for the flow. For $\text{Kn} \gg 1$ however, the collision term of the Boltzmann equation becomes negligible. We then talk about free molecular flow, where the particles can be assumed to be independent of each other. In between, there are collisions, but not at a high enough rate for the medium to be considered continuous, such that kinetic theory rules, with models for collisions defining the rate of transmission of momentum.

An expression for the mean free path can be obtained by considering the cylinder in which a particle moves [31]. Consider a solid particle of diameter d, at velocity v. It will enter in collision with another particle only if another particle is located in its sphere of influence, which is a sphere with a diameter equal to $2d$, as defined by Figure 2.5. We define the cross section of that hard sphere $\sigma_{\text{HS}} = \pi d^2$ [m^2]. The volume covered by the moving sphere per unit time is therefore $v\sigma_{\text{HS}}$. With n [m^{-3}] the density of particles per unit volume, the collision frequency ν_{coll} [s^{-1}] is therefore given by

$$\nu_{\text{coll}} = nv\sigma_{\text{HS}} \tag{2.19}$$

The average distance covered between two collisions (mean free path) is therefore given by

$$\overline{\lambda}_{\text{HS}} = \frac{v}{\nu_{\text{coll}}} = \frac{1}{n\sigma_{\text{HS}}} \tag{2.20}$$

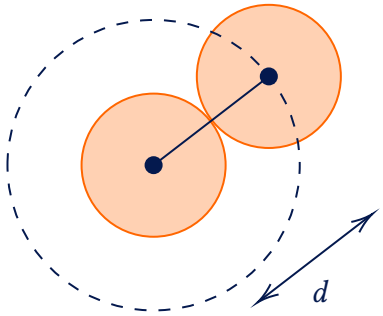

Figure 2.5: Sphere of influence, reproduced from [31]

This expression holds only for a mobile hard sphere particle evolving in an environment with static particles of the same cross section. It however allows to illustrate what main parameters the mean free path depends on: the number density and the cross section for the collisions. In subsection 2.2.5, we provide a more detailed description of the concept of cross sections for physical particles.

For a more accurate expression of the mean free path, one must also have knowledge of the velocity distribution function of the particles. A common assumption for gases with sufficient collisions is the equilibrium solution of the Boltzmann equation: the *Maxwell-Boltzmann distribution function*, for which an expression is given in subsection 2.2.4. For such a distribution, the mean free path becomes

$$\bar{\lambda}_{\mathrm{HS}} = \frac{v}{\nu_{\mathrm{coll}}} = \frac{1}{\sqrt{2} n \sigma_{\mathrm{HS}}} \tag{2.21}$$

2.2.4 Maxwell-Boltzmann distribution function

The Maxwell-Boltzmann distribution function is the equilibrium solution of the Boltzmann equation, in absence of an external force $\mathbf{F}$. This solution is time independent, homogeneous (does not depend on the position $\mathbf{r}$), and isotropic (does not depend on the direction of the velocity, only on its norm $v = |\mathbf{v}|$). It therefore reduces to a function of one variable, giving the number density in the state space shell of all velocity vectors with a norm between v and $v + dv$. For an observer following the gas at its flow velocity, this solution writes

$$f_j(v) = n_j \left(\frac{m_j}{2\pi k_{\mathrm{B}} T} \right)^{3/2} \exp\left\{ -\frac{m_j v^2}{2 k_{\mathrm{B}} T} \right\} \tag{2.22}$$

A gas in this configuration has a collision term equal to zero, such that for every collision increasing a particle's momentum, there is another particle losing the same amount of momentum. For a gas or plasma composed of multiple species j, the collision term only goes to zero when all species are at the same temperature T. In most plasmas however, this absolute equilibrium is not reached because of the usually low density, and the orders of magnitude between the masses of electrons and heavy particles (ions and neutrals). At each collision, electrons only transfer negligible momentum to the heavy particles, such that the electrons and heavy particles reach separate temperatures T_{e}, T_{i} and T_{n}. If the number of collisions is sufficient, all species can reach a Maxwellian distribution function separately, in which case Equation 2.22 must be particularized for each species j with a separate temperature T_j. This

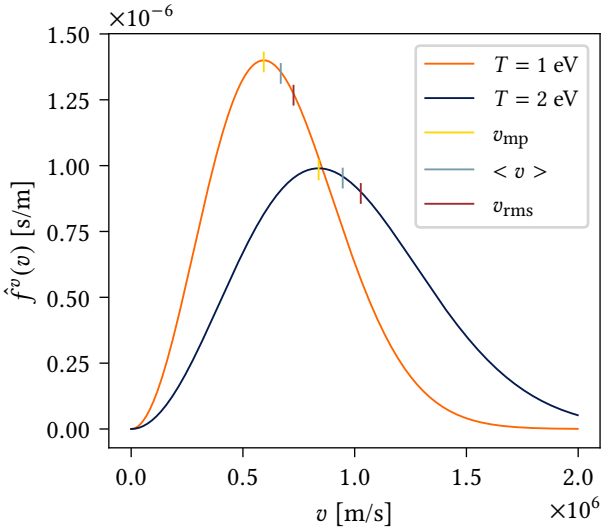

Figure 2.6: Normalized Maxwell-Boltzmann speed distribution and characteristic speeds (for electrons at T_e = 1 and 2 eV)

is the relevant case for the low density plasma studied in this work.

For convenience, it is interesting to define a *distribution of speeds*, expressing the number density in the 1-D element $v \longrightarrow v + dv$ instead of the number density in the 3-D shell in the velocity space, of all vectors of norm between v and $v + dv$. This distribution of speeds $f^v(v)$ can be obtained by integrating over this shell. With θ and ϕ the spherical coordinate angles in the velocity space, this gives

$$f_j^v(v)\, dv = \int_0^{\pi} \int_0^{2\pi} f_j(v) v^2 \sin\theta \, d\theta \, d\phi \, dv = 4\pi v^2 f_j(v) \, dv \tag{2.23}$$

such that the Maxwell-Boltzmann distribution of speeds for species j is expressed

$$f_j^v(v) = 4\pi n_j \left(\frac{m_j}{2\pi k_B T_j} \right)^{3/2} v^2 \exp\left\{ -\frac{m_j v^2}{2 k_B T_j} \right\} \tag{2.24}$$

The integral over all possible speeds naturally gives the number density

$$\int_0^{\infty} f_j^v(v) \, dv = n_j \tag{2.25}$$

The speed distribution can therefore be normalized by n_j, giving the normalized distribution of speeds such that

$$\int_0^{\infty} \hat{f}_j^v(v) \, dv = 1 \tag{2.26}$$

Speeds of interest can be extracted from this speed distribution function, as illustrated in Figure 2.6. The average speed is found as

$$< v_j >= \int_0^{\infty} v \hat{f}_j^v(v) \, dv = \left(\frac{8}{\pi} \frac{k_B T_j}{m_j} \right)^{1/2} \tag{2.27}$$

The root mean square speed

$$v_{j_{\text{rms}}} = \left(\frac{3k_{\text{B}}T_j}{m_j}\right)^{1/2} \tag{2.28}$$

The most probable speed (maximum of the distribution)

$$v_{j_{\text{mp}}} = \left(\frac{2k_{\text{B}}T_j}{m_j}\right)^{1/2} \tag{2.29}$$

It can be noted that all speeds are proportional to $(k_{\text{B}}T_j/m_j)^{1/2}$, such that when the temperature increases, all characteristic speeds increase.

Equivalently, the particles can be distributed across the spectrum of possible thermal kinetic energies, by making the variable change $E = mv^2/2$. This leads to the *Maxwellian distribution of thermal kinetic energy*

$$f_j^E(E) = 2n_j\sqrt{\frac{E}{\pi}}\left(\frac{1}{k_{\text{B}}T_j}\right)^{3/2}\exp\left\{-\frac{E}{k_{\text{B}}T_j}\right\} \tag{2.30}$$

which can be normalized to $\hat{f}_j^E(E)$ similarly to what was done for the distribution of speeds.

2.2.5 Collision cross section

The *total scattering cross sections* σ [m^2] provides a measure of the probability of collision, depending on the nature of the particles colliding. As it was shown in subsection 2.2.3, the values of cross sections can greatly influence the rate of collisions in the collision term of the Boltzmann equation. In this work, only two-body collisions will be taken into account. At low densities such as those met in DRAG-ON, three-body collisions are immensely less probable, such that they can be neglected.

The discussion about the mean free path in subsection 2.2.3 provided a simplistic approach to the concept of cross sections, by considering hard sphere particles that either interact if they enter their respective spheres of influence, or do not interact otherwise.

In reality, particles are atoms, molecules, electrons, or ions. Their volume therefore lacks a rigid boundary. Particles interact through the electric fields generated by the charged particles that constitute them. In function of the distance, they are therefore submitted to a potential that will eventually repel the particles away from each other once the distance is small enough, since at a small distance there is a strong repulsive force due to the negative electron clouds of both particles. An example of this potential field for two neutral atoms is illustrated in Figure 2.7[1], along with the hard sphere model. The approximate distance at which the particles repel can be seen as the sum of the radii in the hard sphere model.

[1]It shows that there is, at some point, a weak attracting force between the particles, but this usually has no effect since the particles have too much kinetic energy to stay in the potential bucket (except if they are reactive atoms, in which case the bucket is very deep and chemical bonds can be created)

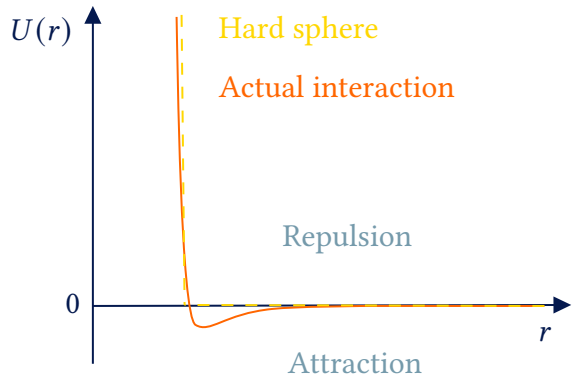

Figure 2.7: Interaction potential for two Argon atoms (adapted from [31]), and hard sphere model

Let there be two particles with velocities $\mathbf{v}_1$ and $\mathbf{v}_2$, with masses m_1 and m_2, subject to an elastic collision. In the reference frame of the first particle, their trajectories in the plane can be represented by Figure 2.8. In this reference frame, the incident velocity of the second particle is the relative velocity $\mathbf{v_{12}} = \mathbf{v}_2 - \mathbf{v}_1$. Knowing the impact parameter b, the velocity $\mathbf{v}_{12}$ and the driving potential $U(r)$ [J] between the particles, the collisional deflection angle $\chi(b, v_{12})$ can be computed with the following equation [30]

$$\chi(b, v_{12}) = \pi - 2 \int_{r_\mathrm{m}}^{\infty} \frac{b}{r^2} \left[1 - \frac{b^2}{r^2} - \frac{2U(r)}{m_2 v_{12}^2} \right]^{-1/2} dr \tag{2.31}$$

with r_m [m] the distance of closest approach, solution of

$$r_\mathrm{m} = b \left[1 - \frac{2U(r_\mathrm{m})}{m_2 v_{12}^2} \right]^{-1/2} \tag{2.32}$$

Let us now imagine a flux Γ [$\mathrm{m^{-2}s^{-1}}$] of incident particles, all at relative velocity $\mathbf{v}_{12}$, but at different impact parameters b and with trajectories lying on different planes defined by angles θ (for a central force potential as $U(r)$, the trajectory remains planar). The particles with the smallest b are deflected more, and those with a larger b are less deflected, such that the particles passing through a surface $b\ db\ d\theta$ are all deflected in a solid angle $d\Omega = \sin\chi\ d\chi\ d\theta$. The *differential scattering cross section* $\sigma_\mathrm{d}(\chi, \theta)$ is defined as the number of particles scattered per unit time, per unit incident flux, and per unit solid angle with orientation (χ, θ). We therefore have

$$\frac{d\mathcal{N}}{dt} = \Gamma\ b\ db\ d\theta = \sigma_\mathrm{d}(\chi, \theta)\ \Gamma\ d\Omega \tag{2.33}$$

Which gives

$$\sigma_\mathrm{d}(\chi, \theta) = -\frac{b}{\sin\chi} \frac{db}{d\chi} \tag{2.34}$$

the minus sign appears because the cross section is defined as a positive quantity, and $db/d\chi$ is negative.

The *total scattering cross section* σ [$\mathrm{m^2}$] (simply referred to as *cross section* in the following of this work), is obtained by integrating the differential scattering cross section over the entire

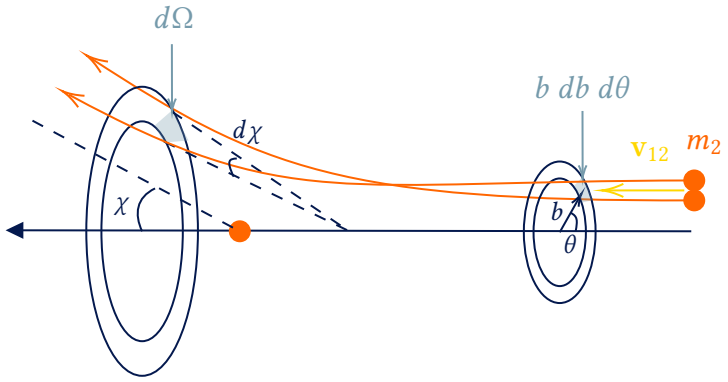

Figure 2.8: Particle scattering by a central potential field, adapted from [30]

solid angle

$$\sigma = \int_0^{2\pi} d\theta \int_0^{\pi} \sigma_{\mathrm{d}}(\chi, \theta) \sin\chi \, d\chi \tag{2.35}$$

These equations show that for a given potential $U(r)$, we can get $\chi(b, v_{12})$ (Equation 2.31) from which we can then obtain the cross section σ with equations 2.34 and 2.35. Applying these equations to the hard sphere model, for spheres of radii r_1 and r_2, Bittencourt [30] shows that we get a cross section

$$\sigma_{\mathrm{HS}} = \pi(r_1 + r_2)^2 \tag{2.36}$$

These so-defined cross sections σ therefore have an elegant geometrical interpretation, by corresponding to the cross section of the sphere of influence around the particle, for the hard sphere model. For more precise computations, they provide a framework to obtain predictions of the trajectories of particles interacting with each other, provided a model for the interaction potential $U(r)$. The latter can be obtained from quantum mechanical calculations of the repulsive forces due to the overlap of the electronic configurations of the considered particles. These cross sections have been calculated in various ways, either numerically or experimentally, for many kinds of collisions. The results of these campaigns can be found in databases such as *LXCat* [33]. It must be noted that, since the cross section evaluation depends on the incident relative velocity, cross sections are most often given in function of the velocity at which the collision occurs (or equivalently the energy of the collision).

2.3 Electronic levels of an atom

In Section 2.2, we considered solely elastic collisions, transferring momentum from one particle to another. In this section, we will see that this is not always the case. For the most energetic collisions, part of the kinetic energy can be transferred to the electronic structure of the atoms or molecules, leading to chemical reactions. In this work, we deal with Argon atoms, which can not bond together but can change their electronic configuration through various excitation processes. A short review of the quantum theory behind the electronic configurations is therefore provided, followed by a discussion of the various excitation and de-excitation processes that can induce changes in these electronic states.

2.3.1 Energy levels

The governing equation for quantum mechanics is the Schrödinger equation. By solving its time independent form, for a nucleus of given charge and a given number of electrons, one can obtain a discrete set of solutions corresponding to the possible electronic configuration an atom or ion can find itself in.

Single electron

For the simple case of a positive nucleus of mass m_N with Z protons and a single electron (hydrogenic particle), the potential field around the nucleus is

$$U(r) = -\frac{Ze^2}{4\pi\varepsilon_0 r} \tag{2.37}$$

Solving the purely radial, time independent form of the Schrödinger equation, we can get the discrete levels of energy the electron can reach

$$E_p = -\frac{Z^2\mu e^4}{8\varepsilon_0^2 h^2}\frac{1}{p^2} \quad p = 1,\ 2,\ 3\ldots \tag{2.38}$$

with $\mu = m_e m_N/(m_e + m_N)$ [kg] the reduced mass, $h = 6.626 \times 10^{-34}$ Js Planck's constant, and p the principal quantum number[2]. The principal quantum number therefore determines the energy level of the electron, or the energy that has to be given to the electron to extract it from the influence of the nucleus. Three additional quantum numbers are however necessary to entirely define the state of an electron:

- The orbital angular momentum quantum number $l = 0,\ 1,\ 2, \ldots,\ p-1$ (denoted s, p, d, f…)
- The magnetic quantum number $m_l = 0,\ \pm1,\ \pm2, \ldots,\ \pm l$
- The spin quantum number $m_s = \pm 1/2$

The three first quantum numbers define the orbitals in which the electron can be found. These are probability distribution functions around the nucleus, that have different shapes depending on the combination of quantum numbers considered. The spin quantum number can be seen as the spinning direction of the electron, which has two possible values. Each unique set of quantum numbers therefore defines a possible state for the electron, such that there are *degenerate states* that have a different combination of quantum numbers, but are at the same energy level. We therefore define the *degeneracy* g [-] as the number of states that correspond to the considered energy level. In the case of a single electron as considered here, we have $g = 2p^2$. Table 2.1 provides the first 28 states an electron can find itself in according to these notations.

[2] Although usually denoted by n, it will here be denoted by p to avoid confusion with the number density.

Table 2.1 Electron state classification

p	1	2				3								
l	s	s	p			s	p			d				
m_l	0	0	-1	0	1	0	-1	0	1	-2	-1	0	1	2
m_s	$\pm\frac{1}{2}$	$\pm\frac{1}{2}$	$\pm\frac{1}{2}$	$\pm\frac{1}{2}$	$\pm\frac{1}{2}$	$\pm\frac{1}{2}$	$\pm\frac{1}{2}$	$\pm\frac{1}{2}$	$\pm\frac{1}{2}$	$\pm\frac{1}{2}$	$\pm\frac{1}{2}$	$\pm\frac{1}{2}$	$\pm\frac{1}{2}$	$\pm\frac{1}{2}$
N# of states ($2p^2$)	2	8				18								

Atomic structure

When there are multiple electrons involved in the potential field, the problem becomes more complicated as there are coupling mechanisms between the angular momentum and the spin of the electrons. The same quantum numbers are however kept to characterize an orbital. The ground state configuration for Argon is denoted

$$1s^2\ 2s^2\ 2p^6\ 3s^2\ 3p^6$$

It shows the number of electrons filling each (p, l) doublet. In addition to this information, there needs to be information about the angular momentum coupling of the electrons. This is given by the *term* symbol, which in the case of the ground state of Argon is

$$^1S_0$$

This additional term represents three additional quantum numbers

- The total orbital angular momentum quantum number $l^* = 0,\ 1,\ 2\ldots$ (denoted S, P, D, F…)
- The total spin angular momentum quantum number $m_s^* = 0,\ \frac{1}{2},\ 1,\ \frac{3}{2}, \ldots$
- The total angular momentum quantum number $J = (l^* + m_s^*),\ (l^* + m_s^* - 1),\ (l^* + m_s^* - 2), \ldots,\ |l^* - m_s^*|$

that are put together in the term symbol as

$$^{2m_s^*+1}l_J^*$$

and represents the coupling between the orbital angular momentum, and the spin angular momentum. An energy level is therefore entirely described by its configuration (orbitals in which the electrons reside), and term symbols denoting the angular momentum coupling between the electrons. The most stable configuration is the ground state, where the electrons are at the lowest possible potential energy. Excitation processes can increase the potential energy of a configuration either by changing the orbital in which an electron resides, or by affecting the angular momentum coupling situation (therefore only affecting the term symbol).

For convenience, in this work, the energy levels will be denoted by an alternative notation, to avoid the heavy configuration-term notation. It consists of indexing the energy levels with

an index starting from 0 (ground state) to 30 (last level for Argon before ionization), sorted by energy difference with the ground state. Ar(0) will therefore correspond to the ground state, followed by Ar(1), Ar(2) and so on until the highest energy level. A table of correspondance between the configuration-term notation and the local notation, as well as the Paschen notation used frequently in the literature, is available in Appendix A to avoid any confusion. These values of energy levels were extracted from the Atomic Spectral Database of the National Institute for Standards and Technology (NIST-ASD) [34]. It can be noted that Argon shows to have a large energy gap between its ground state and first excited state (11.5 eV), therefore requiring large inputs of energy for first excitation. Compared to that, the ionization energy is of 15.7 eV.

2.3.2 Excitation/de-excitation and ionization/recombination reactions

Energy can be transferred to atoms in many different ways. Section 2.2 introduced collisions by treating the case of elastic collisions. Collisions can also be inelastic, in which case part of the kinetic energy of the collision is transferred to the bound electrons, changing the electronic configuration of atoms or ions. This is only possible for the most energetic collisions, or collisions with reactive species.

An atom or ion can enter in collision with an ion, a neutral atom, or a free electron. Usually, electrons and ions are the ones leading to inelastic collisions because of the higher reactivity induced by their charge. They are also usually at higher temperatures (thus speeds) than neutrals, after being accelerated by electric and magnetic fields. At high neutral temperatures only are some neutral atoms fast enough to cause inelastic collisions.

Excited states can also be de-excited. As opposed to excitation processes, which are induced by an external input of energy, de-excitation can also take place spontaneously. This happens because a system (here an atom or ion) always tends to its configuration with the lowest potential energy. Spontaneous de-excitation takes place in the form of radiative decay: an atom's internal energy can drop from a higher state to a lower state by emitting a photon of energy equal to

$$\Delta E_{ul} = E_u - E_l = h\nu_{ul} \tag{2.39}$$

where u and l denote values respectively relative to the upper and lower levels, and ν_{ul} the frequency of the photon. These radiative emissions are the source of the emission spectra analyzed in this work. They will be discussed more in depth in Section 2.4. De-excitation can also take place because of an inelastic collision, where internal energy from the electronic reconfiguration is transferred to the kinetic energy of the colliding species.

The relevant excitation and de-excitation processes for Argon are given in Table 2.2 for collisional processes, and in Table 2.3 for the radiative processes.

2.3.3 Boltzmann population ratio

The *Boltzmann population ratio*, or Boltzmann distribution of excited states, gives the ratio of level u to level l in function of the temperature, for a gas or plasma that has reached equilibrium

Table 2.2 Collisional excitation and de-excitation processes

Electron impact excitation Electron impact de-excitation	$\mathrm{Ar}(l) + \mathrm{e}^- \leftrightarrows \mathrm{Ar}(u) + \mathrm{e}^-$
Electron impact ionization Three-body recombination	$\mathrm{Ar}(i) + \mathrm{e}^- \leftrightarrows \mathrm{Ar}^+ + e^- + e^-$
Heavy ion impact excitation Heavy ion impact de-excitation	$\mathrm{Ar}(l) + \mathrm{Ar}^+ \leftrightarrows \mathrm{Ar}(u) + \mathrm{Ar}^+$
Heavy neutral impact excitation Heavy neutral impact de-excitation	$\mathrm{Ar}(l) + \mathrm{Ar} \leftrightarrows \mathrm{Ar}(u) + \mathrm{Ar}$

Table 2.3 Radiative excitation and de-excitation processes

Spontaneous radiative decay	$\mathrm{Ar}(u) \longrightarrow \mathrm{Ar}(l) + h\nu$
Radiative recombination	$\mathrm{Ar}^+ + \mathrm{e}^- \longrightarrow \mathrm{Ar}(i) + h\nu$
Stimulated radiative decay	$\mathrm{Ar}(u) + h\nu \longrightarrow \mathrm{Ar}(l) + h\nu + h\nu$
Excitation by photoabsorption	$\mathrm{Ar}(l) + h\nu \longrightarrow \mathrm{Ar}(u)$

at temperature T:

$$\frac{n_u}{n_l} = \frac{g_u}{g_l} \exp\left\{-\frac{\Delta E_{ul}}{k_\mathrm{B} T}\right\} \tag{2.40}$$

This equation arises from statistical mechanics [24]. If the total population is n [m^{-3}], we can also write

$$X_i = \frac{n_i}{n} = \frac{g_i}{Z(T)} \exp\left\{-\frac{E_i}{k_\mathrm{B} T}\right\} \quad \text{with} \quad Z(T) = \sum_i g_i \exp\left\{-\frac{E_i}{k_\mathrm{B} T}\right\} \tag{2.41}$$

where X_i [-] is the molar fraction of level i. By taking the natural logarithm of this equation, we get

$$\ln(X_i/g_i) \propto -\frac{E_i}{k_\mathrm{B} T} \tag{2.42}$$

It is important to note that this proportionality relation holds only for gases or plasmas in states of complete equilibrium, where the electrons, ions and neutrals are at the same temperature T.

A common way to display the population of excited states is therefore to use the proportionality relationship of Equation 2.42, in the form of a Boltzmann plot such as the one shown in Figure 2.9. In this plot, each dot corresponds to an excited state. We see that they are all aligned on a line, of which the slope is $-1/(k_\mathrm{B} T)$.

As discussed in subsection 2.2.4, a low density plasma can find itself in a state at which the electrons, ions and neutrals have a different temperature. Neutrals at a low temperature can therefore be excited to higher states by collisions, leading to a population distribution that does not follow Equation 2.40. In such a case, it is still common to plot the population densities of the excited states on a Boltzmann plot. However, the populations would not be perfectly aligned as for the equilibrium case, there would be some scattering with respect to the best

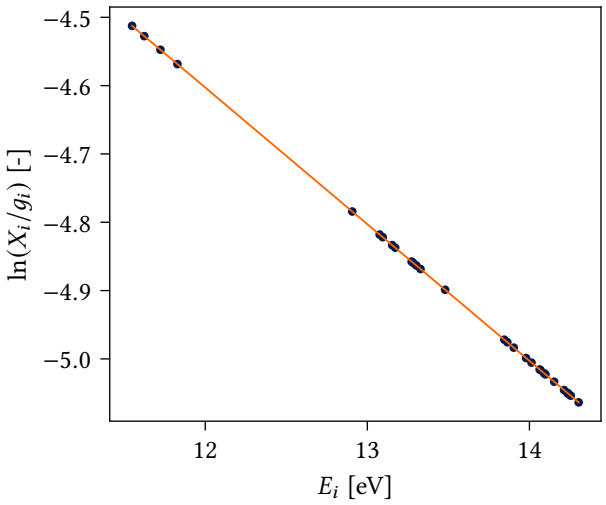

Figure 2.9: Boltzmann plot for Argon in thermal equilibrium at $T = 5$ eV (zoom on the 30 excited states).

fitting line. We will use such plots to characterize the population distributions of the excited states obtained with the CR model.

2.4 Radiation

The diagnostics method used in this work relies on measurements of light emitted by the excited states. To effectively interpret the measured spectra, it is necessary to have an understanding of the physics governing radiation and atomic emissions. This section has the objective of providing the necessary information for the description of radiative processes in plasmas.

Light is an electromagnetic wave, that propagates through space at the speed of light, which is exactly $c = 299\,792\,458$ m/s. Light can also be seen as a flux of photons, containing each a discrete amount of energy. Its energy content is characterized interchangeably by its frequency ν [s^{-1}], or its wavelength λ [m], such that

$$E = h\nu = h\frac{c}{\lambda} \tag{2.43}$$

Small wavelengths correspond to energetic electromagnetic waves, whereas larger wavelengths are less energetic. The window of wavelengths corresponding to visible light has bounds around $\lambda = 400$ nm for the most energetic visible light (violet light), and $\lambda = 700$ nm for the less energetic light (red light). Smaller wavelengths are ultraviolets, and larger wavelengths are infrareds. Any light emission can be decomposed by wavelength, showing the distribution of photons across the spectrum. This map corresponds to the emission spectrum of the source.

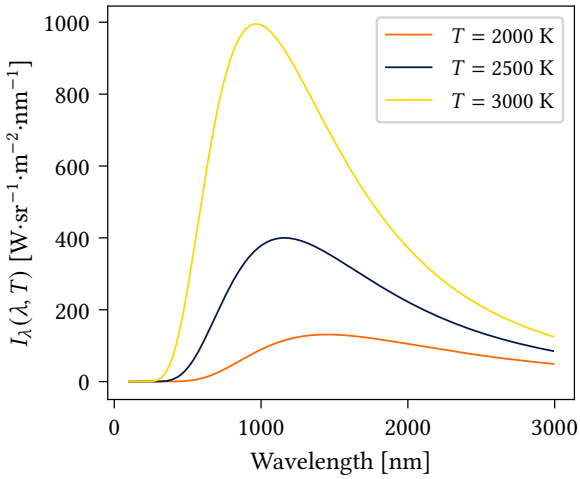

Figure 2.10: Black body spectral radiance for different temperatures

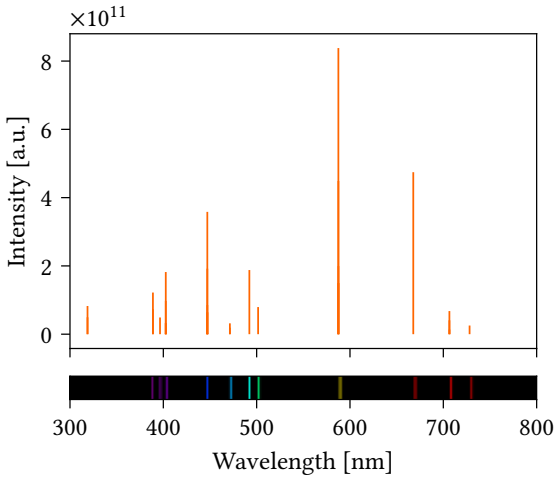

Figure 2.11: Emission spectrum of helium (spectral data extracted from NIST-ASD [34])

2.4.1 Black body radiation

A black body is an idealized physical object that absorbs all light incident to it, and emits radiation at all wavelengths. It emits light according to Planck's law

$$I_\lambda(\lambda, T) = \frac{2hc^2}{\lambda^5} \frac{1}{\exp\left\{\frac{hc}{\lambda k_B T}\right\} - 1} \tag{2.44}$$

where I_λ [W·sr^{-1}·m^{-3}] is the spectral radiance (power emitted per unit surface, solid angle, and wavelength). The black body emission spectrum therefore depends only on the temperature. Figure 2.10 gives this curve for different temperatures, showing that for hotter black bodies, the distribution shifts to higher energy photons, and the intensity is also increased.

2.4.2 Emission spectrum of an atom

Gases can be excited by excitation processes such as the ones discussed in subsection 2.3.2. The excited states can then spontaneously decay to lower levels by emitting a photon at the wavelength corresponding exactly to the energy difference between the upper and the lower level. This gives rise to emission spectra consisting of discrete emission lines, corresponding to the allowed transitions, and zero emissions at all other wavelengths. These emission spectra are unique to each gas, since each have their own set of allowed transitions. For atomic gases, such as argon or helium, the observed spectrum consists of precise lines corresponding to atomic transitions, as illustrated in Figure 2.11. For molecular gases, the spectra are more complex, because molecules also have rotational and vibrational energy levels, which are more closely packed together.

Transition probability

The stability of excited states affects the rate at which the radiative decay occurs. Some transitions are much more frequent than others, and some are even not permitted at all by quantum

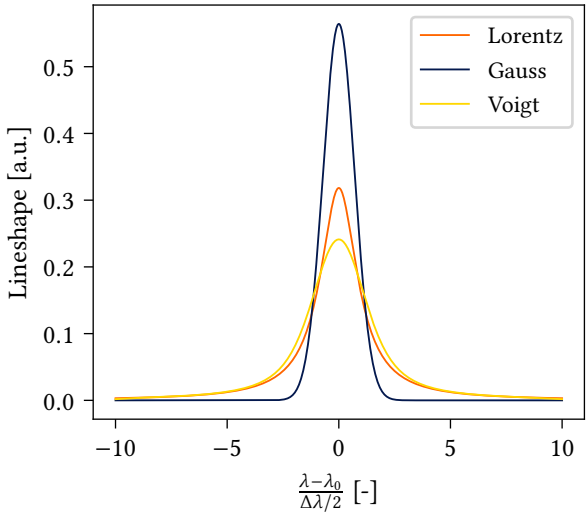

Figure 2.12: Emission line broadening lineshapes

mechanics. There are *selection rules* that allow only certain transitions. To be possible, a transition must verify

- $\Delta l^* = 0,\ \pm 1$
- $\Delta m_s^* = 0$
- $\Delta J = 0,\ \pm 1$ (except $J = 0$ transitions, which are forbidden)

For those that verify the selection rules, the frequency of transition is quantified by the *Einstein coefficients* A_{ul} [s^{-1}], for the transition from upper state u to lower state l. They can be obtained with quantum mechanical calculations. Their values are also listed in the NIST-ASD database [34].

Line broadening

In practice, all measured emissions are not at the exact wavelength corresponding to the transition. There are several broadening mechanisms, which impact the distribution of photons around the theoretical wavelength. These mechanisms lead to different lineshapes for the emission lines, represented in Figure 2.12 around the theoretical wavelength λ_0, for a unit half width at half maximum (HWHM) $\Delta\lambda/2 = 1$, and normalized such that their integral is equal to 1. The most important broadening mechanisms are

- *Natural line broadening:* This type of broadening is due to the Heisenberg uncertainty principle, which can relate the finite lifetime of the excited states to the width of the energy level. This results in a given spectral width for the emission line. This mechanism spreads the emissions around wavelength λ_0 according to a Lorentzian lineshape. The HWHM in wavelengths is given by

$$\left(\frac{\Delta\lambda}{2}\right)_{\text{Natural}} = \frac{\lambda_0^2}{2\pi c} A_{ul} \tag{2.45}$$

- *Doppler broadening:* The emitting particles have a velocity distribution. Because of the Doppler effect, one knows that moving emitting particles therefore emit at a shifted wavelength, depending on the relative velocity towards or away from the observer (red-shifter if moving away from, and blue-shifted if moving towards the observer). For a Maxwell-Boltzmann distribution of speeds, the speed of particles along a given axis is given by a Gaussian distribution around zero. This results in a Gaussian distribution of the emissions around the theoretical wavelength. The hotter the gas, the wider the velocity range, thus the wider the spectral broadening. The HWHM for Doppler broadening is given by

$$\left(\frac{\Delta\lambda}{2}\right)_{\text{Doppler}} = \frac{\lambda_0}{c}\sqrt{2\ln 2}\left(\frac{k_B T}{m}\right)^{1/2} \tag{2.46}$$

  In addition to line broadening, the Doppler effect can also induce a Doppler wavelength shift $\delta\lambda$ if there is a bulk velocity v:

$$\frac{\delta\lambda}{\lambda} = \frac{v}{c} \tag{2.47}$$

- *Pressure broadening or Stark broadening:* The presence of other atoms or ions around can also affect the wavelength of the emitted photons. This takes place through 2 processes. The first is the fact that nearby atoms or ions interfere slightly with the electronic configuration of each other atom through their electric fields, such that the energy levels are slightly different from the single atom case from which the electronic level values are calculated. Collisions also affect the emission wavelengths, by changing the decay rate of the energy levels. Indeed, adding collisional de-excitation to radiative decay, energy level u decays at a frequency equal to the sum of the radiative decay frequency, and the collisional frequency. This leads to a thickening of the Lorentzian profile of natural broadening. The HWMH is proportional to $A_{ul} + \nu_{\text{coll}}$.

- *Instrument broadening:* The spectrometer used to decompose the emissions in function of their wavelengths has a finite wavelength resolution. This last effect can vary a lot depending on the spectrometer that is used.

These broadening mechanisms are combined, such that the total lineshape is usually a Voigt profile, which is the convolution product of a Gaussian profile and a Lorentzian profile.

2.4.3 Absorption

Gases can also interact with light emissions by absorbing photons. The Beer-Lambert law is the equation that relates the change in intensity with the medium and the optical path distance. It writes

$$T_\lambda = \left(\frac{I}{I_0}\right)_\lambda = \exp\{-\alpha_\lambda L\} \tag{2.48}$$

where T_λ [-] is the spectral transmittance, $(I/I_0)_\lambda$ the ratio between the measured spectral radiance and the emitted spectral radiance, L [m] the distance covered, and α_λ [m^{-1}] the spectral absorption coefficient. The latter depends on the gas through which the light is passing, and on the wavelength. Similarly to what was discussed about atomic emissions, atoms can absorb a photon if its wavelength corresponds exactly to the energy difference between the

current energy level of the atom, and a higher energy level, and if this transition is allowed by quantum mechanics. This results in absorption spectra with absorption lines at the same wavelengths as the emission lines, since the energy difference between levels and the allowed transitions are the same for both processes. Molecular gases will have more complex spectra due to the rotational and vibrational energy levels of molecules, but the principles are the same.

The product $\alpha_\lambda L$ [-] is known as the optical thickness. If it is close to zero, the transmissivity is close to unity. A gas can be said *optically thin* if the optical thickness is shown to be close to zero, meaning nearly all emissions go through this thickness unaffected.

2.5 Collisional-Radiative model for Argon

In the previous sections, the governing mechanisms inside the plasma were described in a general manner. In this section, several assumptions are made to identify the driving mechanisms inside the DRAG-ON facility, in order to build a 0-D reactor model of the plasma.

Such a model consists of a chemistry box model with the goal to predict the population of each energy level of Argon, in non-equilibrium conditions. This means that the populations do not follow the Boltzmann distribution, they are defined by the collisional and radiative mechanisms. The output of this model is the solution of a particle balance equation. Each excitation and de-excitation mechanism, from each energy level taken into account, introduces a rate coefficient that populates and depopulates energy states at a certain rate. This leads to a particle balance equation with the shape

$$\frac{dn_j}{dt} = \dot{\omega}_j \quad \forall j \in \mathcal{S} \tag{2.49}$$

where $\dot{\omega}_j$ [$m^{-3} \cdot s^{-1}$] is the net production rate of species j, and $\mathcal{S}$ is the set of all species taken into account in the CR model. In this section, we provide the list of species and mechanisms taken into account, in order to build Equation 2.49. This model is built to be compatible with *Mutation++* [22], an open-source C++ software, developed at the VKI, for the computation of physiochemical properties of plasmas.

The steady state solution of Equation 2.49 provides population densities, which are used to compute synthetic emission line intensities. This can be done only if the chemistry is assumed to be faster than the flow time of the considered plasma, which is checked in Section 2.6. It is this steady state synthetic spectrum that is used for comparison with the experimental results of Chapter 3.

First, the PFG is briefly described, to have a better knowledge of the conditions inside the transparent tube in which the spectroscopic measurements will be made. A discussion is then carried out for the processes to include in the model. Rate coefficients are finally determined for each of these reactions. The governing rate equation for each energy level can then be built.

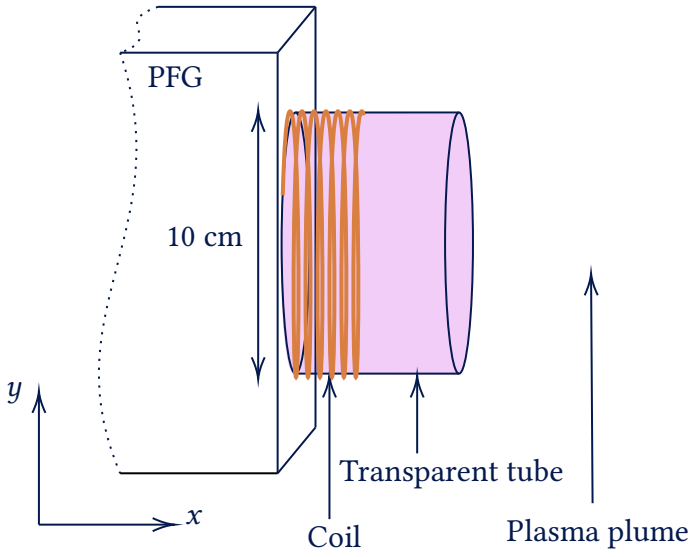

Figure 2.13: Particle Flow Generator (PFG)

2.5.1 Particle Flow Generator

Before making assumptions on the dominant processes, it is first important to describe what is known of the conditions in the zone in which we wish to model the reactions. The region in which the spectroscopy measurements are made is the transparent tube at the exit of the PFG, illustrated in Figure 2.13. This is therefore the region that we wish to model in the CR model. The known quantities in this region are listed in Table 2.4. The magnetic field value in the transparent tube is not known for confidentiality reasons, but it was estimated from the knowledge of the current in the focusing coil at the time of the experiment (0.5 A), and an order of magnitude for the number of turns. The constituting material of this tube is also not disclosed, but it is assumed to be totally transparent.

Table 2.4 Conditions inside the transparent tube

Quantity	Symbol	Value	Unit
Reference length	D_t	0.096	m
Background pressure	P_n	4×10^{-3}	Pa
Ambient temperature	T_n	20	°C
Ion along axis velocity	v_i	$\sim$ 8000	m/s
Magnetic field	B_t	$\sim 3 \times 10^{-4}$	T

2.5.2 Processes included in the CR model

A complete model would include all energy levels of Ar and Ar^+, and all processes listed in Table 2.2 and Table 2.3. However, the particularly low density conditions in DRAG-ON allow to make some simplifying assumptions, to lower the number of reactions needed in the model.

Neutral collisions

In the main chamber of DRAG-ON, the pressure is measured far from the PFG (close to the main chamber's upper surface). The measured pressure is therefore the pressure of the neutral Argon background gas, such that we can relate the measured pressure with the background gas number density with the perfect gas law

$$n_n = \frac{P_n}{k_B T_n} = 1 \times 10^{18}\ \mathrm{m}^{-3} \tag{2.50}$$

assuming that the background gas in the chamber has reached thermal equilibrium with the chamber wall at T_n. With the number density, it is possible to determine the mean free path of this background gas. Using Equation 2.21, and comparing to the reference length (approximately 10 cm diameter of the transparent tube), we get the Knudsen number

$$\mathrm{Kn} = 17.5 \tag{2.51}$$

using the hard sphere model, with sphere radius given by the van der Waals radius of Argon of 1.83 Å [35]. This gives an order of magnitude for the Knudsen number, showing that the majority of Argon atoms will fly out of the transparent tube before being subject to any collision with another neutral, since the mean free path is nearly 20 times larger than the diameter of the tube (the length is even smaller). This places the background gas in the free molecular flow regime, which means that the collisions between neutrals can be neglected in the CR model.

This assumption is reinforced by the fact that the background gas is at a low thermal kinetic energy. At this temperature, the Maxwellian distribution of speeds gives a most probable speed of $v_{mp} = 350$ m/s. This speed gives a most probable kinetic energy of $E_n = 0.025$ eV. This is too low to lead to collisional excitation by neutral collisions.

Electron collisions

Electrons on the other hand are highly energetic, and are therefore likely to excite Argon atoms with collisions. Two main factors make them more likely to actively excite the Argon atoms. High energy electrons tend to have a large cross section for excitation mechanisms, because their charge and kinetic energy make them likely to interact with the electronic configurations of the atoms they encounter. In addition, as opposed to neutrals, their trajectories are affected by the magnetic field generated by the coil wrapped around the transparent tube. This makes them follow a helical motion that allows them to cover more distance than by going in straight lines, which also increases their probability of collisions with Argon atoms. With the value of the magnetic field in the coil of Table 2.4, the cyclotron frequency defined in Section 2.1 can be computed as

$$\omega_{c,e} = \frac{|eB_t|}{m_e} = 5.28 \times 10^7\ \mathrm{rad/s} \tag{2.52}$$

which corresponds to 8.4 million revolutions per second, or a revolution period of 1.2×10^{-7} s. For the electrons with an axial velocity lower than 800 km/s (with a lifetime in the transparent tube larger than the revolution period), the helical motion will therefore increase the probability of collision with Argon atoms. There is no prior knowledge of the electrons' temperature and velocity distribution, but from their expected high kinetic energy and the presence of the

coil's magnetic field, they have to be considered in the model as a potential excitation mechanism. Electron impact ionization will however not be considered in this model. The ionization process is assumed to entirely take place in the PFG itself.

Ion collisions

As opposed to the electrons, the ions will not interact with the neutral background gas. They are also subject to a Lorentz force, which forces them to a helical motion around the magnetic field lines. However, because of their much larger mass than electrons, the revolution frequency is much higher. With the ion mass $m_\mathrm{i} = 6.63 \times 10^{-26}$ kg instead of the electron mass for the cyclotron frequency, we get

$$\omega_{\mathrm{c,i}} = \frac{|eB_\mathrm{t}|}{m_\mathrm{i}} = 728.2 \text{ rad/s} \tag{2.53}$$

This corresponds to revolutions with a period of 0.009 seconds. With the target axial speed of ions being 8 km/s, this gives a lifetime of less than 1.25×10^{-5} seconds. This implies that, at the length scale of the transparent tube, the ions move in straight lines axially. They then are quickly out of the influence of the magnetic field, so they continue in their straight trajectories.

The probability of collision can therefore be computed similarly to what was done for the neutrals. For this, we first need an estimation of the cross section for this type of collision. The cross section depends on the ion's kinetic energy. Assuming all ions are at the target accelerated speed $v_\mathrm{i} = 8$ km/s, their kinetic energy is then $E_\mathrm{i} = 13.2$ eV. The Phelps database from LXCat [33, 36] gives a cross section $\sigma_{\mathrm{i,n}} = 8.6 \times 10^{-20}$ m^2 for collisions between Argon neutral atoms and ions with this kinetic energy. Assuming the neutral atoms are not moving compared to the ions because of the large velocity differences between the two species, we can get the mean free path for the ions using Equation 2.20

$$\overline{\lambda}_\mathrm{i} = \frac{1}{n_\mathrm{n}\sigma_{\mathrm{i,n}}} \simeq 11.6 \text{ m} \tag{2.54}$$

Compared to the transparent tube's diameter and length of about 10 cm, this gives Kn = 116, showing that the probability for collision is very low, since the average ion needs to pass 116 times the diameter of the tube to collide with an Argon atom. For this reason, the ion impact excitation and ionization reactions will be ignored in this model.

Radiative processes

The Einstein A_{ul} coefficients inform us about the lifetime of a given excited state. These coefficients for the allowed transitions for Argon can be found in the NIST-ASD database [34], and are shown in Appendix A for the 45 transitions taken into account in the model. According to this data, the lifetimes of excited states before a radiative decay is between $1/\min(A_{ul}) \simeq 5 \times 10^{-5}$ s and $1/\max(A_{ul}) \simeq 2 \times 10^{-9}$ s, which is much smaller than the time it takes for an Argon atom at v_mp to leave the transparent tube (around 3×10^{-4} s). This confirms that radiative decay is a very active reaction in the considered region. All reactions listed in Table A.2 are taken into account in this model, with their rate coefficients simply given by the Einstein coefficients from the database. It is important to note that these rate coefficients are only known within a certain margin, which in the case of those considered in this model, lies

between ±25% of their value. Reactions with a larger error were ruled out to avoid propagating very large errors in the model, since they did not include any strong (often observed) lines. The several lines having an error between 10 and 25% however could not be ruled out because some are known to be frequently observed.

Absorption on the other hand is not considered in this model: the plasma will be assumed to be optically thin. This assumption is not straightforward to verify, as an estimation of the optical depth would require knowledge of the population of the quantum states. However, the assumption seems reasonable since the overall density is very low, such that the probability of a photon emitted in the tube to find an atom excited just at the right state to excite it by an allowed optical transition before exiting the tube, can be assumed to be very low and thus negligible.

2.5.3 Rate coefficients

The reactions included in the CR model are finally

1. Electron impact excitation and de-excitation

$$\mathrm{Ar}(l) + \mathrm{e}^- \rightleftarrows \mathrm{Ar}(u) + \mathrm{e}^- \quad \forall u > l \tag{2.55}$$

2. Spontaneous radiative decay

$$\mathrm{Ar}(u) \longrightarrow \mathrm{Ar}(l) + h\nu_{ul} \quad \forall u > l \tag{2.56}$$

Each of these reactions is characterized by a rate coefficient $\mathcal{K}$. Combined, they define the dynamics of the model. A rate coefficient is defined as the constant that, multiplied by the number densities of the reagents, gives the rate of production of the products.

Radiative decay rate coefficients

For the radiative decay reactions, the rate coefficients are naturally the Einstein coefficients according to

$$\mathcal{K}_{ul}^{\mathrm{rad}} = A_{ul} \tag{2.57}$$

with $\mathcal{K}_{ul}^{\mathrm{rad}}$ in $[\mathrm{s}^{-1}]$ such that, if there was only radiative decay, the population densities would vary in time according to

$$\frac{dn_i}{dt} = \sum_{j>i} A_{ji} n_j - \sum_{i>j} A_{ij} n_i \tag{2.58}$$

Electron impact excitation rate coefficients

For the electron impact excitation reactions, the rate coefficients can be related to the cross section of the reaction σ_{ij}. As mentioned earlier, the databases for collisions give the cross section in function of the electron kinetic energy, or speed. If all electrons were at the same speed, the rate coefficient for reaction r between energy levels i and j would simply be $\mathcal{K}_r^{\mathrm{ee}} = v_{\mathrm{e}}\sigma_{ij}$

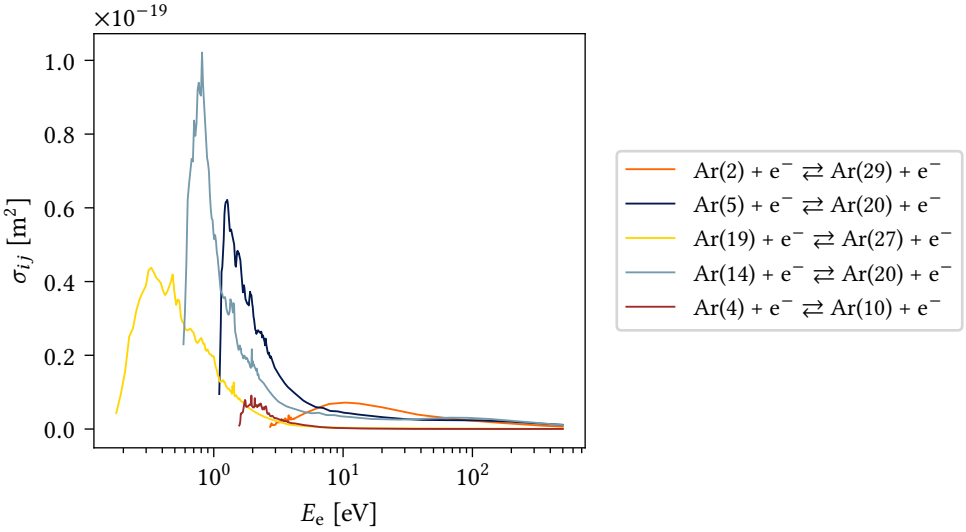

Figure 2.14: Cross section for electron impact excitation, in function of the electron kinetic energy, for several reactions. Data from [33, 37]

[m^3/s]. The actual rate coefficient has to take into account all possible speeds by integrating over the distribution of speeds of the electrons. This gives [24]

$$\mathcal{K}_r^{ee} = \int_{\Delta E_{ij}}^{\infty} \sqrt{\frac{2E}{m_e}}\, \sigma_{ij}(E)\, \hat{f}_e^E(E)\, dE \tag{2.59}$$

The lower bound of this integral is the difference of energy between energy levels i and j, since the electrons of lower energy than this threshold can not participate in this particular excitation reaction. A usual assumption for the electron energy distribution function (EEDF) is the Maxwellian distribution. For a rarefied plasma such as the one encountered in DRAG-ON, this assumption's validity is questionable, since the low number of collisions slows the convergence to a Mawellian distribution. Because of the recent commissioning of the facility however, no EEDF measurements are available, which is why a Maxwellian distribution is used for this first iteration of the CR model. Inserting Equation 2.30 in Equation 2.59, we get

$$\mathcal{K}_r^{ee}(T_e) = \int_{\Delta E_{ij}}^{\infty} 2E \sqrt{\frac{2}{\pi m_e}} \left(\frac{1}{k_B T_e}\right)^{3/2} \exp\left\{-\frac{E}{k_B T_e}\right\} \sigma_{ij}(E)\, dE \tag{2.60}$$

In order to solve this integral, one needs the cross sections $\sigma_{ij}(E)$ [m^2]. There exists several databases, but for this work it was chosen to use the results of Zatsarinny et al. [33, 37] with their *B-Spline R-matrix* (BSR) code. This method has proven itself an efficient way to compute atomic structures and collisional interactions between atoms and electrons or ions [38]. It was furthermore chosen because of its completeness, since cross sections were computed for a large range of electron energies, for all possible excitation processes (465 reactions in total for all 31 levels of Argon). The cross sections for a few reactions are shown in Figure 2.14. For each reaction, these curves are convoluted with the Maxwellian distribution of energy in order to compute the rate coefficient.

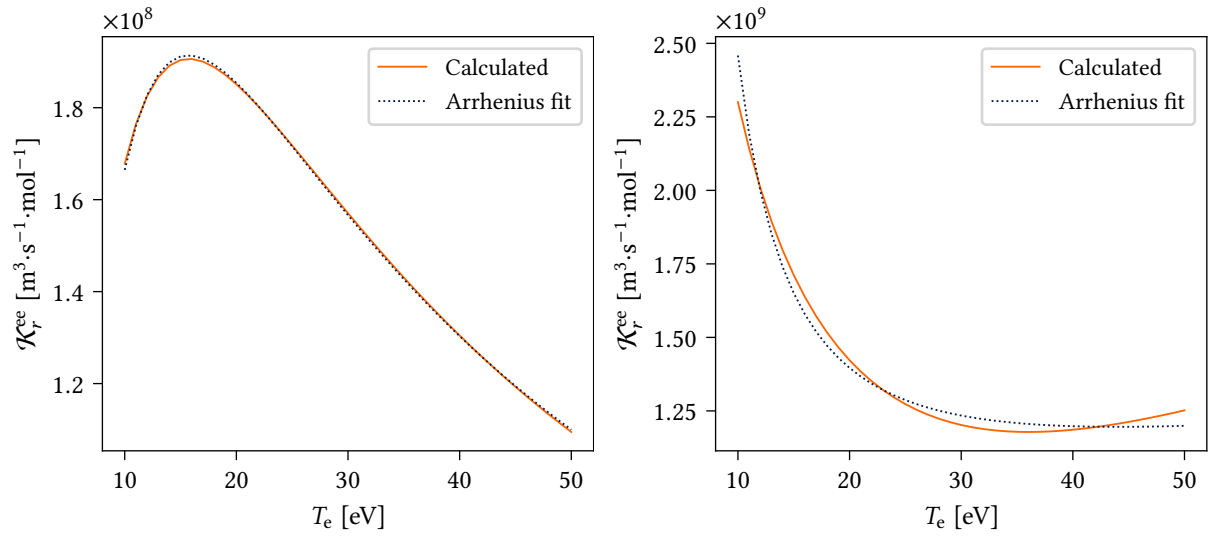

(a) $\mathrm{Ar}(0) + e^- \leftrightarrows \mathrm{Ar}(1) + e^-$ **(b)** $\mathrm{Ar}(14) + e^- \leftrightarrows \mathrm{Ar}(16) + e^-$

Figure 2.15: Comparison of the actual rate coefficient with the Arrhenius form fitting for two electron impact excitation reactions (a) with a typical fitting error of 0.8% and (b) worst case

Since the cross sections are given for *excitation* collisions, Equation 2.60 gives a *forward* rate coefficient, which will be denoted by the subscript f. This rate coefficient is a function of the electron temperature T_e, since the electron energy distribution is a function of T_e. The goal of this work is to determine T_e by using the CR model at different values of T_e, and finding which output fits best the experimental results. It is therefore convenient to avoid solving the integral of Equation 2.60 each time a new electron temperature is tested. It was decided to compute $\mathcal{K}_{f,r}^{ee}(T_e)$ for a range of electron temperatures, and to reduce this curve to a low number of parameters by carrying out a least square fitting to an analytical curve. For compatibility with Mutation++, this analytical expression was chosen to be an Arrhenius form for the rate coefficients

$$\mathcal{K}_{f,r}^{ee}(T_e) \simeq G_r T_e^{\eta_r} \exp\left\{-\frac{E_{a,r}}{k_B T_e}\right\} \tag{2.61}$$

where the parameters for the fit of reaction r are G_r [m^3/s], η_r [-] and $E_{a,r}$ [J]. Doing this curve fitting to an Arrhenius form for all 465 electron excitation reactions, we obtain results similar to what is shown in Figure 2.15, for each reaction r. The results shown in this figure are for a range of electron temperatures between 10 and 50 eV, but it can be done similarly for different ranges. The rate coefficient is also multiplied by the Avogadro constant for compatibility with Mutation++ units.

These fits are useful for the evaluation of the rate coefficients, but they induce an additional error in the model, since no fit is perfect. The statistics over all reactions for the errors on the fits are given in Table 2.5, for the 10 to 50 eV electron temperature range. The error estimate used for the statistics is the infinite norm of the relative error $||\varepsilon_r||_\infty$ for each reaction, defined as

$$||\varepsilon_r||_\infty = \max \frac{\left|\mathcal{K}_{f,r}^{ee}(T_e) - G_r T_e^{\eta_r} \exp\left\{-\frac{E_{a,r}}{k_B T_e}\right\}\right|}{\mathcal{K}_{f,r}^{ee}(T_e)} \quad , \text{ for } \; (T_{e,\min} \leq T_e \leq T_{e,\max}) \tag{2.62}$$

Table 2.5 Statistics of the fitting errors for the rate coefficients, for 10 eV $\leq T_e \leq$ 50 eV

Maximum [%]	6.9
Average [%]	1.1
Median [%]	0.8
Standard deviation [%]	0.9
# reactions with $\|\|\varepsilon_r\|\|_\infty > 5$ **%**	2

This error estimate shows that fitting the rate coefficients to an Arrhenius form do not introduce a large error in the model. Most reactions have a maximum fitting error lower than 1%. Only two reactions reach errors larger than 5% (worse case displayed in Figure 2.15b). Because of the severe error definition chosen (infinite norm), this means that 5% errors only occur for two reactions, if the rate coefficients are evaluated at their worse fitting temperature. Usually, this worse fitting temperature is the lowest temperature. These orders of magnitude for the fitting errors were respected for each tested temperature interval. It was observed that the errors remain small if the chosen electron temperature range was small (a few electron-volts) for the estimation the rate coefficients at temperatures lower than 5 eV. For larger minimum temperatures, larger intervals can be taken without introducing a large fitting error (as shown with the 10–50 eV interval). These low errors due to the fitting must however be interpreted with caution, as the cross sections the rate coefficients are based on have uncertainties that can reach 50 to 100%. The uncertainty on the rate coefficients is therefore not limited to the uncertainty on the fitting, but dominated by the low reliability of the cross sectional data.

Electron impact de-excitation rate coefficients

The backward rate coefficients for the electron impact excitation reactions, denoted by subscript b, are computed internally by Mutation++ according to the principle of detailed balance, which states that at equilibrium, the forward reaction is exactly balanced by the reverse process [22]:

$$\mathcal{K}^{ee}_{f,r} n_e n_u = \mathcal{K}^{ee}_{b,r} n_e n_l \tag{2.63}$$

The population ratio of the excited states not being known before solving the equation, it is assumed that the excited states are populated according to the Boltzmann population ratio of Equation 2.40 at the electron temperature. This results in the de-excitation rate coefficient being computed with

$$\mathcal{K}^{ee}_{b,r} = \mathcal{K}^{ee}_{f,r} \frac{g_u}{g_l} \exp\left\{-\frac{\Delta E_{ul}}{k_B T_e}\right\} \tag{2.64}$$

2.5.4 Rate equation and estimation of the line intensities

With the species and the reactions between them clearly identified, the rate equation for the evolution of the population of each species can be developed. The species are the 31 Argon energy levels of Table A.1. The reactions allowing to jump from one energy level to the other are 45 spontaneous radiative decay reactions, for which the rate is given by the Einstein A_{ul} coefficients listed in Table A.2, and the 465 electron impact excitation reactions for which the rate coefficients can be evaluated from Arrhenius coefficients calculated beforehand, and the

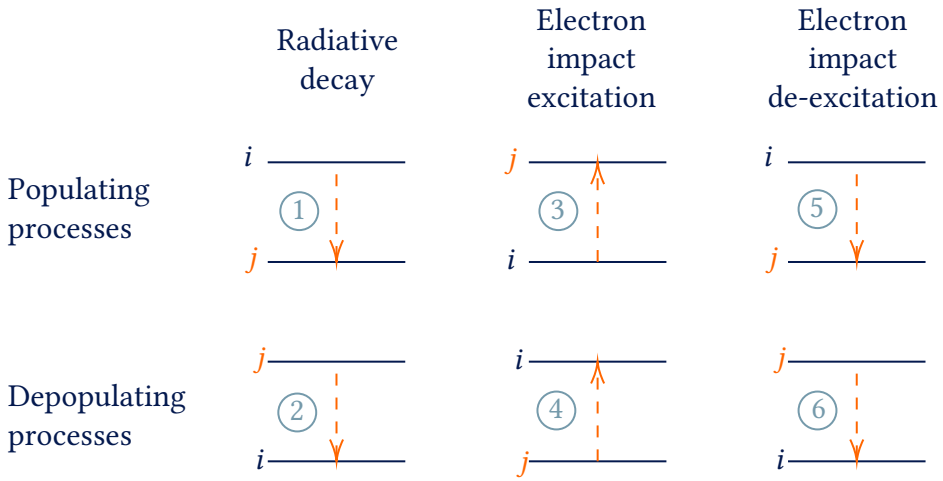

Figure 2.16: Illustration of the different terms of the rate equation

electron temperature. The backward rate coefficients can then be computed directly from the forward coefficients.

The rate equation is obtained by stating that the evolution in population of an energy level is governed by the sum of the production rates of all the reactions by which this level is produced, minus the sum of the production rates of all reactions by which this level is consumed. For level j, it can be written as

$$\frac{dn_j}{dt} = \sum_{j<i} A_{ij} n_i - \sum_{j>i} A_{ji} n_j + \sum_{r \ni j>i} \mathcal{K}^{\mathrm{ee}}_{f,r} n_\mathrm{e} n_i - \sum_{r \ni j<i} \mathcal{K}^{\mathrm{ee}}_{f,r} n_\mathrm{e} n_j + \sum_{r \ni j<i} \mathcal{K}^{\mathrm{ee}}_{b,r} n_\mathrm{e} n_i - \sum_{r \ni j>i} \mathcal{K}^{\mathrm{ee}}_{b,r} n_\mathrm{e} n_j \quad (2.65)$$

The different terms correspond to the following reactions, in order from 1 to 6 (as illustrated by Figure 2.16):

1. Radiative decay of upper levels i to level j, therefore populating level j proportionally to the Einstein coefficient of the reaction and the populations of upper levels i.
2. Radiative decay of level j to lower levels i, proportionally to the population of level j and the Einstein coefficients.
3. Excitation of lower levels i to level j, by electron collision, therefore populating level j.
4. Excitation of level j to upper levels i, by electron collision, depopulating level j.
5. De-excitation of upper levels i to level j, by electron collision, populating level j.
6. De-excitation of level j to lower levels i, by electron collision, depopulating level j.

The model therefore consists of a system of 31 coupled ordinary differential equations, that can be solved numerically provided the electron temperature for the rate coefficients, the electron number density, the total Argon number density and the initial conditions for the level populations:

$$\left.\begin{array}{c} T_\mathrm{e} \\ n_\mathrm{e} \\ n_\mathrm{n} \\ n_j(t=0)\ \forall j \end{array}\right\} \rightarrow \boxed{\text{CR model}} \rightarrow n_j(t)\ \forall j$$

Line intensities

Line intensities can be computed based on the number density of the excited states of interest. The intensity of a spectral line is indeed proportional to the energy of the emitted photons (therefore inversely proportional to the wavelength), the rate of emissions, and the population of the emitting energy level. It is given by

$$I_{ul} = \frac{hc}{\lambda_{ul}} \frac{1}{4\pi} A_{ul} n_u \tag{2.66}$$

where I_{ul} has units of $[\mathrm{W{\cdot}sr^{-1}{\cdot}m^{-3}}]$. This will allow a comparison to the laboratory measurements of Chapter 3.

Time to steady state

In order to compute line intensities, we therefore need a single value for the population of each excited state. The time dependent solution of Equation 2.65 must therefore be reduced to a single value for the prediction of the line intensities. After a sufficient amount of time, all $n_j(t)$ stabilize to a steady state density. In the literature, most papers assume that this time to steady state (chemical timescale) is small enough to be negligible compared to the time the species spend in the reactor (Lagrangian timescale). This allows to assume the density of each excited state is equal to the density at steady state. This is true in high density cases, where the collision rate is very high. In a low density reactor such as the one simulated here, the excitation rates are much smaller such that it can take a significant amount of time to reach $dn_j/dt = 0$ for all levels. The next section will therefore look at the dynamics of the CR model results, to check the validity of this assumption but also to investigate the effect of each input of the model on the steady state populations in the plasma.

It is important to note that the steady state reached in the present CR model when $dn_j/dt = 0$ does not correspond to equilibrium of the system. At equilibrium, the population densities would simply be obtained with the Boltzmann population distribution. In the present model, the electrons and neutrals are considered as two sets of particles that interact by collisions, exciting Argon, but the momentum transfer between them are considered to be negligible because of the small mass of the electrons. The computed densities are therefore non-equilibrium densities, with electrons and neutrals at their own distinct temperatures.

Initial conditions

The initial conditions $n_j(t = 0)$ are throughout this work defined as

$$n_0(t = 0) = n_\mathrm{n} \quad , \quad n_j(t = 0) = 0 \; \forall j \neq 0 \tag{2.67}$$

where n_0 is the number density of the ground state of Argon. This means that all excitation has to be performed through electron collisions. Before the effect of the electrons, no Argon atom finds itself in a higher energy state than the ground state. These are reasonable initial conditions, since at ambient temperature ($T_\mathrm{n} = 300$ K), the Boltzmann distribution gives the highest molar fraction (other than the ground state), of the order of $X_1 = n_1/n_\mathrm{n} = 10^{-194}$, which confirms that all the Argon gas has to be excited from the ground state.

2.6 Dynamics of the CR model

In this section, we analyze first results of the constructed CR model, to better grasp its behaviour and the effect of each input parameter on the calculated energy level densities.

2.6.1 Time to steady state

When solving Equation 2.65 as it is, we obtain the time evolution of the densities of each energy level. This time evolution depends largely on the electron number density. Indeed, more electrons lead to more excitation, and more excitation makes the system reach steady state faster. Since there is no prior knowledge of the electron number density inside the transparent tube, several orders of magnitude for electron densities were tested to see the range of chemical timescales that could be observed.

It was observed that the chemical timescale decreased by one order of magnitude when the electron density was increased by an order of magnitude, since $dn_i/dt \propto n_e$. The results are displayed in Table 2.6, where the observed time to steady state is also compared to the flow timescale with the Damköhler number

$$\mathrm{Da} = \frac{\text{flow timescale}}{\text{chemical timescale}} \tag{2.68}$$

with the flow time scale being equal to 3×10^{-4} s (the time it takes for an Argon atom at the most probable speed of 350 m/s to cross the diameter of the transparent tube). A Damköhler number much higher than 1 indicates that the chemistry can be considered instantaneous. On the other hand, a Damköhler number smaller than unity means that the observed emissions do not correspond to the steady state densities of the reactor. The simulations in Table 2.6 were carried out with electron temperature of 25 eV, and a neutral Argon number density of 10^{18} m^{-3}, corresponding to the measured pressure in the chamber.

Table 2.6 Evolution of the timescale to steady state

Electron number density [m^{-3}]	10^{15}	10^{16}	10^{17}	10^{18}
Time to chemical equilibrium [s]	2×10^{-2}	4×10^{-3}	1×10^{-4}	1×10^{-5}
Damköhler number [-]	0.015	0.075	3	30

The time evolutions of the level populations in the cases with the most and the less electrons are shown in Figure 2.17. This figure shows clearly the slower chemistry in the lower electron density case. It also shows that having more electrons has an important effect on the balance found between the excited states: high energy states are being excited by the larger number of high energy electrons.

For the comparison to experimental line intensities, care must therefore be taken concerning the values of population densities taken for the computation of synthetic line intensities, because depending on the electron density, the chemical timescale might not be negligible compared to the flow timescale. It will however be shown in Chapter 4 that the electron densities matching best the experimental lines are of the order of magnitude of $n_e = 10^{18}$ m^{-3}. This

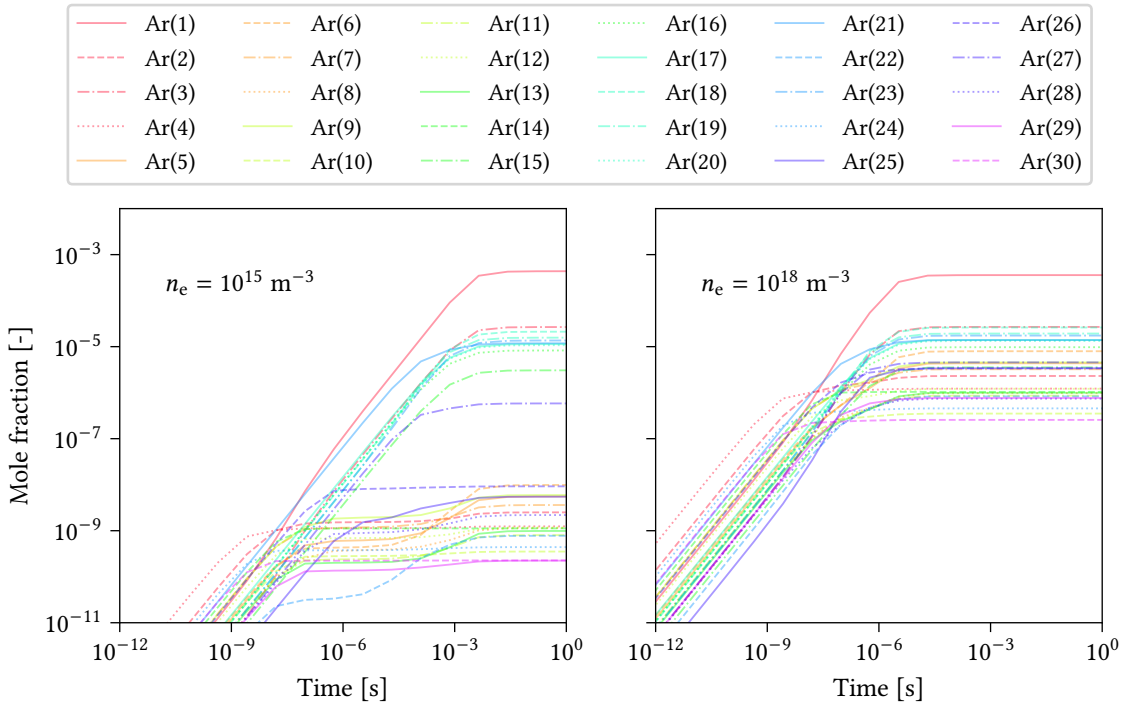

Figure 2.17: Kinetics of the CR model for two electron density conditions

therefore allows to assume instantaneous chemistry, allowing to use the steady state densities as the actual densities in the reactor.

2.6.2 Effect of the plasma parameters on energy level populations

An interesting aspect is to look at the effect of each plasma parameter on the populations of the energy levels of Argon. This is illustrated through Boltzmann plots, as defined in subsection 2.3.3. Since we solve for non-equilibrium conditions, we expect scattering of the energy level populations. A trend for the level of excitation can however be extracted from the best fitting line through the excited states. A steep slope corresponds to a lower excitation level, while a more horizontal slope corresponds to higher excitation. In this section, we assess the effect of the electron temperature, electron density, and neutral Argon density on the steady state populations of the energy levels.

Electron temperature: The electron temperature affects the electron energy distribution function. Higher electron temperature increases the number of electrons with a high enough energy to participate in the excitation reactions, therefore leading to larger rate coefficients. It is therefore expected to observe higher excitation at higher electron temperatures, which aligns with the results in Figure 2.18.
It can however be seen that as the electron temperature gets larger, the effect of increasing further the electron temperature is less notable. A similar observation was made by Ben Slimane [39] for a Xenon CR model. This means that at high electron temperatures (above 15 eV), the sensibility of the steady state populations to T_e is lower.

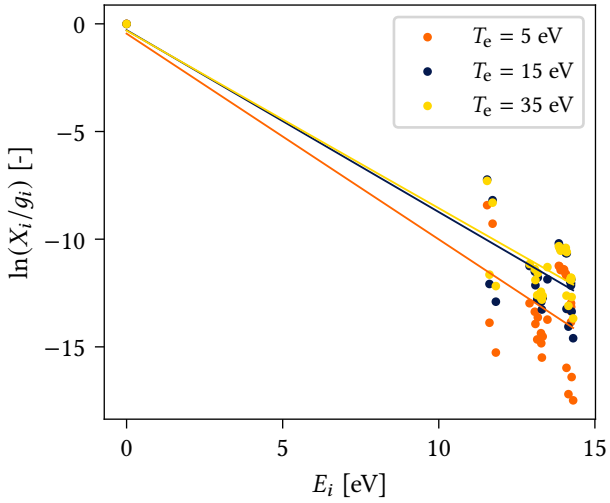

Figure 2.18: Effect of T_e on the steady state energy level populations. Results obtained with $n_e = n_n = 10^{18}$ m^{-3}.

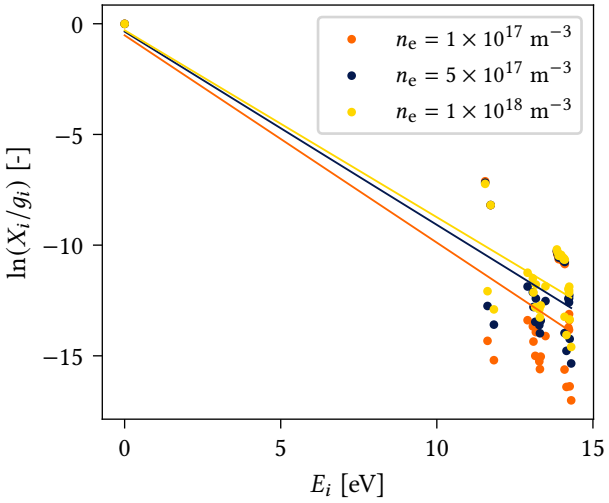

Figure 2.19: Effect of n_e on the steady state energy level populations. Results obtained with T_e = 15 eV and $n_n = 10^{18}$ m^{-3}.

Electron density: In addition to modifying the kinetics of the CR model, the electron density n_e also has an effect on the steady state populations of the excited states. It indeed changes the balance between the reactions of Equation 2.65. A high electron density increases the rate of collision with electrons, therefore leading to a plasma with more populated excited states, as depicted in Figure 2.19.

Argon density: Increasing the Argon density n_n however has no influence on the relative populations of excited states. This is an expected result, since it results in multiplying all terms of the governing rate equation by the same constant. It however influences the computed synthetic line intensities proportionally, as increasing the number density of Argon increases the number of emitting atoms. This influence on the line intensities is however irrelevant in this work, because the comparison to the experiment will provide relative intensity measurements.

2.7 Conclusion

This chapter provided the necessary understanding of the physical and chemical processes in action in a plasma. This allowed to build a functioning CR model, capable of computing populations of excited states of Argon based on a set of plasma parameters. From these energy level populations, synthetic line intensities can be obtained. The electron temperature and density were identified as being the key parameters, that actually have an effect on the population distribution of the excited states, thus on the synthetic line intensities. The important scattering of the energy level populations compared to a linear distribution on Boltzmann plots illustrates the far from equilibrium conditions that can be modeled with the present CR model.

Chapter 3 will provide information on how the measurements were made in the DRAG-ON facility, to have measures of line intensities comparable to what is obtained with the CR model.

Chapter 4 will then iterate on the main plasma parameters, to find which match the experimental results best, according to a chosen criterion.

CHAPTER 3

Optical Emission Spectroscopy

This chapter intends to provide a detailed description of the experimental setup and methodology for the Optical Emission Spectroscopy (OES) measurements in the DRAG-ON facility, as well as the experimental results. The goal of this experiment is to obtain, for each measured emission line of Argon, a radial distribution of line intensity.

Section 3.1 provides a theoretical background in OES, including the theory behind spectroscopy itself and its application to plasma diagnostics. The information in this section is based on Chen's discussions [21] on OES as a plasma diagnostics technique. The more specific information about optics is based on the Handbook of Optics, edited by Bass [40]. Section 3.2 then describes the experimental setup for OES measurements, including details on the various instruments used during the test. Section 3.3 then focuses on the calibration of the spectrometer, which is a crucial step in obtaining reliable measurements. Finally, Section 3.4 provides the procedure followed for the tests. The data preprocessing procedure is then described step by step. The results are finally presented and discussed.

Overall, this chapter provides a thorough description of the methodology used for the OES measurements in the DRAG-ON facility. The goal is to give the reader an understanding of the experimental setup and method, as well as the potential sources of error, and to present the results to which the CR model predictions are compared to.

3.1 Principles of spectroscopy for plasma diagnostics

OES is widely used for plasma diagnostics. It consists of decomposing plasma emissions spectrally, and to derive information about the emitting plasma based on the measured spectrum. The main advantage of this method is being non-invasive: the measurements can be made at a distance, by capturing the photons emitted by the plasma. The measurement technique therefore does not interfere with the measured quantity. In addition, for plasmas confined in high vacuum chambers like in DRAG-ON, this allows to change the setup, or make measurements at different points, without having to break the vacuum each time. It is therefore a rather cheap diagnostics technique. This section reviews the principles behind this measurement method for a better understanding of the results.

3.1.1 Spectral decomposition of light

Before interpreting any emission spectra, it is necessary to understand the way a spectrometer decomposes incident light by wavelength. This can be done using a prism, using the fact that the refraction index inside the prism depends on the wavelength of the light passing through

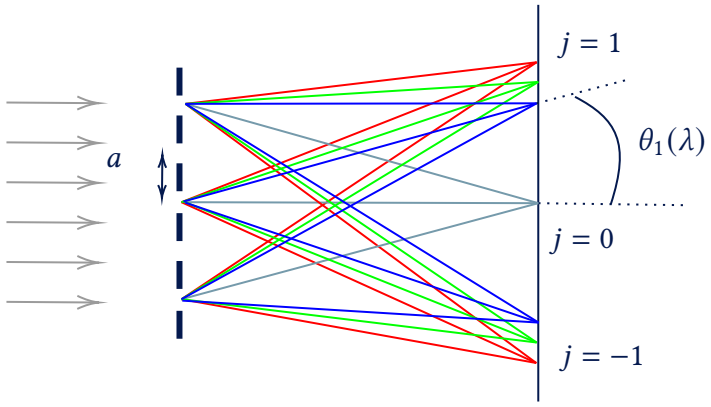

Figure 3.1: Polychromatic light dispersion by a grating

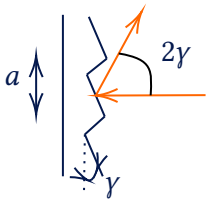

Figure 3.2: Blazed grating

it. Each wavelength therefore exits the prism with a different angle, therefore decomposing an incident beam into its wavelengths. While prisms are still used today for some applications, most spectrometers now use gratings.

Dispersion by a grating

Gratings consist of a very fine periodic pattern on a surface, that can work either by reflection or transmission. In both cases, it can be seen as an array of very thin slits, diffracting incident light. When incident light passes through this array, each slit acts as a point source, separated by distance a. All the resulting spherical waves added together lead to interference patterns for each wavelength component of the incident light. For monochromatic incident light, the resulting interference pattern behind the grating is a series of dots, symmetrically distributed with respect to the central, brightest dot. All space in between receives no light because of destructive interferences between all point sources from the grating. The angles between the centerline and the dots θ_j depends on the wavelength λ, and are given by

$$a \sin \theta_j = j\lambda \tag{3.1}$$

where $j = 0, \pm 1, \pm 2 \ldots$ is the order of the dot (zero for the dot on the centerline, ± 1 for the closest ones, and so on). For polychromatic light, each wavelength contribution of the source makes its own set of dots, separated by their own angles $\theta_j(\lambda)$, as illustrated in Figure 3.1. It can therefore be seen that, by placing detectors around the order $j = 1$, one can measure the intensity of light spectrally. A good grating is one that has a small enough distance between slits for the angular separation between the orders to be large, such that the spectral decomposition does not overlap between the other orders. A drawback compared to prisms is that an important fraction of the incident power can be lost to the other orders, reducing the measured signal. This problem is reduced by using *blazed* gratings (Figure 3.2), which is a special kind of reflective grating that can be designed to concentrate all light to the first order for a target wavelength λ_0, if the following equality is verified

$$a \sin(2\gamma) = \lambda_0 \tag{3.2}$$

This is the type of grating used in practice in this work. The emission intensity being very low, we can not afford to lose part of the emissions to orders that do not arrive on the detectors.

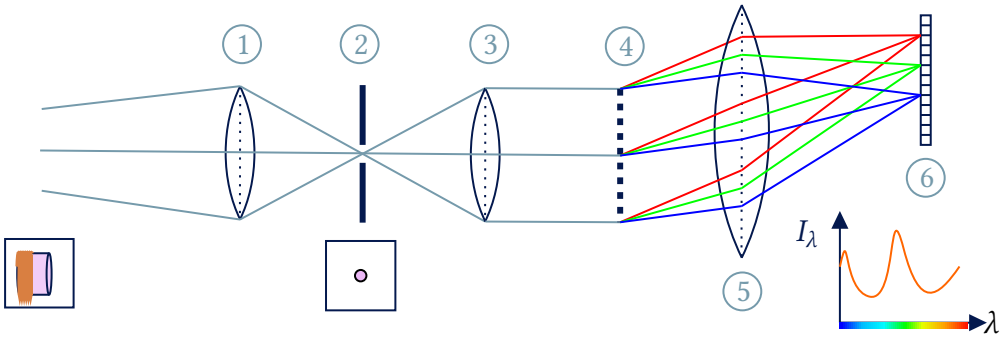

Figure 3.3: Schematic of a the main components of a generic spectrometer

Generic spectrometer

A grating alone is not sufficient to have a functional spectrometer. Figure 3.3 gives the different components of a generic spectrometer. Following the numbering of this figure, the main components of a spectrometer are

1. The *collecting optics*, which can be of many different forms (mirrors or lenses of different shapes) but in all cases have the role of focusing the incident rays to a focal point, either directly in a slit or through optical fiber, which leads to the slit.

2. The *slit* has the role of reducing the amount of light entering the spectrometer. For this work, the slit consists of a very small hole, reducing the collimated image to nearly a point, which will be spread spectrally. In other contexts, the slit can be a longer but thin aperture, reducing the image to a 1-D line. This dimension reduction is necessary because the spectral dispersion will take an additional dimension, and since the sensor can only be 2-D, the slit can only let an image of maximum 1 dimension in the spectrometer. The size of the slit influences the resolution of the spectrometer. The smaller the slit, the sharper the spectral resolution. For emission spectra, a good resolution is necessary to see the difference between close emission lines, but also to avoid changing the lineshape of the lines. This however comes at a price: the smaller the slit, the less light enters the spectrometer. For very dim emissions such as the ones encountered in DRAG-ON, a compromise has to be made between resolution and strength of the signal.

3. *Collimating optics* ensure a uniform incident angle on the grating. This is necessary for the dispersion to be only a function of the wavelength, and not of the incident angle.

4. The *grating* itself, discussed earlier, is the component actually splitting the incident light spectrally.

5. The *refocusing optics* focus the nearly parallel rays of same wavelength, to focus them on the sensor.

6. Finally, the *sensor* measures the amount of photons incident to it. It consists most often of a Charge Coupled Device (CCD) sensor, either in a linear configuration (for point measurements split in one dimension for the wavelength, in which case one pixel corresponds to one wavelength), or in a matrix configuration (one pixel dimension is for the image dimension, and the other is for the wavelength dimension).

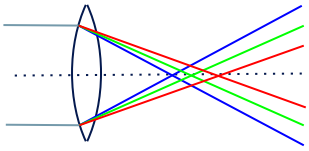

Figure 3.4: Chromatic aberration

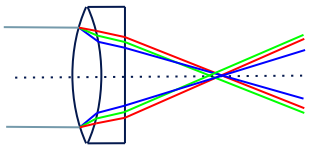

Figure 3.5: Achromatic doublet

In practice, most spectrometers use mirrors where possible, instead of lenses. Mirrors have the advantage of suppressing all chromatic aberrations that can be observed with lenses. Indeed, lenses work by refraction, and much like prisms, their refraction index depends on the wavelength. This leads to an often small but sometimes problematic dispersion of the light passing through the lens, as illustrated by Figure 3.4. These aberrations have an important impact on the measurements for applications such as spectroscopy, which is why mirrors are most often used for this application.

For cases where using a mirror is impractical, special assemblies can be used to reduce this effect, called *achromatic doublets*. They are a pair of lenses made of different materials, glued together. The role of the second lens is to counteract the chromatic aberration of the first. Although the correction is never perfect, it can significantly improve the focusing, as illustrated in Figure 3.5. Such an achromatic doublet is used for the collecting optics of the present experimental setup.

3.1.2 Use of spectroscopy for plasma diagnostics

Having a method to split emissions into their wavelengths, it is possible to use the measured emission spectrum for plasma diagnostics. There are several ways of doing so. The radiative signature of a plasma indeed holds a lot of information about the plasma parameters, once each atomic transition can be related to an observed peak in the spectrum. The measurement of the intensity can allow to get the population of the emitting species with Equation 2.66, provided the spectrometer is calibrated for the measurement of absolute intensities. Otherwise, the comparison of emission lines can give information about the ratio of populations between species.

If the plasma is in thermal equilibrium (unique temperature), these ratios can be compared to the Boltzmann population ratio of Equation 2.40, therefore giving information about the plasma temperature. The width and shape of the emission lines also holds information, if the resolution of the spectrometer is fine enough for these measurements.

For plasmas far from thermal equilibrium, the spectral measurements can be compared to the results of a non-equilibrium CR model predicting the intensities of emission lines. This last method is the choice made in this work. Most equations relating level populations to temperature therefore do not hold.

Overall, OES provides a versatile and non-invasive tool for plasma diagnostics, which is why it is so widely used in the literature.

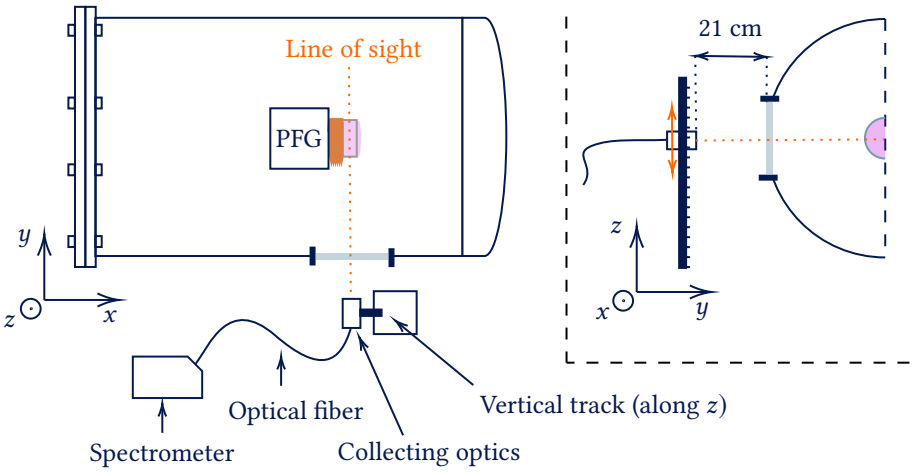

Figure 3.6: Schematic of the experimental setup (top and front views)

3.2 Experimental setup

The spectroscopic measurements are carried out with the setup schematized in Figure 3.6. Pictures of the actual setup are also given in the appendix, Section B.1. The collecting optics are placed on a vertical track, allowing one vertical degree of freedom. This makes it possible to take measurements at different heights. The goal of these measurements at different z positions is to obtain line intensity distributions $I_{ul}(z)$ for transition between levels u and l, which ultimately can be used to compute the radial intensity distribution $I_{ul}(r)$ of each line.

The collecting optics focus the incident light into the optical fiber. The latter has its other end connected to the spectrometer, delivering the collected photons through the slit. The spectrometer's sensor collects the spectrally split beam during the chosen integration time. The measured signal is then sent to a computer connected to the spectrometer. In the following, we will review the main characteristics of each component of the optical instrumentation. In addition to the optical setup, the functioning principle of the pressure gauges used for the pressure measurements is described.

Collecting optics

The collecting optics consist of an achromatic doublet with a tunable aperture. This aperture is open to the maximum for the measurements. This is necessary because of the low intensity emissions to be measured. The main properties of the lens and aperture are summarized in Table 3.1.

Optical fiber

The optical fiber connects the collecting optics to the slit of the spectrometer. Its characteristics are listed in Table 3.2.

Table 3.1 Characteristics of the collecting optics [41, 42]

Manufacturer	ThorLabs
Aperture model	SM1D12C
Lens model	AC 254-050-AB-ML
Spectral range [nm]	400 to 1000
Aperture diameter [mm]	1 to 12
Lens diameter [mm]	25.4
Focal length [mm]	50
Chromatic focal shift [mm]	-0.2 (@450 nm) to +0.3 (@1100 nm)

Table 3.2 Characteristics of the optical fiber [43]

Manufacturer	Ocean Insight
Model	QP200-2-VIS-BX
Spectral range [nm]	400 to 2100
Core size [µm]	200
Length [m]	2

Spectrometer

The spectrometer is the central element of the setup. It is a high sensitivity spectrometer, with a relatively large slit to avoid blocking a too large part of the signal, at the cost of a lower spectral resolution. In order to avoid losing any intensity to unused orders of diffraction, the spectrometer uses a blazed grating. Inside the spectrometer, only mirrors are used (no lens) to avoid any additional chromatic aberrations. It is a custom spectrometer ordered by the VKI, and provided by Ocean Insight [44]. Its characteristics are listed in Table 3.3.

Table 3.3 Characteristics of the spectrometer

Manufacturer	Ocean Insight
Model	Maya2000Pro
Serial number	MAYP113452
Grating	600 lines blazed at 1 µm
Spectral range [nm]	597 to 1034
Slit	INTSMA-050 slit (50 µm)
Sensor	Hamamatsu S11510 CCD [45]

The sensor is a 2-D pixel matrix (2068×70 pixels, 2048×64 effective), but the spectrometer reads it as a pixel array, by summing the measurements in the smallest dimension. The spectrometer was calibrated in wavelengths by the manufacturer, relating each pixel to a precise wavelength value. This relation is given by

$$\lambda = C_0 + \#p \cdot C_1 + \#p^2 \cdot C_2 + \#p^3 \cdot C_3 \tag{3.3}$$

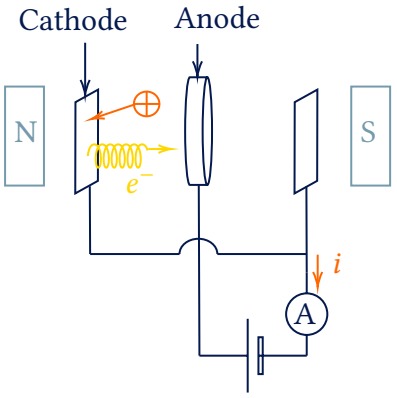

Figure 3.7: Cold cathode pressure gauge

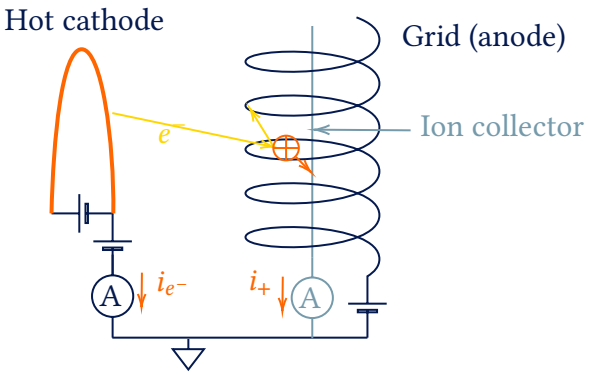

Figure 3.8: Hot cathode pressure gauge

where C_i [nm/pixel^i] is the calibration coefficient of order i, and $\#p$ is the pixel index (0 to 2067). The coefficients are given in a calibration sheet provided by the manufacturer. The regression fit is equal to $1 \pm 5 \times 10^{-11}$, showing an excellent agreement.

The integration time used for the measurements in DRAG-ON is

$$t^* = 500 \text{ ms}$$

This large integration time is necessary to increase the signal-to-noise ratio, since the emissions from the plasma are very weak.

Alignment of the optics

The alignment process is carried out with a laser connected to the collecting optics. With targets on the windows on both sides of the vacuum chamber, it was possible to align the optics for the line of sight to go through the transparent tube, while minimizing the vertical and horizontal tilt angles.

Pressure sensors

At low pressures such as those reached in DRAG-ON, conventional pressure sensors using membrane deflection are unusable. The facility is equipped with two types of pressure gauges that can work under such low pressures: *cold cathode pressure gauges* and *hot cathode pressure gauges*.

The functioning principle of cold cathode gauges is represented in Figure 3.7. The high voltage between the cathode and the anode forces arcs to form between them. This stream of electrons is caught in a magnetic field, such that their trajectories is helical, increasing the distance covered by the electrons before reaching the anode. Depending on the number density and nature of the gas in the system, the electrons will collide with more or less neutral atoms, which will be ionized by the collision with these very energetic electrons. These now positive particles are therefore attracted to the negatively charged cathode. This results in a current that, when measured, can be related to the number density, which can then be related to the pressure. This type of pressure gauge measures pressure in real time, which is why they are used for

pressure monitoring in DRAG-ON.

Hot cathode gauges also work by electron impact ionization, as illustrated in Figure 3.8. The difference with the previous type of sensor is the way the electrons are emitted. For hot cathode gauges, they are emitted thermally, by heating the cathode with a current. The flux of electrons can be controlled precisely with this technique. The emitted electrons are drawn toward the high voltage anode (grid). When they collide with neutral particles inside the grid, they can ionize them. These positive ions are then attracted towards the ion collector, which is at ground potential, thus largely negative when compared to the anode. This ion current can be related to the background number density, or pressure. The advantages of this type of pressure gauge is the proportional relation between the current and the pressure, and the control on the electron flux, which make them more accurate. They are can however not give an instantaneous reading, and are therefore only used when precise pressure measurements are needed.

3.3 Relative intensity calibration of the optical setup

3.3.1 Purpose of the intensity calibration

The assembly described in Section 3.2 does not have a flat response with wavelength. If light of uniform spectral intensity was to be emitted at the location of the transparent tube towards the collecting optics, the measured signal would not be perfectly flat: the setup is more sensible to some wavelength than others. This is due to various causes:

- The background Argon gas between the transparent tube and the window might absorb some wavelength lines,
- The chamber's window and transparent tube itself might not have a perfectly flat transmittance,
- The 21 cm of air between the window and the collecting optics has a spectral absorption coefficient that highly depends on the humidity level, since water vapor absorbs certain lines significantly in the infra-red,
- The lens has a transmittance that is not perfectly uniform for all wavelengths,
- The reduced but still existent chromatic aberrations imply that some wavelengths are better focused than others into the fiber optics,
- The path of light through the fiber optics leads to a certain amount of attenuation, which also depends on the wavelength,
- The pixels of the CCD detector in the spectrometer can have slightly different sensitivities, leading to a higher signal for the wavelengths related to the more sensitive pixels.

All these phenomena imply that the response of the spectrometer, defined as

$$H(\lambda) = \frac{I_\lambda^{\text{in}}(\lambda)}{I_\lambda^{\text{out}}(\lambda)} \tag{3.4}$$

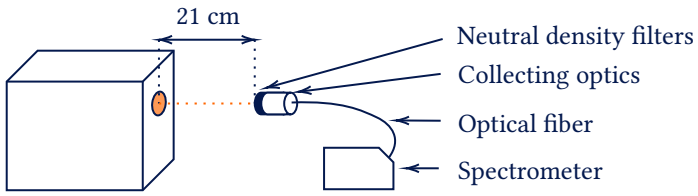

Figure 3.9: Placement of the optical instruments in front of the blackbody source

where I_λ^{in} is the incident spectral radiance and I_λ^{out} is the measured spectral radiance, depends on the wavelength, and therefore needs to be measured. This step is particularly necessary for this work, since the purpose of the spectral measurements is the comparison of emission line intensities. If they are on parts of the spectrum that have a significantly different response, the comparison would be meaningless without an intensity calibration.

3.3.2 Calibration method

The principle to make such a calibration is to measure the output of the setup to a known input light source, and to take the ratio between both signals. If the optical path for the calibration is exactly the same as for the test, this method allows to have absolute intensity measurements. For practical reasons however, an absolute calibration of the setup could not be carried out in the context of this work. It would have required to have a source of known spectral radiance inside the transparent tube, which could not be done in practice with the available blackbody source. For future developments however, such an absolute calibration could be performed with a Tungsten wire, which are frequently used as calibration sources because of their well known emission spectrum [46].

Instead, the collecting optics, fiber and spectrometer were moved to a calibration laboratory, where they could be placed in front of a blackbody source as shown in Figure 3.9 (a picture of the actual setup is shown in the appendix, Section B.2). The comparison of the known spectral radiance of the blackbody source to the measured radiance allow to measure the spectral response of the setup. The source's main characteristics are summarized in Table 3.4.

Table 3.4 Blackbody source characteristics [47]

Manufacturer	AMETEK Land
Model	R1500T
Temperature range [°C]	500 to 1500
Emissivity [-]	0.99
Uncertainty [K]	±3

Assumptions

Since the calibration setup does not include the transparent tube and the window of the chamber, the calibration is carried out with the assumption that these components have a spectrally flat response. In the visible and near infrared ranges, this is true for glass [48], and was verified in the literature for the material of the transparent tube. It is also assumed that the absorption by the Argon gas in the chamber is negligible in such a high vacuum.

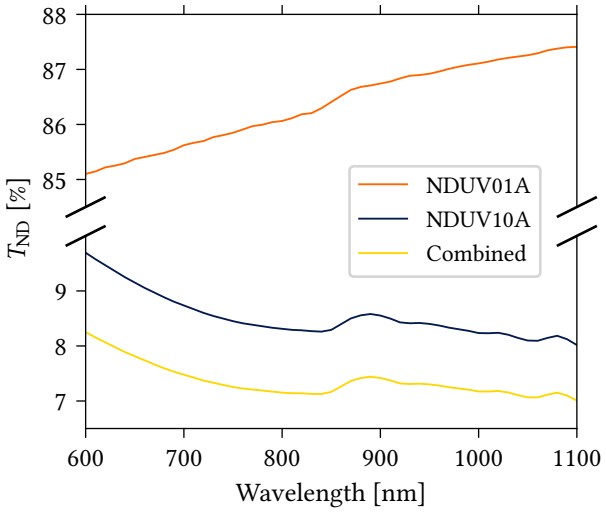

Figure 3.10: Response of the neutral densities [49]

Practical considerations

At the blackbody temperatures needed for significant emissions on the entire spectrometer range (600-1000 nm), the blackbody source emits much higher intensity light than the plasma in the DRAG-ON facility. The high sensitivity spectrometer therefore had to be protected from saturation by reducing the integration time to 10 ms, and adding neutral density filters (ND) in front of the collecting optics. The change in integration time only changes the measured signal by a proportionality constant (this is a property of the CCD sensors), therefore having no effect on the relative calibration.

The ND, on the other hand, have a contribution to the measured assembly response, which must be subtracted after the measurements. The response of these filters can in theory be measured by comparing the response with and without the ND, but this was in practice not possible with this setup. Indeed, for the spectrometer not to saturate without the ND, the blackbody source could not be at a temperature higher than 800°C. At this temperature, there are only negligible emissions at the smaller wavelengths. Taking the ratio of the response with and without filter therefore corresponds to dividing white noise by white noise, giving no valid response for nearly half the wavelength range. It was thus decided to use the filter response provided by the manufacturer. The transmittance for the two combined neutral density filters is represented in Figure 3.10, for both filters NDUV01A and NDUV10A [49].

The effect of the absorption of water vapor due to the optical path through air must also be taken into account for the final calibration curve. The spectral transmittance of humid air was computed in the spectral range of interest with the cross sectional data of the *HIgh-resolution TRANsmission molecular absorption* (HITRAN) database [50]. The details of this calculation are given in Appendix C. The developed code allows to compute the transmittance through air at a given pressure, temperature and relative humidity, for a given spectral range. There is water vapor absorption both in the calibration setup, and in the experimental setup in DRAG-ON. If the conditions differ significantly (different length, temperature, pressure or relative humidity), the water vapor absorption might have been stronger in one laboratory than the

other, meaning that the ratio of the spectral transmittance between the two cases needs to be used for the computation of the final calibration curve.

To take into account the effect of the ND filters, and the possible different atmospheric conditions for water vapor absorption, Equation 3.4 becomes

$$H(\lambda) = \frac{I_\lambda^{\text{in}}(\lambda) \cdot T_{\lambda,\text{ND}}(\lambda)}{I_\lambda^{\text{out}}(\lambda)} \cdot \frac{T_{\lambda,\text{H}_2\text{O}}(\text{calibration conditions}, \lambda)}{T_{\lambda,\text{H}_2\text{O}}(\text{DRAG-ON conditions}, \lambda)} \tag{3.5}$$

with $T_{\lambda,\text{ND}}$ [-] the spectral transmittance of the ND filters, and $T_{\lambda,\text{H}_2\text{O}}$ [-] the spectral transmittance of water vapor in air, for the given conditions of pressure, temperature, relative humidity and length of the optical path. In the case of the measurements used in this work, the optical path length through air was chosen to be the same in both setups, and the atmospheric conditions were equivalent, such that the water vapor absorption is the same in both cases, therefore not influencing the setup response. The developments of Appendix C were made in previsions of possible future modifications of the setup in DRAG-ON, possibly changing the optical path length between the window and the collecting optics. The developed tool for the computation of $T_{\lambda,\text{H}_2\text{O}}$ for given conditions make it possible to re-use the calibration curve obtained in this work, even for different conditions.

3.3.3 Results of the intensity calibration

The response of the system was measured for three different temperatures to verify repeatability of the measurement. After removing the background radiation to the measured spectra[1], we obtain the curves of Figure 3.11. In this figure, the measurements are compared to the known incident emissions, calculated with Planck's law for blackbody radiation (Equation 2.44), and scaled to an arbitrary constant for better visualization (no impact on the results for relative intensity calibration).

The ratio of the known incident spectrum (blackbody multiplied by the ND filter transmittance), to the measured spectrum, is given in Figure 3.12. It shows that the measurement of the response $H(\lambda)$ is indeed repeatable. It can be noted that there is however variability in the results at the smaller wavelengths. This is explained by the lower emissions of the blackbody source at these wavelengths. As we increase the source's temperature, the signal overcomes the noise, leading to a cleaner measurement of the setup response.

Finally, the curve used for the scaling of the spectrometer measurements in the following of this work is given in Figure 3.13. It corresponds to the measurement made at 1200°C, smoothed with a Savgol filter [51]. The relative error between the experimental and smoothed system response is shown in Figure 3.14. The standard deviation of the error does not exceed 5%, and is of the order of 1% for most of the spectral range of the spectrometer. The error is defined as

$$\epsilon_H = \frac{H^{\text{exp}} - H^{\text{smooth}}}{H^{\text{smooth}}} \tag{3.6}$$

[1] This is done for each measurement. The background is measured in advance when the source is off, and subtracted to each measurement.

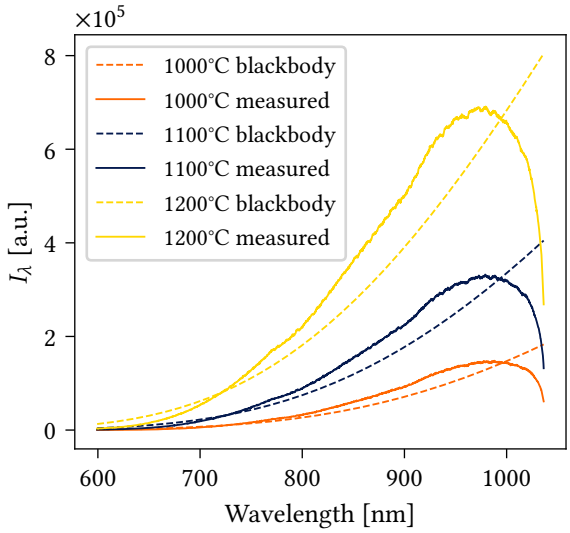

Figure 3.11: Blackbody and measured spectral radiances at 1000, 1100 and 1200°C

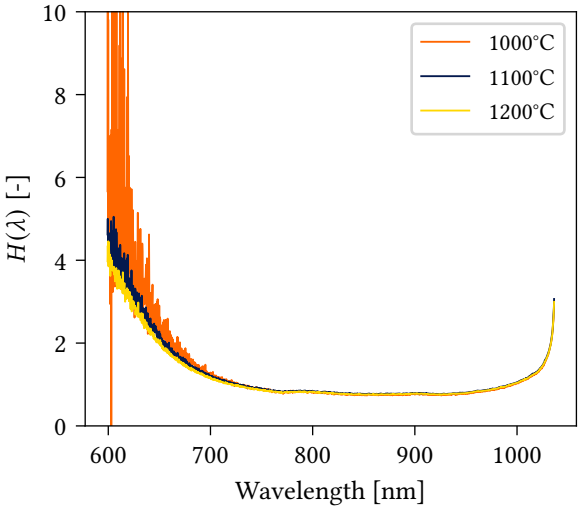

Figure 3.12: Measured optical installation response at 1000, 1100 and 1200°C

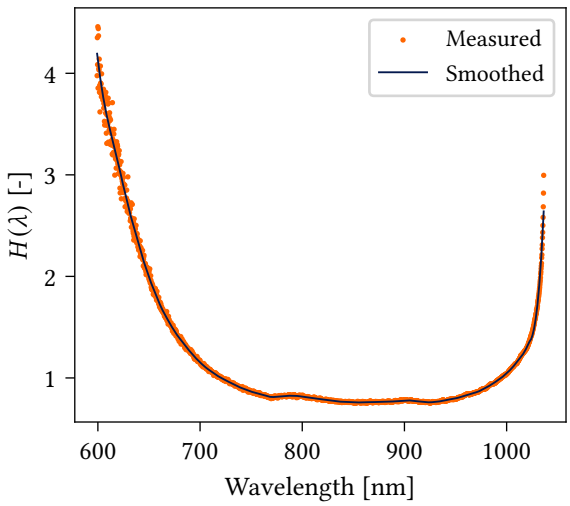

Figure 3.13: Smoothed response of the optical setup

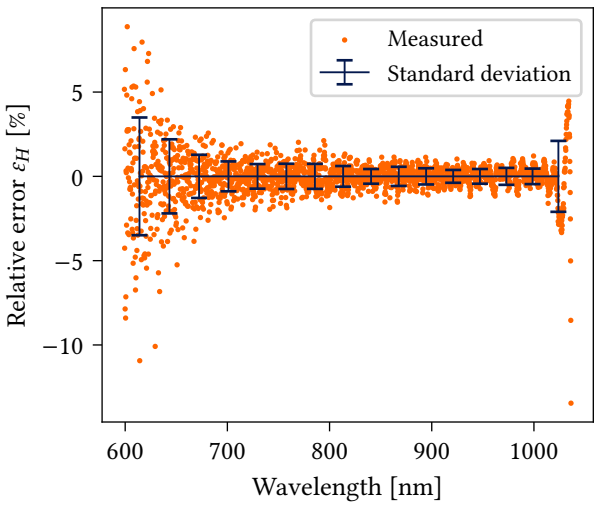

Figure 3.14: Error on the response of the optical setup

3.4 Test campaign and results

With the experimental setup in place, the optics properly aligned, and the optical installation calibrated in wavelengths and in intensity, the measurements can be carried out and processed. In this section, the experimental procedure is detailed. The steps to process the raw measurements are then enumerated, from the direct output of the spectrometer to the radial distribution of intensity $I_{ul}(r)$ for each spectral line. The results are then discussed.

3.4.1 Procedure

The following procedure was followed:

1. Alignment of the collecting optics.
2. Spectrometer integration time set to to 500 ms.
3. Measurement of the background emissions.
4. Ignition of the PFG. If the chamber was vented before the test, an outgassing of 45 minutes must be performed. It consists of letting the PFG run at high flow rate, which ensures that any contamination in the PFG are evacuated before making any measurement. After the outgassing, if any, the PFG must be tuned to the parameters chosen for the test. In this case:
   - Acceleration voltage of 25 V
   - Focusing coil current of 0.5 A
   - RF power of 60 W
   - Argon volume flow rate of 3 sccm (standard cubic centimeters per minute). It corresponds to a particle flow rate of 2.2×10^{-6} mol/s.

   Pictures of the PFG running in these conditions are given in Section B.3.
5. Measurement of the emission spectrum.
6. Repeat step (5) for other positions of the collecting optics on the vertical track. For this experiment, the vertical resolution was chosen to be 10 mm[2]. At some z positions, measurements were made twice to check repeatability.
7. Shutdown of the PFG.

3.4.2 Line intensity calculation

Once the data is collected, it needs to be treated in order to obtain the desired intensity measurements. In this section, these necessary data processing steps are detailed.

[2]This is rather coarse, and was intended to be refined, but unplanned maintenance of the PFG did not allow for further testing

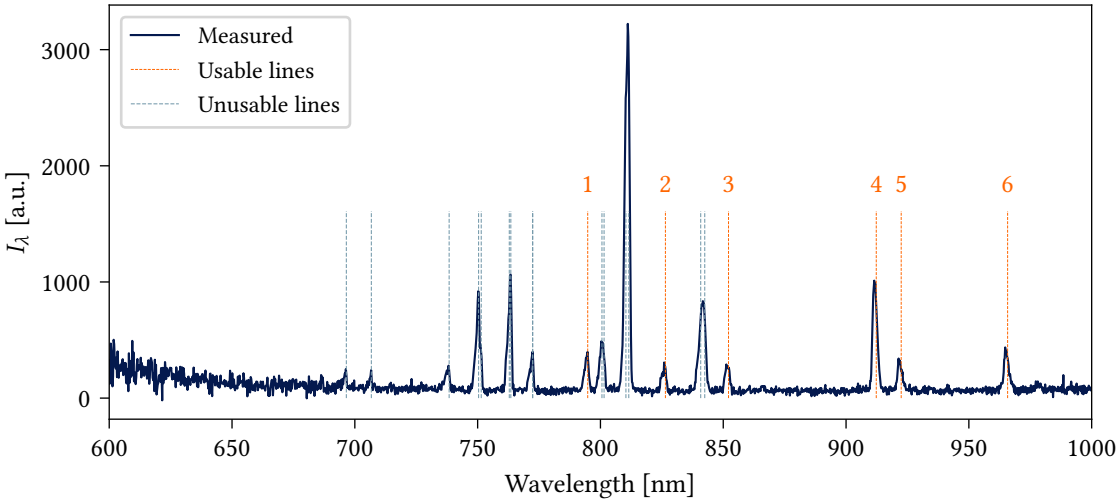

Figure 3.15: Line identification by comparison to Argon atomic transitions.

Line identification

The first step consists of identifying the spontaneous decay reactions that are related to each emission line observed in the measured spectrum. In order to do that, each pixel must first be related to a wavelength using Equation 3.3. After removing the unusable pixels at the extremities of the CCD sensor, subtracting the background, and multiplying the spectrum by the intensity calibration curve measured in Section 3.3, we obtain a spectrum that can be used for line identification.

The identification is carried out by comparing the observed emission lines to the wavelengths of allowed optical transitions of Argon. Most of these transitions are listed in Table A.2, but for completeness, lines that are not used in the model because of a too high uncertainty on the Einstein coefficients were also added, as well as emission lines of Ar^+ which could also play a role in the observed emissions. This comparison is shown in Figure 3.15, where the reactions that did not fall in any observed peak were removed for clarity. The shown spectrum corresponds to the measurement at the z position corresponding to the centerline of the PFG. This figure allows the identification of the transitions for which the intensity can be compared to the CR model (usable lines). They are listed in Table 3.5, where the index matches the indices of Figure 3.15. We define the set $\mathcal{L}$ of lines, as all the lines that will be used for the comparison to the CR model.

There are also unusable lines, including the clearest one around 811 nm, which can not be used for comparison to the CR model. This is because these lines could correspond to two different transitions. In the case of the highest peak, it is not possible to know if we see transition $\mathrm{Ar}(8) \rightarrow \mathrm{Ar}(2) + h\nu$ at 810.4 nm, or the transition $\mathrm{Ar}(6) \rightarrow \mathrm{Ar}(1) + h\nu$ at 811.1 nm, or a combination or both. This is due to the poor spectral resolution of the spectrometer, which is not fine enough to resolve the two peaks. The two emission lines merge, making it impossible to compare with the results of the CR model, which predicts the intensity of transitions independently. This holds for all other unusable lines of Figure 3.15. The lines at 706.7 nm and 738.4 nm are special case, as they overlap with strong emission lines of Ar^+ and

Table 3.5 Identified set usable lines $\mathcal{L}$ for the comparison to the CR model

#	**Wavelength** [nm]	**Upper level**		**Lower level**
1	794.8176	11	→	3
2	826.4521	13	→	4
3	852.1441	11	→	4
4	912.2967	5	→	1
5	922.4498	9	→	4
6	965.7786	5	→	2

not lines of neutral Argon. Because of the presence of Argon ion in the chamber, these lines are therefore unusable as well. The line at 696.5 nm is also ignored because of the too low signal-to-noise ratio, greatly increasing the uncertainty in the computation of its intensity (20 to 100% depending on the height at which the measurement is made).

Spectral integration

In order to obtain a single value for the intensity of a transition, the measured lines must be integrated spectrally. In this work, it was decided to fit each line to a Gaussian curve and to integrate the area under that curve, as it is frequently done in the literature [29, 26]. This method avoids the integration of the surrounding noise, which for small emission lines can be significant compared to the actual intensity of the peak. A Gaussian curve is chosen for the fitting because the main broadening mechanism is instrumental broadening. The spectral resolution is not fine enough to resolve the physical broadening mechanisms discussed in Section 2.4. Indeed, the observed spectral resolution is a HWHM of about 1 nm, which is 3 orders of magnitude larger than the contribution of Doppler broadening to the HWHM.

Each emission line is thus fitted to an analytical expression of the shape

$$I_{\lambda,ul} = G_{ul} \exp\left\{-\frac{(\lambda - \lambda'_{ul})^2}{2s_{ul}^2}\right\} \tag{3.7}$$

where G_{ul}, λ'_{ul} and s_{ul} the parameters of the fit (λ'_{ul} being naturally always nearly equal to the expected wavelength for this transition). The fit is carried out with the least squares method, on the data points locally shifted in intensity to remove their local baseline (the average of the noise around the emission line is thus equal to zero). This must be done for each usable emission line, for each height at which a spectrum was measured. The Gaussian fittings for the centerline measurements are represented in Figure 3.16 for two typical lines.

The intensity is finally obtained by integrating these lineshapes spectrally. This gives

$$I_{ul} = G_{ul} s_{ul} \sqrt{2\pi} \tag{3.8}$$

Uncertainty evaluation

There are two quantifiable uncertainty sources in the experimental intensity measurement procedure. The first comes from the intensity calibration of the setup. We only know the

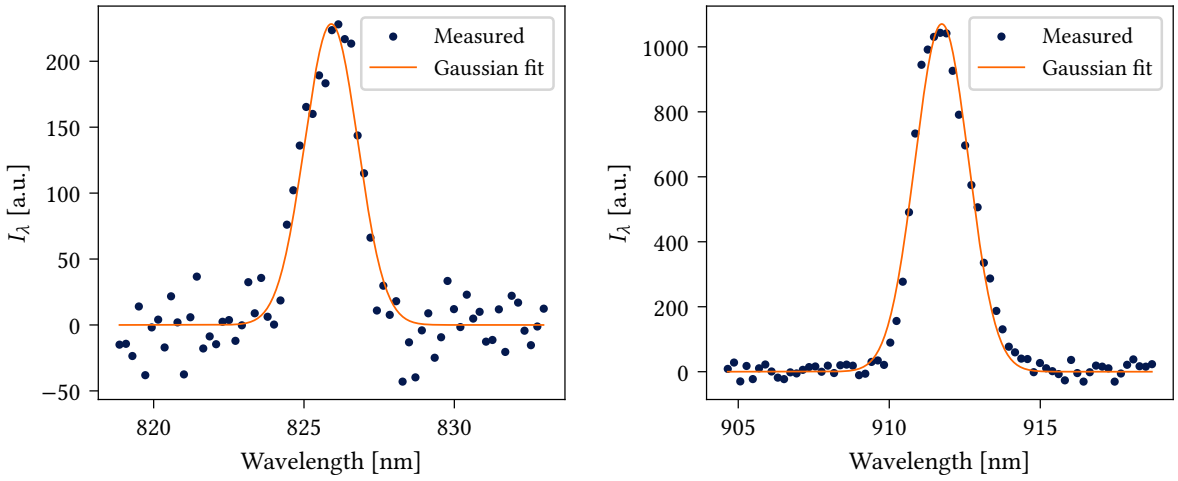

(a) Line #2 (826 nm)

(b) Line #4 (912 nm)

Figure 3.16: Gaussian fitting for two typical emission lines, for the centerline measurement

relative response of the setup with a certain amount of precision, as it was shown in Figure 3.14. At each wavelength, the calibration introduces a certain amount of uncertainty quantified by $\varepsilon_H(\lambda)$. The second source of uncertainty comes from the Gaussian fitting and spectral integration. The least square fitting method gives estimates of the uncertainty on each fitting parameter, by means of the covariance matrix returned by the `curve_fit` method from the `scipy` Python package [52]. The uncertainty on the integrated intensity δI_{ul} due to the fit can therefore be computed with

$$\delta I_{ul}^{\text{fit}} = \sqrt{\left(\frac{\partial I_{ul}}{\partial G_{ul}}\delta G_{ul}\right)^2 + \left(\frac{\partial I_{ul}}{\partial s_{ul}}\delta s_{ul}\right)^2} = \sqrt{\left(s_{ul}\,\sqrt{2\pi}\,\delta G_{ul}\right)^2 + \left(G_{ul}\,\sqrt{2\pi}\,\delta s_{ul}\right)^2} \tag{3.9}$$

where δG_{ul} and δs_{ul} are the uncertainties on the fitting parameters. The total relative uncertainty is therefore given by

$$\frac{\delta I_{ul}}{I_{ul}} = \varepsilon_H(\lambda_{ul}) + \frac{\delta I_{ul}^{\text{fit}}}{I_{ul}} \tag{3.10}$$

where $\varepsilon_H(\lambda_{ul})$ is the 95% interval of the uncertainty on the setup response, evaluated locally around λ_{ul}.

3.4.3 Spatial intensity distribution

With the method described in this section, we can therefore obtain a value for the intensity for each line, at each z position, as well as a measure of the uncertainty on the intensity calculation. The resulting intensity distribution in function of the height at which the measurement is made can thus be plotted for each usable emission line. Figure 3.17 displays this distribution for two typical transitions, along the adimensional height $\hat{z} = 2z/D_{\text{t}}$ [-]. All lines follow a similar distribution.

Figure 3.17 most importantly shows that the repeatability of the experiment is not verified. Measurements made at the same height give significantly different results (larger than the

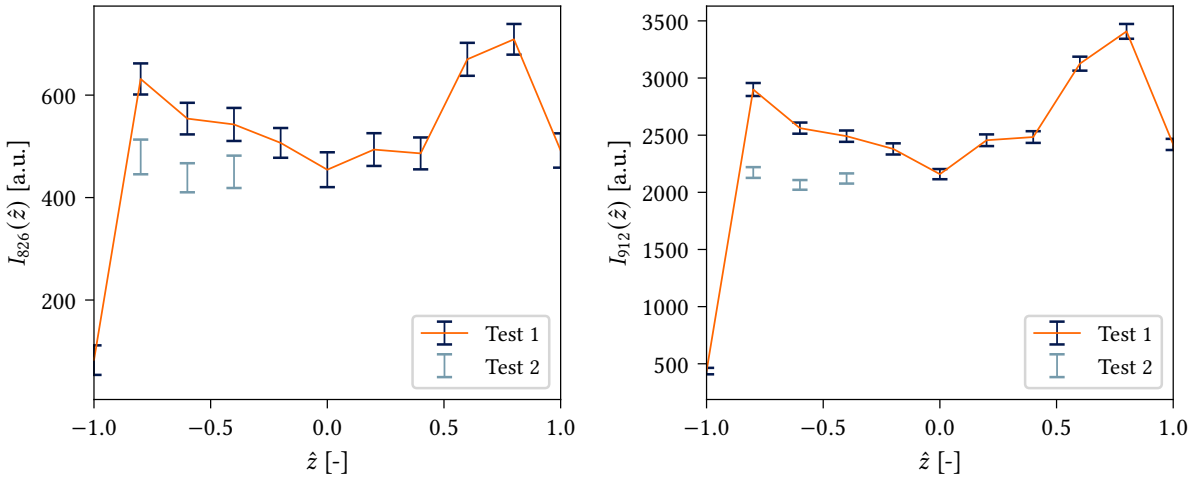

(a) Line #2 (826 nm) **(b)** Line #4 (912 nm)

Figure 3.17: Typical intensity distributions in function of the collecting optics position

uncertainty on the intensity calculation), limiting the validity of the measured intensity distributions. This can be explained by the manual translation of the lens on the vertical track. Even though the vertical track is supposed to preserve the alignment, the repeated releasing and tightening of the screw might have tampered with the alignment nontheless, therefore giving unrepeatable measurements. In order to prevent that from happening in future experiments, the setup must be modified to use electric translation motors instead of the manual translation method used here.

Radial intensity distribution

The results obtained in the timeframe of this work can not be used to extract a radial distribution of line intensities. However, the transformation from vertical distribution to radial distribution is a necessary step for the data processing method to be complete for future OES experiments. The method is therefore discussed briefly here.

At each height at which the measurements are made, we measure the integrated intensity on the line of sight. Comparing these measurements to the CR model results would require assuming that on a line of sight, the conditions are uniform. It is therefore equivalent to saying that $I_{ij}(y, z)$ is a function of z only (with y and z the horizontal and vertical coordinates in a vertical slice of the transparent tube). With the cylindrical geometry of the transparent tube, it seems more reasonable to assume an axisymmetric distribution of the intensities, which integrated horizontally leads to the variation of intensity in function of z observed in the measurements, as illustrated in Figure 3.18.

The Abel inverse transform [53] is a mathematical tool that can compute a radial distribution based on an integrated distribution such as the one we have for the intensities. It is formulated as

$$I_{ij}(r, x) = -\frac{1}{\pi} \int_r^\infty \frac{dI_{ij}(z, x)}{dz} \frac{1}{\sqrt{z^2 - r^2}} dz \tag{3.11}$$

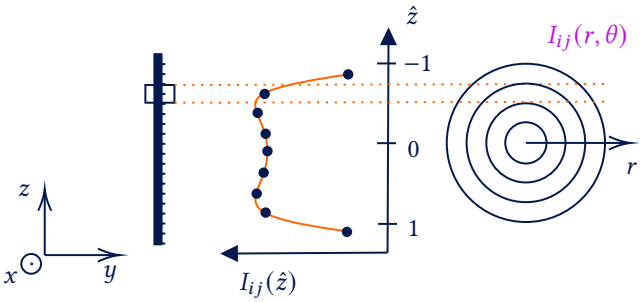

Figure 3.18: Horizontal integration of axisymmetric emissions

The method developed in this work is meant to focus on one slice only along the x axis, such that there is no dependency of the intensity on this variable in the measurements we want to transform. In order to evaluate this integral, $I_{ij}(z)$ must be symmetric with respect to the centerline (since we assume axisymmetry). In general, measurements will always include noise that break the symmetry. In addition, the OES measurements are carried out with a coarse resolution along z. Evaluating Equation 3.11 numerically can be challenging, as this integral has been shown to be very sensitive to noise. It can therefore be interesting to fit the data points to a smooth curve before applying the transform. The integral of Equation 3.11 can then be evaluated either numerically or analytically. The present intensity distributions seem to follow a M pattern, although this pattern has to be confirmed by more reliable measurements. If this pattern is verified, a fitting shape function could be

$$I_{ij}(\hat{z}) = \begin{cases} A_0 + A_2\hat{z}^2 + A_4\hat{z}^4 & \text{if } -1 < \hat{z} < 1 \\ 0 & \text{otherwise} \end{cases} \tag{3.12}$$

where the constants A_i are the parameters of the fit. This allows to have a symmetric input to the Abel transform, but also an analytical expression that can be used to solve Equation 3.11 analytically. For later measurements, if the fitting curve does not provide an analytical solution, the `PyAbel` library can be used for numerical integration. This library contains a variety of numerical methods, each specialized for a specific type of input distribution [53].

In the cases where Equation 3.12 can be used to approximate the distribution, the radial distribution is given analytically by

$$I_{ij}(\hat{r}) = -\frac{2}{3\pi}\sqrt{1-\hat{r}^2}\left[3A_2 + 2A_4\left(2\hat{r}^2+1\right)\right] \tag{3.13}$$

where $\hat{r} = 2r/D_t$ [-] is the non dimensional radial position. Applied to the curve of Figure 3.19, this gives the radial distribution displayed in Figure 3.20. These figures are for illustration purposes, since the experimental data could not be used for the testing of the Abel inversion because of their unreliability.

3.5 Conclusion

In this chapter, we have investigated the experimental considerations to perform OES in the DRAG-ON facility. After reviewing the basics of spectroscopy, we have described the facility, setup and instruments used for the measurement of plasma emissions. The relative intensity

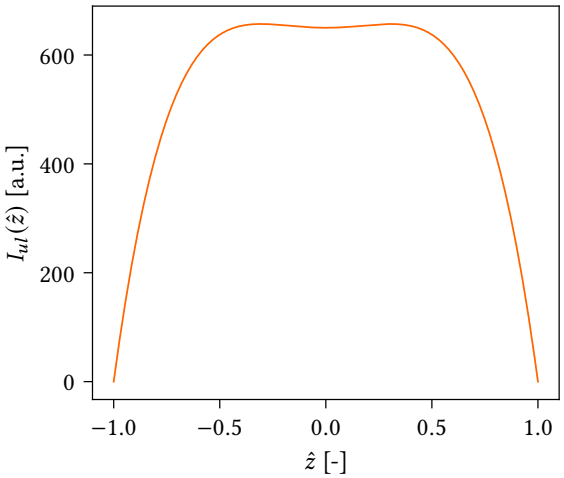

Figure 3.19: Example line intensity distribution along z

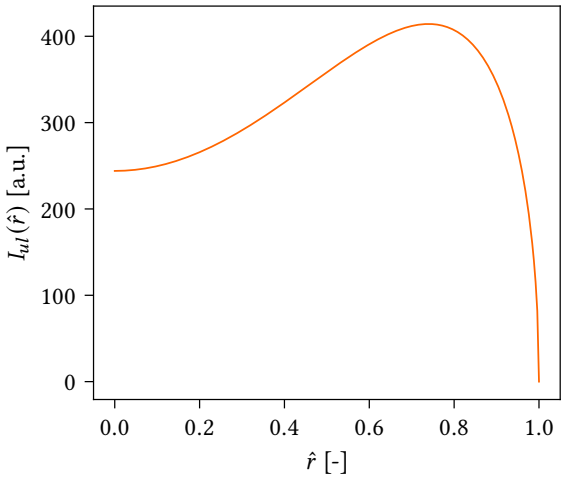

Figure 3.20: Radial distribution, by Abel transformation

calibration of the optical installation was then detailed, and the calibration results discussed, showing consistency in the response of the setup for different calibration temperatures. The procedure to extract line intensities from emission spectra was then detailed, showing how we avoid integrating the noise, and how we estimate the error on the spectral integration for intensity calculation.

Once these intensities were obtained however, the experimental results have shown irregularities. Most importantly, repeatability was shown not to be respected with the current experimental setup and procedure. The most probable explanation is the manual translation of the collecting optics along the vertical track, which might have caused a misalignment of the optics for several measurement points. In order to remove this source of error from future experiments, a motorized translation should therefore be used. The alignment must be done carefully, since the present intensity measurements have shown great sensibility.

Finally, the method provided at the end of this chapter to transform a line-of-sight integrated, vertical distribution to a radial intensity remains valid, but it must be noted that if the trend of the distribution is different, another fitting function must be used.

Overall, this chapter provides the framework for performing OES measurements in the DRAGON facility, and the observation made will allow to enhance the experimental setup to provide more reliable measurements in the future. A motorized rail with vertical and horizontal degrees of freedom was ordered to enhance the setup, and it was placed in the facility (pictures in the appendix, Section B.4). Unfortunately, it could not provide measurements in the timeframe of this work because of unforeseen maintenance of the PFG.

The next chapter consists of comparing the numerical results of the CR model of Chapter 2 to the experimental lines, to find which plasma parameters fit best the experimental line intensities. The complete method would consist in performing this comparison for each radial position. However, the low reliability of the measurements obtained in this chapter does not

allow to use the radial distribution of line intensities. Chapter 4 will therefore rely on the OES measurements made at one vertical position only, which is sufficient for the development of the tools for the comparison. An natural evolution of this work is therefore to scale this analysis to a radial distribution of spectra.

CHAPTER 4

Extraction of Plasma Parameters from Line Intensity Comparison

The two previous chapters provide the foundation for the methodology. In Chapter 2, a comprehensive CR model for Argon was developed, capable of predicting emission line intensities based on two key plasma parameters: the electron temperature and electron density. On the other hand, Chapter 3 provided experimental measurements of the emission line intensities of Argon observed in the DRAG-ON facility.

In this chapter, we focus on the comparison of these two sets of line intensities. We define a criterion based on the standard deviation, to assess the agreement between the experimental and predicted intensities. This criterion serves as an objective function, quantifying the disparity of the results of both methods. By evaluating this objective function with different values of electron temperatures and densities, we aim to identify the parameter values that minimize the disparity. These obtained values for electron density and temperature therefore correspond to the inputs of the CR model that yield the best agreement with the experimental lines, according to the defined criterion.

In addition, the uncertainty on the obtained parameter values is computed by Monte Carlo sampling. By sampling the different sources of uncertainty in the model and experimental results within their bounds, we simulate a range of possible electron density and temperature values, therefore giving the region of uncertainty of the estimates. A discussion is then carried out to evaluate the suitability of these results as estimates of the actual conditions inside the facility.

As previously discussed in Chapter 3, concerns have been raised about the reliability of the spatial distribution of intensities at this stage of the experimental work. We will therefore focus our analysis on a single spectrum measurement. This enables to investigate the feasibility and reliability of the methodology, setting the foundation for future scaling to spatially distributed intensities. The intensity measurements we compare the CR model results to in this chapter are listed in Table 4.1.

4.1 Comparison criterion

Various criteria are used in the literature for the comparison of the measured and predicted line intensities. In this section, the different possibilities are discussed and the choice of a standard deviation estimator is justified.

Table 4.1 Experimental intensities used for comparison to the CR model

i	**Wavelength** [nm]	**Upper level**		**Lower level**	$I_{i,\mathrm{exp}}$ [a.u.]	**Relative error** [%]
1	794.8	11	$\rightarrow$	3	986.0	4.9
2	826.5	13	$\rightarrow$	4	709.0	4.8
3	852.1	11	$\rightarrow$	4	770.9	4.6
4	912.3	5	$\rightarrow$	1	3408.1	2.3
5	922.4	9	$\rightarrow$	4	939.4	3.8
6	965.8	5	$\rightarrow$	2	1215.5	4.1

The experimental intensity measurements provide information about the relative intensities of the usable lines. They can therefore not be directly compared to the CR model results. A usual method to make the comparison with this constraint is to compare experimental and CR model line ratios, and find the plasma parameters that allow for the CR model to have the selected line ratios equal to the experimental ratios [26, 27]. The number of parameters that can be estimated from this method depends on the number of line ratios used in the analysis. For example, Iordanova and Koleva [26] determine n_e and T_e by selecting two line ratios. One is n_e sensitive (lines at 696.5 and 750.4 nm), and the other is T_e sensitive (lines at 801.5 and 794.8 nm). Their CR model is used to simulate what these two line ratios would be equal to for a range of electron temperatures and densities. By finding the conditions at which both line ratios are equal to the experimental line ratios, they find the conditions of the measured plasma. Although this method allows to have estimates of the plasma parameters in a straightforward way, it requires the use of lines that can not be used in this work because of the low resolution of the spectrometer, reducing the number of usable lines.

Instead, the criterion used by Malyshev and Donnelly [25] is employed in this work. It consists of computing the standard deviation of the ratios of predicted to experimental lines, normalized by the average:

$$\xi(T_\mathrm{e}, n_\mathrm{e}) = \frac{\mathrm{STD}\left(\mathrm{I_{CR}/I_{exp}}\right)}{\left\langle I_{\mathrm{CR}}/I_{\mathrm{exp}} \right\rangle} = \frac{\sqrt{\dfrac{1}{N}\displaystyle\sum_{i\in\mathcal{L}}\left(\frac{I_{i,\mathrm{CR}}}{I_{i,\mathrm{exp}}} - \left\langle \frac{I_{\mathrm{CR}}}{I_{\mathrm{exp}}} \right\rangle\right)^2}}{\left\langle I_{\mathrm{CR}}/I_{\mathrm{exp}} \right\rangle} \tag{4.1}$$

where N is the number of comparable lines in $\mathcal{L}$ (6 lines of Table 4.1), STD stands for standard deviation on set $\mathcal{L}$, and $\left\langle I_{\mathrm{CR}}/I_{\mathrm{exp}} \right\rangle$ is the average of the ratios on the same set of lines. This ξ objective function is a function of the electron density and electron temperature, since each $I_{i,\mathrm{CR}}$ depends on these two parameters.

One can see that this objective function ξ [-] is a measure of the disparity of the CR intensities to the experimental intensities. Indeed, if the model was perfect and if we gave it the exact conditions in the plasma, a ratio between a CR model line intensity to an experimental intensity would give the ratio between the units of both intensities, since the intensity calibration was relative, thus giving measurements in arbitrary units. In this perfect situation, each line ratio would be equal to this units ratio, since all computed line simply represents

the experimental lines in other units. The average $\langle I_{\mathrm{CR}}/I_{\mathrm{exp}} \rangle$ would therefore be equal to that unit ratio, and the standard deviation would be zero. If we are in a case where the conditions in the CR model are not equal to those in the plasma, some predicted lines will grow in intensity while other would shrink, inducing a standard deviation with respect to the average. The minimum ξ is therefore found at the conditions at which the standard deviation is the lowest, therefore where the CR model predictions best match the experimental intensities, in their relative units. The standard deviation is normalized by the average line ratio, for the objective function to be dimensionless and represent a percentage of deviation with respect to the mean.

This definition of the objective function was tested alongside the definition used by Bariselli et al. [29], used for the characterization of an Air-Xenon plume. This other definition consists in normalizing all experimental line intensities by the total intensity (such that the sum is equal to 1), and do the same for the CR model predicted intensities. The relative root mean square error of the CR model predictions to the experimental normalized intensities is then used as definition of the objective function

$$\xi'(T_{\mathrm{e}}, n_{\mathrm{e}}) = \sqrt{\frac{1}{N} \sum_{i \in \mathcal{L}} \frac{(\hat{I}_{i,\mathrm{exp}} - \hat{I}_{i,\mathrm{CR}})^2}{\hat{I}_{i,\mathrm{exp}}^2}} \tag{4.2}$$

with the normalized intensities $\hat{I}$ [-]

$$\sum_{i \in \mathcal{L}} \hat{I}_{i,\mathrm{exp}} = \sum_{i \in \mathcal{L}} \hat{I}_{i,\mathrm{CR}} = 1 \tag{4.3}$$

This criterion gives the same results as those obtained with Equation 4.1, with just a slightly higher uncertainty, confirming the consistency of the method chosen for this work. To avoid redundancy, only the results obtained with Equation 4.1 are presented in the following of this chapter.

The main advantage of the two last definitions of the objective functions is the fact that they allow the usage of multiple emission lines, whereas line ratio techniques lose part of the information contained in the experimental lines by choosing a single, or two line ratios at most. Using all the available experimental data allows to better comprehend the extent to which the CR model intensities actually match the experimental intensities, by giving a relative standard deviation. The line ratio technique on the other hand finds a crossing point, giving no information on the disparity of the CR model results to the experimental results.

4.2 Minimization of the objective function

With the objective function clearly defined in Equation 4.1, we can now evaluate it for an array of electron temperatures and densities, to find the conditions that actually minimize the chosen measure of disparity. As no prior knowledge is known about the conditions of the plasma, a large number of conditions were tested, ranging from densities of $n_{\mathrm{e}} = 10^{15}$ to 5×10^{18} m^{-3}, and temperatures from 2 to 80 eV.

At each tested point in the $(T_{\mathrm{e}}, n_{\mathrm{e}})$ space, the CR model is run to obtain the synthetic line intensities at these conditions. The synthetic intensities of the transitions included in the set

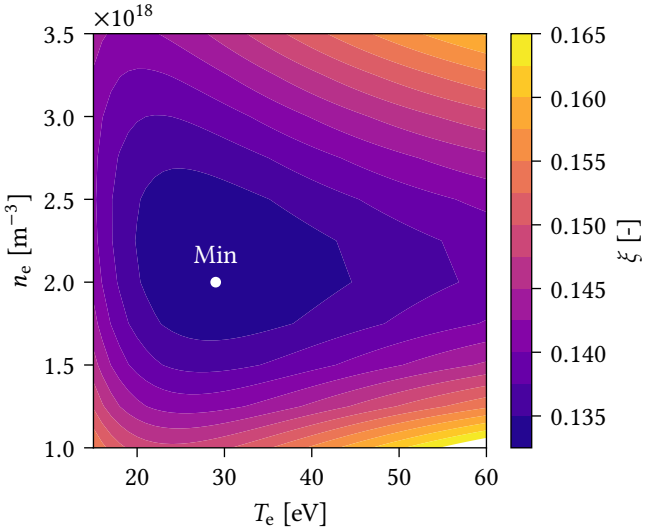

Figure 4.1: Contour plot for the error estimator in the the (T_e, n_e) space

$\mathcal{L}$ of usable experimental lines are then compared to the OES measurements with the defined criterion.

Only one minimum was found in this region of the (T_e, n_e) space, and $\xi(T_e, n_e)$ only grew when moving away from this minimum, in any direction. A zoom on this minimum is shown in Figure 4.1. This contour plot was obtained with a grid of $\Delta n_e = 0.25 \times 10^{18}$ m^{-3}, and $\Delta T_e = 1$ eV. With this resolution, we find a minimum located at

$$T_e^* = 29 \text{ eV} \quad , \quad n_e^* = 2 \times 10^{18} \text{ m}^{-3} \tag{4.4}$$

At this position, we have

$$\xi(T_e^*, n_e^*) = 0.1326 \tag{4.5}$$

For better visualization, the experimental and synthetic line intensities are shown in Figure 4.2 at this optimal point, with intensities normalized as in Equation 4.3.

4.3 Uncertainty analysis with Monte Carlo sampling

In this section, we evaluate the uncertainty on the results for T_e^* and n_e^*. This is done using the Monte Carlo sampling method. It consists of evaluating the uncertainty on T_e^* and n_e^* by brute force, by sampling each known source of uncertainty within their uncertainty bounds, and obtaining a distribution of the optimal plasma parameters. This method allows to assess the variance in the location of the minimum of the objective function, based on several known uncertainty sources, without linearizing the relation between the sources and the results.

We first identify the quantifiable sources of uncertainty:

- For the experimental intensities, we know that their uncertainty is given by the added relative contributions of the intensity calibration, and of the Gaussian fitting and integration. The uncertainty on $I_{i,\text{exp}}$ is finally given by Equation 3.10, and their values for the experimental lines used in this chapter are given in Table 4.1.

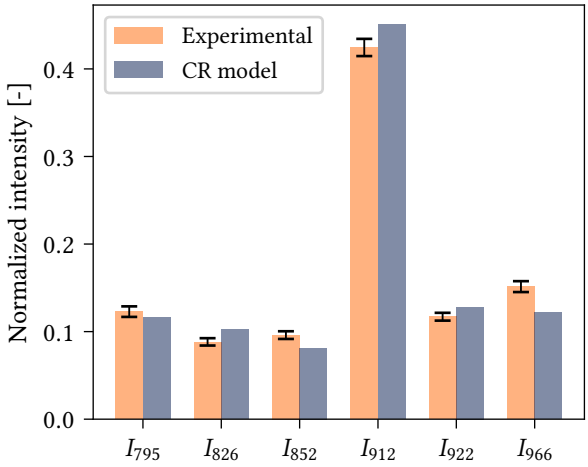

Figure 4.2: Comparison of the experimental line intensities to the numerical line intensities at the optimal plasma parameters

- The uncertainties on the intensities obtained with the CR model are difficult to evaluate, since they are the result of the steady state solution of a system of differential equations. Instead, we know the uncertainties on coefficients in this system.
  We have known uncertainties on the Einstein coefficients included in the model. For each spontaneous radiative decay reaction, we know δA_{ul} since it is given by the NIST-ASD database along with the coefficients. The values of uncertainties are given in Table A.2. They are usually of the order of 10% of the Einstein coefficient.
  In addition, we know that the rate coefficient for each of the electron impact excitation reaction is also evaluated with a certain amount of uncertainty because of the fitting to an Arrhenius form. The uncertainty on these rate coefficients is around 1% for most reactions, with the worst case being of 7%.

Other sources of uncertainty can not be evaluated, and will therefore not be included in this analysis. They include the human error in the experimental results, and the cross sections in the CR model, which do not come with a measure of uncertainty. The assumptions for the CR model, such as assuming a Maxwellian EEDF, or the 0-D modelization, also introduce uncertainties that can not be quantified.

For each sample, we therefore build a new CR model with Einstein coefficients sampled within a normal distribution centered around the NIST-ASD values, and electron impact excitation rate coefficients sampled in a similar way. These new CR models work exactly in the same way as before, with the only difference being the values of the coefficients in the governing equation (Equation 2.65). The experimental intensities are also sampled within their uncertainty bounds. The sampling is performed by assuming the given bounds for each source of uncertainty correspond to a 95% interval for the value of interest.

We can therefore compute a map of the objective function, as the one obtained in Figure 4.1, and find the minimum. This minimum gives the location of the optimal electron temperature and density, for this sample. By repeating this procedure for a sufficient number of samples, we get a distribution of optimal plasma parameters.

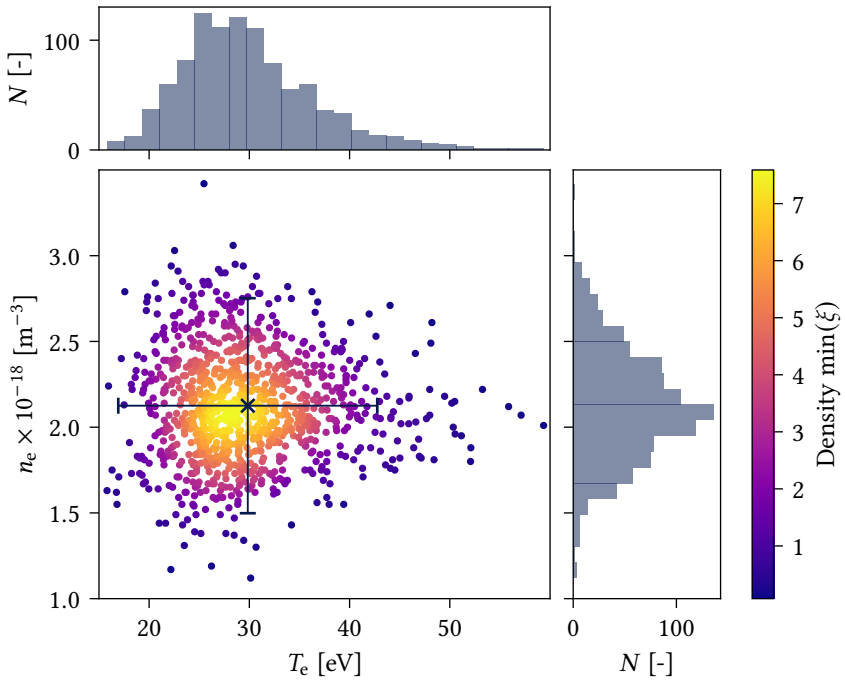

Figure 4.3: Distribution of ξ obtained with the Monte Carlo sampling method

In practice, the entire map of $\xi(T_e, n_e)$ is not computed for each sample. Instead, we minimize the objective function with a multivariable optimization algorithm based on the gradients method, to limit the number of evaluations needed to find a single minimum. This optimization algorithm is the Broyden-Fletcher-Goldfarb-Shanno algorithm, implemented in the `minimize` function of the `scipy` Python library [52]. This allows to reduce the number of evaluations of the objective function, but also to increase the resolution compared to a grid of fixed step.

The resulting samples are represented in Figure 4.3, obtained with 1000 samples, each time constructing the CR model and solving the minimization problem. The raw distribution of the sampled minima of ξ in the (T_e, n_e) plane is complemented by the marginal distribution function for each plasma parameter. The obtained distributions gives insight on the uncertainty on the optimal values. We get the sample averaged values $< \cdot >$ and uncertainties $\delta\cdot$ on the optimal parameters:

$$\left\langle T_e^* \right\rangle = 29.8 \text{ eV} \qquad \delta T_e^* = 12.9 \text{ eV} \tag{4.6}$$

$$\left\langle n_e^* \right\rangle = 2.1 \times 10^{18} \text{ m}^{-3} \qquad \delta n_e^* = 0.6 \times 10^{18} \text{ m}^{-3} \tag{4.7}$$

or a relative uncertainty of 28% for the electron density, and an uncertainty of 43% on the electron temperature. These uncertainties are computed as a 95% interval for the average value assuming a standard distribution, or $\delta X = 1.96 \cdot \text{STD}(X)$.

The Monte Carlo method was stopped after 1000 samples, because it proved to be sufficient to have converged statistical estimates of the average and standard deviation on the results, as

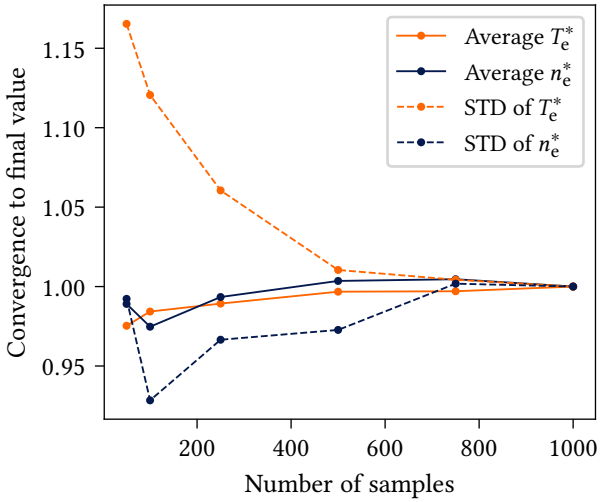

Figure 4.4: Convergence of the Monte Carlo sampling results with the number of samples

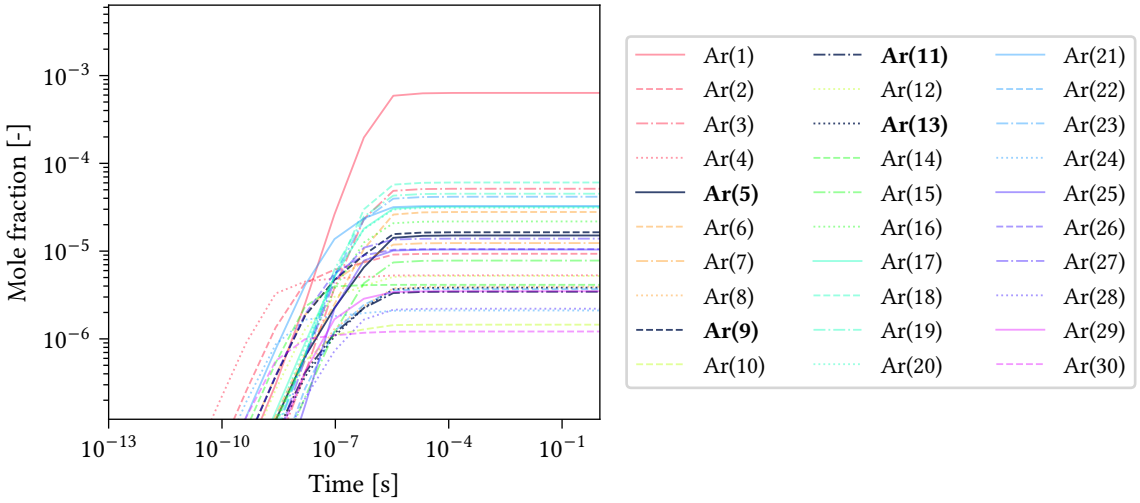

Figure 4.5: Kinetics until steady state, at the optimal point

shown in Figure 4.4. Doubling the number of samples from 500 to 1000 samples only changed the average values by 0.5%, and the standard deviations by 3%. From 750 to 1000 samples, no value changed by more than 0.5%. This is considered to be sufficiently converged knowing the level of uncertainty on the actual results.

4.4 Conditions at the optimal point

In this section, we review the predicted plasma conditions at the obtained optimal point.

Kinetics

At an electron temperature and density of T_e^* and n_e^*, the governing system of differential equations for the energy level populations follows the kinetics shown in Figure 4.5. In this

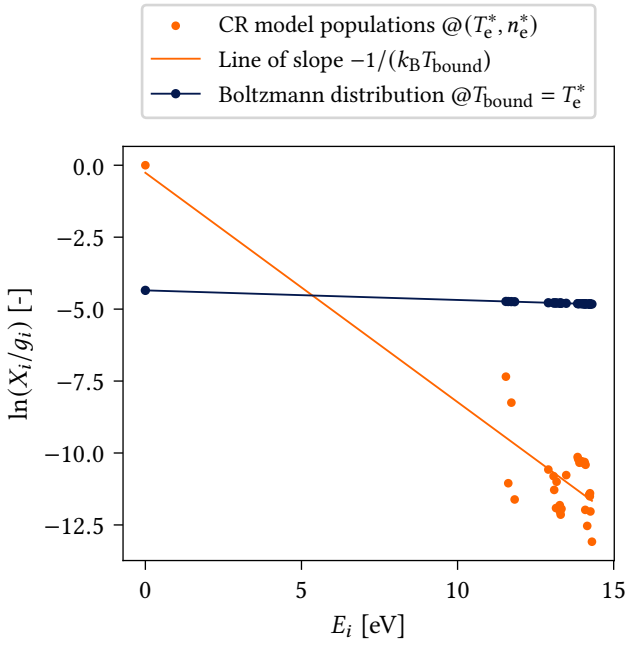

Figure 4.6: Boltzmann plot for the energy levels at the optimal point and comparison to the Boltzmann distribution if there was no radiation

figure, the upper levels for the lines of interest in this study are bolded, and their lines are in black. We see that due to the high rate coefficients needed to reach a configuration close to the experimental one, the Argon atoms are excited at a high enough rate for the chemistry to be considered instantaneous compared to the flow time scale (steady state reached after 10^{-5} s, compared to a flow timescale of 3×10^{-4} s). This confirms the choice to rely on the steady state for the computation of the synthetic line intensities.

Steady state energy level populations

At steady state, the energy level populations are represented in Figure 4.6 (orange). As discussed in Section 2.6, the observed scattering is due to the state of chemical non-equilibrium of the solution: we solve for the excitation of Argon by electrons at a very high temperature compared to the atoms themselves, and we assume the EEDF does not vary in the timescales considered here (the electrons stay at T_e^*). These electrons give part of their kinetic energy to excite the atoms. Simultaneously, the relatively fast radiative emissions lower the excitation level of the atoms. The steady state configuration, corresponding to a balance between these mechanisms, leads to the population densities represented by the orange dots on the Boltzmann plot. Their degree of excitation can be quantified by the slope of the best fitting line through these points (orange line in Figure 4.6). This slope corresponds to a temperature of 1.25 eV, which is not a kinetic temperature as defined by kinetic theory, but an *electronic temperature*, quantifying the energy of the *bound* electrons T_{bound}. It corresponds to the chemical equilibrium temperature that would lead to the closest population distribution, described by the orange line of slope $-1/k_B T_{bound}$.

In Figure 4.6, the CR model population results are compared to those obtained with the Boltz-

mann distribution, if the chemical equilibrium temperature was $T_{\text{bound}} = T_e^*$ (blue). If there was no radiative process, the equilibrium would be reached when the electron excitations and de-excitation would balance, leading to the blue (Boltzmann) distribution.

The difference in slope of the two lines illustrates the highly out-of-equilibrium conditions encountered in the observed plasma. In a low density such as DRAG-ON, the steady state is reached at a relatively low excitation level because of the efficiency of the radiative processes to lower the excitation level of the atoms. Because of the rate of radiative emissions, the plasma remains *cold* in the sense that it remains at a low excitation level.

4.5 Validity of the results

The results obtained in this chapter have to be interpreted with caution. The obtained electron temperature and density correspond to the values that minimize the difference between the results of the CR model and the experimental line intensities. They can only be assumed to correspond to the actual conditions in the facility under the strong assumption that the CR model is capable of accurately representing the conditions inside the facility. This must be confirmed through other means of measurement, and only in case of agreement can we more safely draw conclusions about the conditions in the facility. In this section, we discuss the validity of the obtained results, and the assumptions in the model that can have a great impact on the final values.

Comparison to invasive diagnostics

Parallel measurements made in the plasma plume in DRAG-ON by K. Tsoumpariotis [54] with invasive Langmuir and Faraday probes give much lower results for the electron temperature and density. For the same operating conditions of the PFG, they give an ion density (thus electron density) between 10^{14} and 10^{15} m^{-3}, and an electron temperature between 2 and 6 eV depending on the method used. These measurements are not directly comparable because they were not carried out at the same position. The OES measurements were made with an integrated line of sight through the transparent tube, while the invasive measurements were made 5 cm outside of the transparent tube, in the center of the plume for the Faraday probe, and at $r = 37$ mm for the Langmuir probe. The differences in electron densities and temperatures using invasive and non-invasive diagnostics methods are thus expected to be different because of the axial distance between the measurements. Indeed, the plasma is confined radially in the tube. From the outlet of the tube, the very mobile electrons can expand in the entire vacuum chamber, lowering their number density greatly. The electron temperature is also expected to decrease axially, since they give part of their kinetic energy through elastic and inelastic collisions. Particle-In-Cell simulations solving the Boltzmann equation for an axisymmetric plasma plume expansion [55] indeed predict an exponential decrease of the number density with the axial direction, of about an order of magnitude every 10 cm.

The electron densities and temperatures measured at these two axial positions therefore have the quality of evolving in the right direction (both decreasing axially). The orders of magnitudes between the results however suggest that there is an overestimation of the electron density and energy with OES, especially for the density.

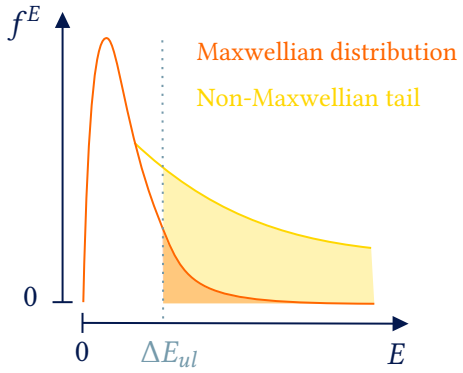

Figure 4.7: Maxwellian and non-Maxwellian tails and effect on the number of electrons participating to the excitation processes

Influence of CR model assumptions on the results

The results are the inputs to the CR model that allow to best fit the experimental intensities. This makes them very sensitive to the assumptions made while building the CR model. One assumption that is particularly reconsidered is the electron Maxwellian velocity distribution function. The model seems to show that for the emitting excited states to be close to the OES measured population ratios, we need a large number of high energy electrons. The net production rates of the governing equation (Equation 2.65) indeed consist of a weighted sum of radiative and collisional population and de-population processes. The steady state populations correspond to a balance between these processes. The results show that for the CR balance to stabilize in a configuration close to the experimental energy level population ratios, we need an important contribution from the electron excitation processes.

Assuming a Maxwellian EEDF, as it is done in this model, implies that the only way to increase this rate of energetic collisions, is to have a large fraction of very fast electrons (high T_e), and to have overall many electrons (high n_e). The obtained results under these constraints seem to be overestimated. This can be an indication that the constraints imposed by the Maxwellian assumption do not represent well reality. Indeed, high excitation rates can appear at much lower densities if the electrons have an energy distribution with a more populated tail. Only electrons with $E > \Delta E_{ul}$ can participate in the excitation processes. It is therefore the tail of the distribution that contains the electrons actually exciting the Argon atoms. If the tail of the distribution is non-Maxwellian, this can have a large impact on the excitation rates even for the same total number of electrons, since for a same total n_e, there is a larger fraction of *active* electrons. This is illustrated in Figure 4.7, showing how a non-Maxwellian tail can have an impact on the number of active electrons (area under the curve, over ΔE_{ul}).

Non-Maxwellian EEDFs are observed experimentally in low density plasmas [56, 57], confirming that this is a possible future line of research for a better understanding of the conditions in the DRAG-ON facility. However, the measurement of the EEDF is not straightforward, and often relies on other assumptions and models to obtain results. Langmuir probes are often used for EEDF measurements, but they rely on probe theories, and assume isotropy of the velocity distribution function in the state space [21]. Such measurements were carried out in DRAG-ON in parallel to this work [54], giving a non-Maxwellian EEDF that could be used as

an alternative for the CR model. Chai and Kwon [28] use such a coupled method for the calibration of their OES measurements. The EEDF is first measured with a Langmuir probe, and used for the computation of the rate coefficients of the CR model to which the OES measurements are compared to.

Validity of the uncertainty bounds

The confidence intervals obtained with the Monte Carlo sampling method reveal a large uncertainty on the final values for the electron temperature and density, of the order of 30% for n_e^*, and 40% for T_e^*. This is an expected result for OES, which can have error bounds going up to 100% of the measured values, even when care is taken about the EEDF considerations [28]. This is due to the large uncertainties on the coefficients representing the chemical processes in the CR model (Einstein and excitation rate coefficients).

The bounds on the final results obtained in the present work are therefore optimistic, by only considering the quantified sources of uncertainty. Depending on the database used for the construction of the CR model, large differences can be found in the cross sections for a same reaction (up to 50 or 100% difference, depending on the reaction), which would lead to different results. This was not included in the Monte Carlo sampling method, as the uncertainty on the cross sections were not included with Zatsarinny's results [37]. In addition to uncertainty on the cross sections, there could also be variability in the experimental values, for repeated measurements. By repeating the experiment a number of times at the same conditions, this variability in the intensities could be determined, adding a contribution to the uncertainty on the experimental intensities.

To reduce the uncertainty on the results, a complete covariance analysis could be carried out, to see which reaction coefficients participate the most in the total uncertainties. By identifying them, alternative Einstein coefficient or cross sectional data could be found with lower uncertainties for these particular reactions, therefore lowering the total uncertainty on the results for electron density and temperature.

4.6 Conclusion

This chapter provides a criterion for comparing the experimental line intensities to the CR model predicted line intensities. This criterion has been used as an objective function that, when minimized, determines the electron density and temperature that leads to the best fit of the experimental data. This minimization process has been carried out for enough samples to extract statistics about the distribution of the results.

The results show that the measured plasma emission spectrum corresponds best to excited state populations far from Boltzmann equilibrium. This justifies the need for a non-equilibrium CR model, as the one built in Chapter 2. However, the electron density and temperature that lead to these plasma conditions seem to be overestimated with the current model. This can be explained by the assumption that the electrons follow a Maxwellian velocity distribution, which is the basis for the computation of the excitation rate coefficients in the CR model, thus influences greatly the results. The actual velocity distribution of electrons therefore appears

to be out of kinetic equilibrium. A more accurate knowledge of the EEDF can be brought by Langmuir probe measurements or numerical simulations complementary to this work.

CHAPTER 5

Conclusion

The objective of this work was to develop and implement a non-invasive diagnostics method for the characterization of the Argon plasma flow of the DRAG-ON facility. The employed method is Optical Emission Spectroscopy, coupled with a Collisional-Radiative model for the prediction of the level population densities in chemical non-equilibrium conditions. The main research questions were to assess the degree of non-equilibrium of the DRAG-ON plasma, and to determine ways to improve the fidelity of the CR model if the usual assumptions showed to have shortcomings to model the rarefied plasma conditions.

To achieve this goal, the CR model first had to be implemented. This required the selection of relevant excitation and de-excitation reactions to include in the model, and the computation of rate coefficients for each of these reactions. The resulting CR model consists of a set of electron impact excitation/de-excitation reactions and radiative decay reactions (510 reactions in total) between the 31 excited states of Argon. Solving the resulting system of rate equations for a given set of plasma parameters yields the densities of each excited state, from which line intensities can be obtained. It was shown that, at the conditions fitting best the experimental emissions, using the steady state solutions of the rate equations is a valid assumption, as the chemical timescale appears to be smaller than the flow timescale. The key parameters and their effect on the population densities were also identified as being the electron temperature and density.

The experimental setup for OES measurements was then presented. This setup was calibrated for relative intensity measurements, giving a calibration curve that can be used for any future experiment carried out with the same optical instruments, provided no perturbing element is added on the optical path. The radiative signature of the Argon plasma generated by the PFG was then measured at different collecting optics heights. By relating the identified peaks to known transitions of Argon, usable line intensities could be integrated, giving a value of intensity comparable to those obtained with the CR model. The results did not verify repeatability of the measurements with the current setup. Measurements made at the same height, in the same PFG conditions, but separated by the manipulation of the collecting optics on the vertical rail appeared to be significantly different, demonstrating the sensibility of the measurements to external factors. The most probable cause is a slight misalignment of the optics after their manipulation. The spatial distributions of intensities measured during the first test campaign carried out in the context of this work therefore appear to be unusable. The framework for transforming the line-of-sight integrated intensities to a radial distribution was nevertheless discussed, as it is a natural evolution of the current work.

Finally, a criterion was provided to compare the experimental line intensities to the synthetic intensities predicted by the CR model. The comparison criterion is defined as a measure of

the error between the two sets of lines. A parametric minimization of this function therefore provides the electron temperature and density that minimize the discrepancy between the experimental and CR model results. Repeated evaluations of the minimum location for sampled CR model coefficients in their uncertainty bounds provide a measure of the uncertainty on the extracted plasma parameters T_e^* and n_e^*. This uncertainty sampling method incorporates all nonlinearities between the uncertainty sources and the results, but could be complemented with the inclusion of the uncertainties on the cross sections and on repeated measurements. At the optimal plasma conditions, the plasma is shown to be very far from chemical equilibrium, with the population distribution of excited states scattered far from the equilibrium conditions at the electron temperature.

The optimal electron temperature and density evaluated with this method appear to overestimate the actual conditions when comparing them to invasive diagnostics results performed in parallel to this work. This suggests that the current state of the CR model does not fully capture the chemical properties of the observed plasma. In order to best fit the experimental line intensities, the electron impact excitation rate coefficients must be large. With the current assumption on the electron energy distribution function, these high rates can only be reached with high electron temperatures and densities. A non-Maxwellian EEDF tail could also explain high rate coefficients, even for lower electron temperatures and densities. This suggests that the extremely low densities encountered in DRAG-ON do not allow the EEDF to follow the usual Maxwellian distribution. The probable difference between the actual and assumed EEDF could therefore be an explanation to the large electron densities and temperatures obtained with this first attempt at using the developed method.

Overall, this work provides a framework for the characterization of the rarefied plasma flow encountered in DRAG-ON with OES and CR modelling. The preliminary results obtained with the first measurements addressed in this work allowed to enhance the experimental setup, and to have a better understanding of the highly out-of-equilibrium conditions encountered in this facility. This will allow an adaptation of the CR model to the unique conditions of DRAG-ON. Ultimately, the method will allow more reliable non-invasive diagnostics of the plasma plume, that can be used to monitor the plasma conditions simultaneously to the testing of the ABEP intake efficiency, therefore contributing, to some extent, to the development of this promising technology.

Future work

The present work leaves room for future developments, both to enhance the experimental setup for reliability, and to increase the fidelity of the CR model. In this final section, we provide a method refinement strategy to obtain a robust method for the characterization of the DRAG-ON plasma, based on the developments and questions raised in the present work. The following sequence of actions could be undertaken, in order of priority:

1. Verification of the repeatability of the OES measurements with the new motorized experimental setup, by performing multiple measurements at each position. This will allow to test the robustness of the new setup, and quantify the unavoidable variability of the experimental results, which can be added as a source of uncertainty in the method. If

large variability is still observed, other ways of obtaining reliable measurements should be investigated before attempting any other improvement of the method.

2. Verification of the robustness of the method with different PFG conditions. For example, changing the coil current could show the impact of the magnetic field on the observed population densities. Similarly, the RF power of the PFG can be changed to see the impact on the excitation levels. Such tests would allow to see if the obtained results evolve in the expected direction, assessing the robustness of the method before going into refinements of the model.

3. Modification of the EEDF used for the rate coefficients computation. This new test EEDF can come from the Langmuir probe measurements or a numerical simulation in the phase space. The validity of the new results for the electron temperature and density with this new EEDF should then be checked with other means of measurements.

4. If important deviations are still encountered, other points can be changed to increase the fidelity of the CR model, such as the inclusion of ionization reactions. If the EEDF has a populated tail, this potentially increases the number of electrons capable of ionizing Argon.

These steps constitute the main lines of work. They would allow to have a more robust and reliable method for the determination of the electron density and temperature from OES measurements. Once these priorities have been addressed, further refinements can be carried out, such as

- Applying the Abel transform to a line-of-sight integrated intensity distribution, to obtain a radial distribution of intensities. From there, the comparison method can be repeated for each radial position to extract a radial distribution of the plasma parameters $T_e^*(r), n_e^*(r)$.

- Performing an absolute calibration of the optical setup, for example with a Tungsten wire of known spectral radiance, placed inside the chamber. This would provide absolute intensities, directly comparable to the CR model results without the need of taking ratios or normalizing, reducing the error propagation.

- Extending the range of experimental OES measurements by capturing the emissions more downstream, in the plume.

- Expanding the current 0-D model to a 1-D or 2-D model, taking into account the translation and expansion of the chemical reactor, as developed by Bocelli et al. [58]. If the results obtained with the modified CR model show a larger chemistry timescale, this step would be necessary, as instantaneous chemistry would no longer be a valid assumption.

- The uncertainty due to the variability of the cross sectional data in function of the database was not taken into account in the present uncertainty analysis. This could be done to see which reactions contribute the most to the final uncertainty.

References

[1] European Space Agency — ESA. *GOCE (Gravity field and steady-state Ocean Circulation Explorer)*. 2023. (Visited on 05/06/2023).

[2] Michael J. Drinkwater et al. 'GOCE: ESA's First Earth Explorer Core Mission'. In: *Space Science Reviews* 108.1/2 (2003), pp. 419–432.

[3] Nicholas Crisp et al. 'The benefits of very low earth orbit for earth observation missions'. In: *Progress in Aerospace Sciences* 117 (2020), p. 100619.

[4] JAXA | Japan Aerospace Exploration Agency. *Super Low Altitude Test Satellite (SLATS) "TSUBAME" has set a Guiness World Record*. 20th Dec. 2019. (Visited on 05/06/2023).

[5] ESA | European Space Agency. *VLEO for Telecommunications - Very Low Earth Orbits (VLEO) for Satellite Communications ARTES FPE*. 19th Mar. 2021. (Visited on 05/06/2023).

[6] T. Andreussi et al. 'The AETHER project: development of air-breathing electric propulsion for VLEO missions'. In: *CEAS Space Journal* 14.4 (2022), pp. 717–740.

[7] F. Romano et al. 'RF Helicon-based Inductive Plasma Thruster (IPT) Design for an Atmosphere-Breathing Electric Propulsion system (ABEP)'. In: *Acta Astronautica* 176 (2020), pp. 476–483.

[8] Tommaso Andreussi et al. 'Development and Experimental Validation of a Hall Effect Thruster RAM-EP Concept'. In: *The 35th International Electric Propulsion Conference*. Georgia Institute of Technology, USA, 12th Oct. 2017.

[9] Lake A. Singh and Mitchell L. R. Walker. 'A review of research in low earth orbit propellant collection'. In: *Progress in Aerospace Sciences* 75 (1st May 2015), pp. 15–25.

[10] T. Andreussi, E. Ferrato and Vittorio Giannetti. 'A review of air-breathing electric propulsion: from mission studies to technology verification'. In: *Journal of Electric Propulsion* 1.1 (15th Dec. 2022).

[11] Peng Zheng et al. 'A Comprehensive Review of Atmosphere-Breathing Electric Propulsion Systems'. In: *International Journal of Aerospace Engineering* 2020 (2020), pp. 1–21.

[12] Pietro Parodi. *Analysis and Simulation of an Intake for Air-Breathing Electric Propulsion Systems*. MA thesis. Università di Pisa, 2019.

[13] Pfeiffer Vacuum. *Vacuum technology, vacuum pumps and vacuum components by Pfeiffer Vacuum*. 2023. (Visited on 13/05/2023).

[14] ThrustMe. *ThrustMe: Advanced In-Orbit Propulsion Systems*. 2023. (Visited on 13/05/2023).

[15] VKI | von Karman Institute for Fluid Dynamics. *Dual-chamber for RArefied Gases and ON-ground testing (DRAG-ON)*. (Visited on 06/06/2023).

[16] VKI | von Karman Institude for Fluid Dynamics. *1200 KW Induction Plasmatron*. (Visited on 06/06/2023).

[17] Benoit Bottin et al. 'The VKI Plasmatron Characteristics and Performance'. In: *RTO AVT Course on Measurement Techniques for High Enthalpy and Plasma Flows, published in RTO EN-8* (2000).

[18] Bernd Helber et al. 'Ablation of Carbon Preform In the VKI Plasmatron'. In: *43rd AIAA Thermophysics Conference*. New Orleans, Louisiana, 25th June 2012.

[19] George Potrivitu et al. 'A Review of Low-Power Electric Propulsion Research at the Space Propulsion Centre Singapore'. In: *Aerospace* 7.6 (2020), p. 67.

[20] Valery Godyak and Vladimir Demidov. 'Probe measurements of electron-energy distributions in plasmas: what can we measure and how can we achieve reliable results?' In: *Journal of Physics D* 44.23 (15th June 2011), p. 233001.

[21] Francis F. Chen and Jane P. Chang. *Lecture Notes on Principles of Plasma Processing*. 1st ed. Springer New York, 2003.

[22] James B. Scoggins et al. 'Mutation++: MUlticomponent Thermodynamic And Transport properties for IONized gases in C++'. In: *SoftwareX* 12 (2020).

[23] Giacomo Dimarco et al. 'An efficient numerical method for solving the Boltzmann equation in multidimensions'. In: *Journal of Computational Physics* 353 (15th Jan. 2018), pp. 46–81.

[24] G. J. Tallents. *An Introduction to the Atomic and Radiation Physics of Plasmas*. 1st ed. Cambridge University Press, 2018.

[25] M. V. Malyshev and Vincent M. Donnelly. 'Determination of electron temperatures in plasmas by multiple rare gas optical emission, and implications for advanced actinometry'. In: *Journal of vacuum science & technology* 15.3 (1997), pp. 550–558.

[26] S Iordanova and I Koleva. 'Optical emission spectroscopy diagnostics of inductively-driven plasmas in argon gas at low pressures'. In: *Spectrochimica Acta Part B: Atomic Spectroscopy* 62.4 (1st Apr. 2007), pp. 344–356.

[27] Sarah Siepa et al. 'On the OES line-ratio technique in argon and argon-containing plasmas'. In: *Journal of Physics D* 47.44 (2014), p. 445201.

[28] Kil-Byoung Chai and Duck-Hee Kwon. 'Optical emission spectroscopy and collisional-radiative modeling for low temperature Ar plasmas'. In: *Journal of Quantitative Spectroscopy & Radiative Transfer* 227 (2019), pp. 136–144.

[29] Bariselli et al. 'Characterization of an Air-Xenon Operated Electric Thruster Plume through Optical Emission Spectroscopy'. In: *9th International Workshop on Radiation of High Temperature Gases for Space Missions*. Azores, Portugal, 2022.

[30] J. A. Bittencourt. *Fundamentals of Plasma Physics*. 3rd ed. Springer Science, 2004.

[31] Iain D. Boyd and Thomas E. Schwartzentruber. *Nonequilibrium Gas Dynamics and Molecular Simulation*. 1st ed. Cambridge University Press, 2017.

[32] Pascal Chabert and Nicholas Braithwaite. *Physics of Radio-Frequency Plasmas*. 1st ed. Cambridge University Press, 24th Feb. 2011.

[33] Leanne Pitchford et al. 'LXCat: an Open-Access, Web-Based Platform for Data Needed for Modeling Low Temperature Plasmas'. In: *Plasma Processes and Polymers* 14.1-2 (2016).

[34] Alexander Kramida et al. *NIST Atomic Spectra Database*. 2022. (Visited on 04/05/2023).

[35] Santiago Alvarez. 'A cartography of the van der Waals territories'. In: *Dalton Transactions* 42.24 (2013), pp. 8617–8636.

[36] A. V. Phelps. 'The application of scattering cross sections to ion flux models in discharge sheaths'. In: *Journal of Applied Physics* 76.2 (1994), pp. 747–753.

[37] Oleg Zatsarinny, Yu Wang and Klaus Bartschat. 'Electron-impact excitation of argon at intermediate energies'. In: *Physical Review A* 89.2 (2014).

[38] Oleg Zatsarinny and Klaus Bartschat. 'The B-Spline R-matrix method for atomic processes: application to atomic structure, electron collisions and photoionization'. In: *Journal of Physics B* 46.11 (2013).

[39] Ben Slimane Tarek. *A Xenon Collisional Radiative Model for Electric Propulsion Application: Determining the electron temperature in a Hall-effect Thruster*. MA thesis. KTH Royal Institute of Technology, 2020.

[40] Michael Bass et al. *Handbook of Optics, Third Edition Volume I: Geometrical and Physical Optics, Polarized Light, Components and Instruments*. 3rd ed. Vol. 1. McGraw Hill Education, 2009.

[41] ThorLabs. *Mounted Achromatic Doublets, AR Coated: 400 - 1100 nm*. 2023. (Visited on 14/05/2023).

[42] ThorLabs. *SM1D12C - SM1 Graduated Ring-Actuated Iris Diaphragm*. 2023. (Visited on 14/05/2023).

[43] Ocean Insight. *QP200-2-VIS-BX*. 2023. (Visited on 14/05/2023).

[44] Ocean Insight. *Applied Spectral Knowledge | Spectrometers | Ocean Insight*. 2023. (Visited on 14/05/2023).

[45] Hamamatsu. *IR-enhanced CCD image sensors | S11510 series*. 2016.

[46] Charles De Izarra and Jean-Michel Gitton. 'Calibration and temperature profile of a tungsten filament lamp'. In: *European Journal of Physics* 31.4 (June 2010), pp. 933–942.

[47] AMETEK Land. *LANDCAL Blackbody Temperature Calibration Sources*. 2023. (Visited on 15/05/2023).

[48] Präzisions Glas & Optik GmbH. *BOROFLOAT | Transmission curve | Thickness 2mm*. (Visited on 15/05/2023).

[49] ThorLabs. *Mounted UV Fused Silica Reflective ND Filters*. 2023. (Visited on 15/05/2023).

[50] Iouli E. Gordon et al. 'The HITRAN2020 molecular spectroscopic database'. In: *Journal of Quantitative Spectroscopy & Radiative Transfer* 277 (2021), p. 107949.

[51] Abraham Savitzky and Marcel J. E. Golay. 'Smoothing and Differentiation of Data by Simplified Least Squares Procedures.' In: *Analytical Chemistry* 36.8 (1964), pp. 1627–1639.

[52] Pauli Virtanen et al. 'SciPy 1.0: fundamental algorithms for scientific computing in Python'. In: *Nature Methods* 17.3 (2019), pp. 261–272.

[53] Daniel D. Hickstein et al. 'A direct comparison of high-speed methods for the numerical Abel transform'. In: *Review of Scientific Instruments* 90.6 (2019), p. 065115.

[54] Konstantinos Tsoumpariotis. *Characterization of a Rarefied Plasma Beam by Invasive Methods*. MA thesis. von Karman Institute for Fluid Dynamics, 2023.

[55] Shelley D. Minteer et al. 'On electron boundary conditions in PIC plasma thruster plume simulations'. In: *Plasma Sources Science and Technology* 28.3 (2019), p. 034004.

[56] Takamasa Hori et al. 'Measurement of non-Maxwellian electron energy distributions in an inductively coupled plasma'. In: *Applied Physics Letters* 69.24 (1996), pp. 3683–3685.

[57] Seolhye Park et al. 'Characteristics of a non-Maxwellian electron energy distribution in a low-pressure argon plasma'. In: *Journal of the Korean Physical Society* 64.12 (2014), pp. 1819–1827.

[58] Stefano Boccelli et al. 'Lagrangian diffusive reactor for detailed thermochemical computations of plasma flows'. In: *Plasma Sources Science and Technology* (2019).

[59] Roman V. Kochanov et al. 'HITRAN Application Programming Interface (HAPI): A comprehensive approach to working with spectroscopic data'. In: *Journal of Quantitative Spectroscopy & Radiative Transfer* 177 (2016), pp. 15–30.

[60] Oleg A. Alduchov and Robert E. Eskridge. 'Improved Magnus Form Approximation of Saturation Vapor Pressure'. In: *Journal of Applied Meteorology* 35.4 (1996), pp. 601–609.

APPENDIX A

Argon Energy Levels and Spectral Lines

A.1 Electronic levels

The energy levels of Argon are referred to throughout this project. In this appendix, Table A.1 provides a list of the 31 energy levels of the neutral Argon atom with an energy level lower than the ionization energy. This table provides the levels in the local index notation, the configuration-term notation according to NIST-ASD [34], and the Paschen notation frequently used in the literature. The degeneracy g [-] and the energy E [eV] relative to the ground state are given for each level.

Additional information on the configuration-term notation

- In the configuration column, the common configuration for lower electrons ($1s^2\ 2s^2\ 2p^6\ 3s^2$) is not shown for compacity.
- For all excited states, a first coupling term is indicated in the configuration, and corresponds to the coupling between the orbital angular momentum and spin angular momentum of a single electron, as discussed in subsection 2.3.1.
- An additional symbol (°) is added to account for parity. The symbol appears for odd cases, when $(-1)^{\sum_i l_i} = -1$.
- For all excited states, the term column denotes the coupling between the total angular momentum of a first electron, and the orbital angular momentum of the second electron. The value between square brackets is the sum of J_1 and l_2^*, and the exponent before the brackets is still $(2m_s^* + 1)$ but for the second electron.

A.2 Spectral lines

This appendix contains the list of emission lines used in the CR model of this project. They consist of all allowed transitions by quantum mechanics with an upper energy level lower than the ionization energy, and a quantified Einstein A_{ul} coefficient with a relative error lower than 25%. These transitions are listed in Table A.2, with data extracted from the NIST-ASD database [34]. The last column gives an upper bound for the uncertainty on the Einstein coefficient for each transition. The wavelengths are Ritz wavelengths (theoretical vacuum wavelengths, as opposed to experimental air wavelengths).

Table A.1 List of energy levels for the Argon atom, sorted by energy, from NIST-ASD [34]

Local index	Paschen	Configuration	Term	J	g [-]	E [eV]
0	gs	$3p^6$	^1S	0	1	0
1	$1s_5$	$3p^5(^2P^\circ_{3/2})4s$	$^2[3/2]^\circ$	2	5	11.548
2	$1s_4$	$3p^5(^2P^\circ_{3/2})4s$	$^2[3/2]^\circ$	1	3	11.624
3	$1s_3$	$3p^5(^2P^\circ_{1/2})4s$	$^2[1/2]$	0	1	11.723
4	$1s_2$	$3p^5(^2P^\circ_{1/2})4s$	$^2[1/2]$	1	3	11.828
5	$2p_{10}$	$3p^5(^2P^\circ_{3/2})4p$	$^2[1/2]$	1	3	12.907
6	$2p_9$	$3p^5(^2P^\circ_{3/2})4p$	$^2[5/2]$	3	7	13.076
7	$2p_8$	$3p^5(^2P^\circ_{3/2})4p$	$^2[5/2]$	2	5	13.095
8	$2p_7$	$3p^5(^2P^\circ_{3/2})4p$	$^2[3/2]$	1	3	13.153
9	$2p_6$	$3p^5(^2P^\circ_{3/2})4p$	$^2[3/2]$	2	5	13.172
10	$2p_5$	$3p^5(^2P^\circ_{3/2})4p$	$^2[1/2]$	0	1	13.273
11	$2p_4$	$3p^5(^2P^\circ_{1/2})4p$	$^2[3/2]$	1	3	13.283
12	$2p_3$	$3p^5(^2P^\circ_{1/2})4p$	$^2[3/2]$	2	5	13.302
13	$2p_2$	$3p^5(^2P^\circ_{1/2})4p$	$^2[1/2]$	1	3	13.328
14	$2p_1$	$3p^5(^2P^\circ_{1/2})4p$	$^2[1/2]$	0	1	13.480
15	$3d_{12}$	$3p^5(^2P^\circ_{3/2})3d$	$^2[1/2]^\circ$	0	1	13.845
16	$3d_{11}$	$3p^5(^2P^\circ_{3/2})3d$	$^2[1/2]^\circ$	1	3	13.864
17	$3d_{10}$	$3p^5(^2P^\circ_{3/2})3d$	$^2[3/2]^\circ$	2	5	13.903
18	$3d_9$	$3p^5(^2P^\circ_{3/2})3d$	$^2[7/2]^\circ$	4	9	13.979
19	$3d_8$	$3p^5(^2P^\circ_{3/2})3d$	$^2[7/2]^\circ$	3	7	14.013
20	$3d_7$	$3p^5(^2P^\circ_{3/2})3d$	$^2[5/2]^\circ$	2	5	14.063
21	$3d_6$	$3p^5(^2P^\circ_{3/2})5s$	$^2[3/2]^\circ$	2	5	14.068
22	$3d_5$	$3p^5(^2P^\circ_{3/2})5s$	$^2[3/2]^\circ$	1	3	14.090
23	$3d_4$	$3p^5(^2P^\circ_{3/2})3d$	$^2[5/2]^\circ$	3	7	14.099
24	$3d_3$	$3p^5(^2P^\circ_{3/2})3d$	$^2[3/2]^\circ$	1	3	14.153
25	$3d_2$	$3p^5(^2P^\circ_{1/2})3d$	$^2[5/2]^\circ$	2	5	14.214
26	$3d_1$	$3p^5(^2P^\circ_{1/2})3d$	$^2[3/2]^\circ$	2	5	14.234
27	$2s_5$	$3p^5(^2P^\circ_{1/2})3d$	$^2[5/2]^\circ$	3	7	14.236
28	$2s_4$	$3p^5(^2P^\circ_{1/2})5s$	$^2[1/2]^\circ$	0	1	14.241
29	$2s_3$	$3p^5(^2P^\circ_{1/2})5s$	$^2[1/2]^\circ$	1	3	14.255
30	$2s_2$	$3p^5(^2P^\circ_{1/2})3d$	$^2[3/2]^\circ$	1	3	14.304

Table A.2 Transitions used in the CR model, from NIST-ASD [34]

#	λ_{ul} [nm]	**Upper**	**Lower**	A_{ul} [s^{-1}]	Uncertainty [%]
1	86.68	30	0	3.13E+08	18
2	86.9754	29	0	3.50E+07	25
3	87.6058	24	0	2.70E+08	18
4	87.9947	22	0	7.70E+07	25
5	104.822	4	0	5.32E+08	1
6	106.666	2	0	1.32E+08	2
7	667.7281	14	2	2.36E+05	10
8	696.543	13	1	6.40E+06	7
9	706.7217	12	1	3.80E+06	10
10	714.7041	11	1	6.30E+05	10
11	727.2935	13	2	1.83E+06	7
12	738.398	12	2	8.50E+06	10
13	747.1164	11	2	2.20E+04	10
14	750.3868	14	4	4.50E+07	10
15	751.4651	10	2	4.00E+07	10
16	763.5105	9	1	2.45E+07	10
17	772.376	8	1	5.20E+06	7
18	772.4207	13	3	1.17E+07	7
19	794.8176	11	3	1.86E+07	10
20	800.6156	9	2	4.90E+06	18
21	801.4785	7	1	9.30E+06	10
22	810.3692	8	2	2.50E+07	7
23	811.5311	6	1	3.30E+07	10
24	826.4521	13	4	1.53E+07	7
25	840.8209	12	4	2.23E+07	7
26	842.4647	7	2	2.15E+07	7
27	852.1441	11	4	1.39E+07	10
28	866.7943	8	3	2.43E+06	10
29	912.2967	5	1	1.89E+07	10
30	919.4638	29	5	1.76E+06	25
31	922.4498	9	4	5.00E+06	10
32	929.1532	28	5	3.26E+06	25
33	935.4218	8	4	1.06E+06	10
34	965.7786	5	2	5.40E+06	10
35	978.4502	7	4	1.47E+06	10
36	1047.0053	5	3	9.80E+05	18
37	1047.8034	22	5	2.44E+06	25
38	1095.0726	30	9	3.96E+05	25
39	1107.8868	25	7	8.30E+05	25
40	1139.3703	28	8	2.22E+06	25
41	1144.1832	29	9	1.39E+06	25
42	1146.7545	26	8	3.69E+05	25
43	1148.8108	5	4	1.90E+05	25
44	1166.8709	26	9	3.76E+06	25
45	1171.9487	24	7	9.52E+05	25

APPENDIX B

Images of the Experiments

This appendix contains pictures of the experimental setup, both for the OES measurements in DRAG-ON (Section B.1) and the calibration (Section B.2). These pictures can help visualize the layouts used in practice. Section B.3 contains pictures of the working PFG, showing the glow of the plasma flow.

B.1 OES setup in DRAG-ON

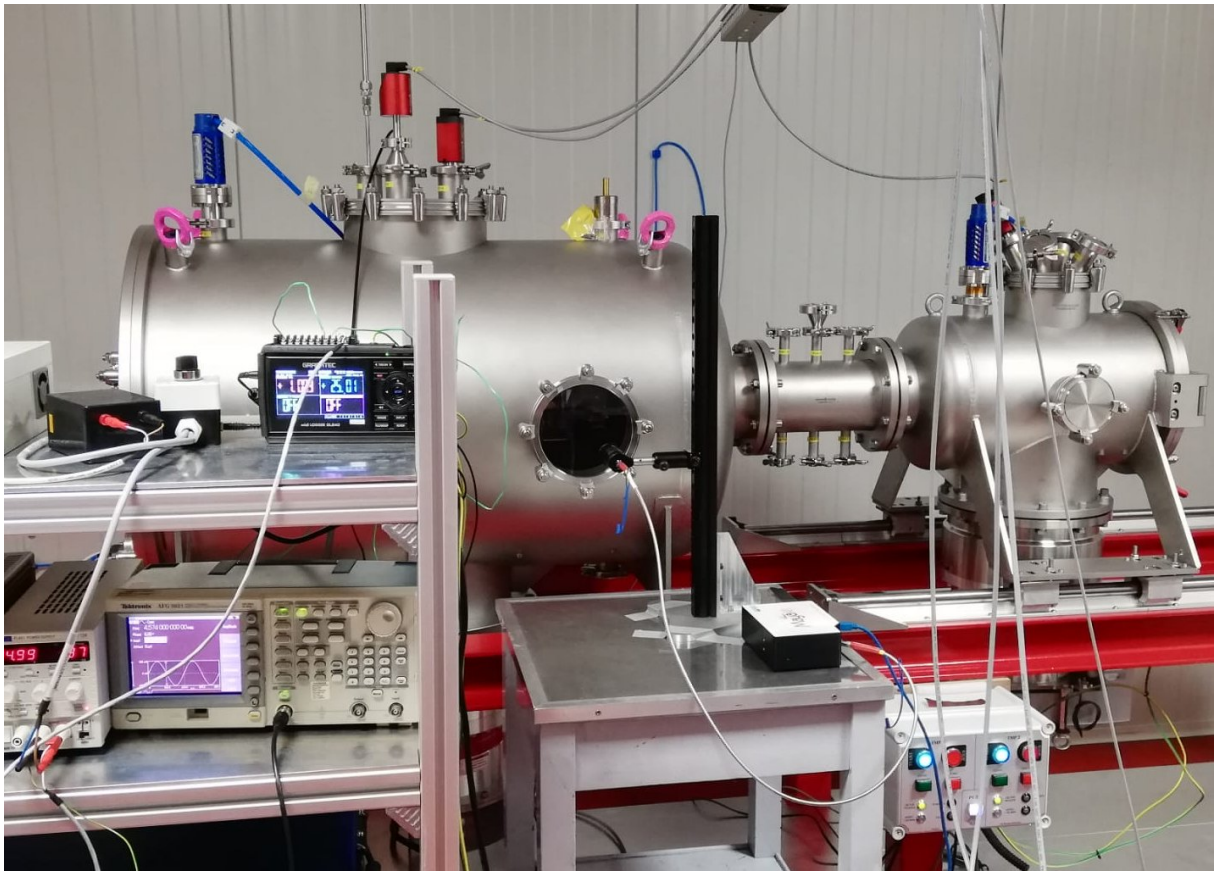

Figure B.1: OES setup in DRAG-ON

B.2 Setup for the calibration of the optical assembly

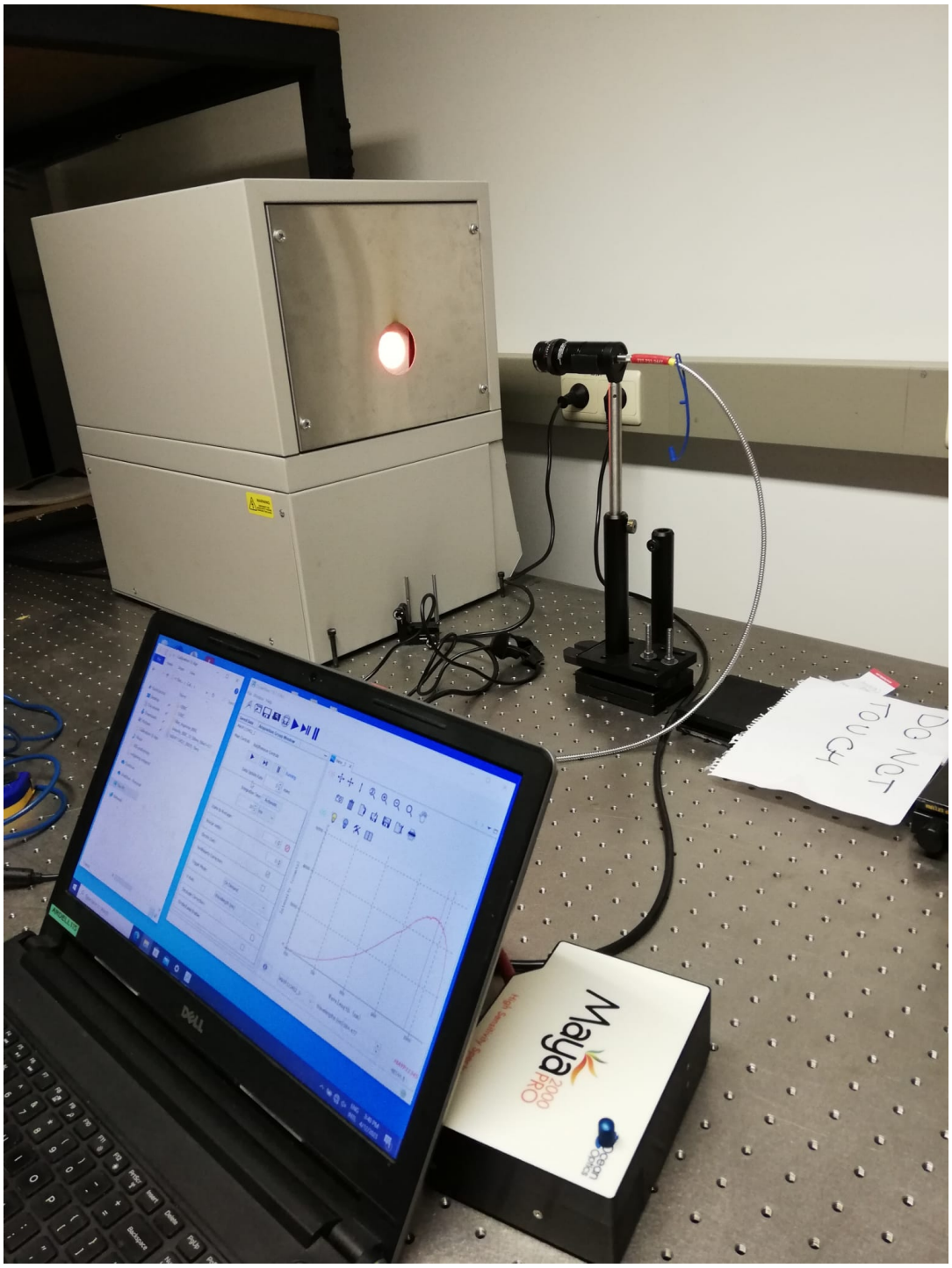

Figure B.2: Setup for the calibration of the instruments

B.3 Plasma flow

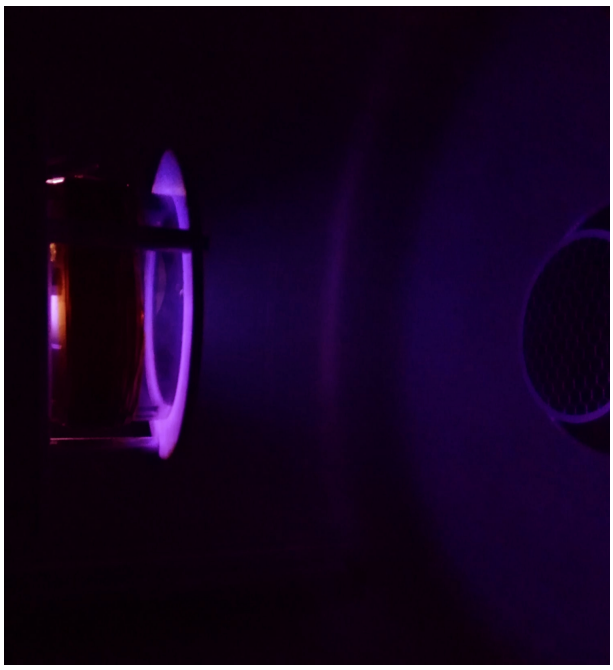

Figure B.3: Argon plasma flow generated by the PFG (view from the side window)

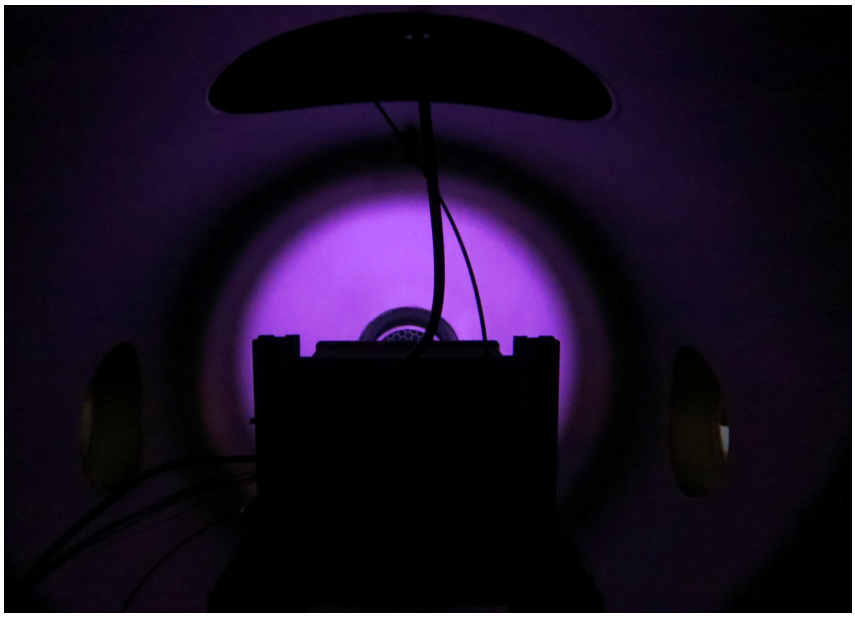

Figure B.4: Reflection of the plasma light emissions on the chamber walls (view from the back)

B.4 Experimental setup with the motorized vertical rail

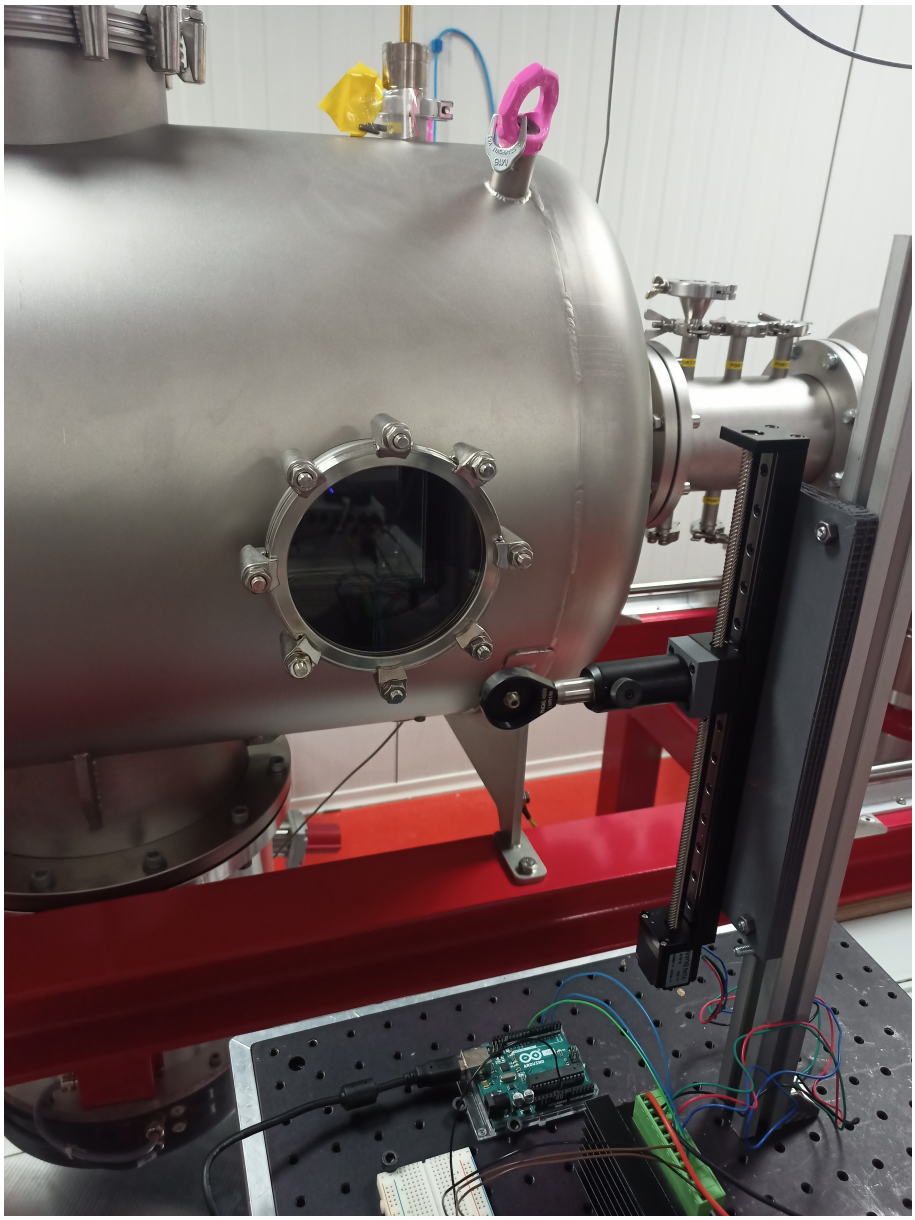

Figure B.5: Motorized rail for future experiments. It has two degrees of freedom (horizontal and vertical), and is manipulated with a graphical user interface.

APPENDIX C

Water Vapor Absorption

In this appendix, we see how the HITRAN database [50] can be used for the computation of the spectral transmittance of humid air for given atmospheric conditions. This is an important step in the calibration of the optical setup, as water vapor can have an impact on the measured intensities of certain lines in the infrared region. If the air slice thickness, or the atmospheric conditions are different between the measurements in the DRAG-ON facility and the calibration setup, the difference in absorption can have an impact on the measured line intensities at certain wavelengths.

The HITRAN Application Programming Interface (HAPI) [59] is used to generate the transmittance spectrum of humid air in function of the length of the optical path through air, and the atmospheric conditions. Since the spectral range of interest is between 600 and 1000 nm, only absorption by water vapor is significant and therefore considered in the transmittance calculations. HAPI is able to extract a variety of spectroscopic parameters from the HITRAN database directly and store them in local files. This was done for H_2O and all its isotopologues between 600 and 1000 nm. The data contains the Einstein coefficients for all transitions of the H_2O molecule. Because of its vibrational and rotational energy levels, the number of transitions is very large (120710 lines in the considered spectral range). In addition to the Einstein coefficients, the HITRAN database also provides data about how each of these lines are broadened in several diluents.

The HAPI function `absorptionCoefficient_Voigt` is used to exploit all the downloaded data, to extract the absorption coefficient $\alpha'_\lambda(\lambda)$ [cm^2/molecule] at all wavelengths in the considered range, in function of the atmospheric conditions (pressure, temperature, and water vapor partial pressure). Since, in the laboratory, the partial pressure of water vapor is not given directly, it has to be computed from the relative humidity RH [-] according to

$$P_{H_2O} = \mathrm{RH} \cdot P_{\mathrm{sat}} \tag{C.1}$$

with P_{sat} [Pa] the saturation pressure at the recorded ambient temperature, given by an empirical equation from Alduchov and Eskridge [60]

$$P_{\mathrm{sat}} = 610.94 \cdot \exp\left\{\frac{17.625T}{243.04 + T}\right\} \tag{C.2}$$

where T [°C] is the ambient temperature, in degrees Celcius for this equation.

The transmittance can finally be computed with

$$T_\lambda(\lambda) = \exp\{-\alpha_\lambda L\} \tag{C.3}$$

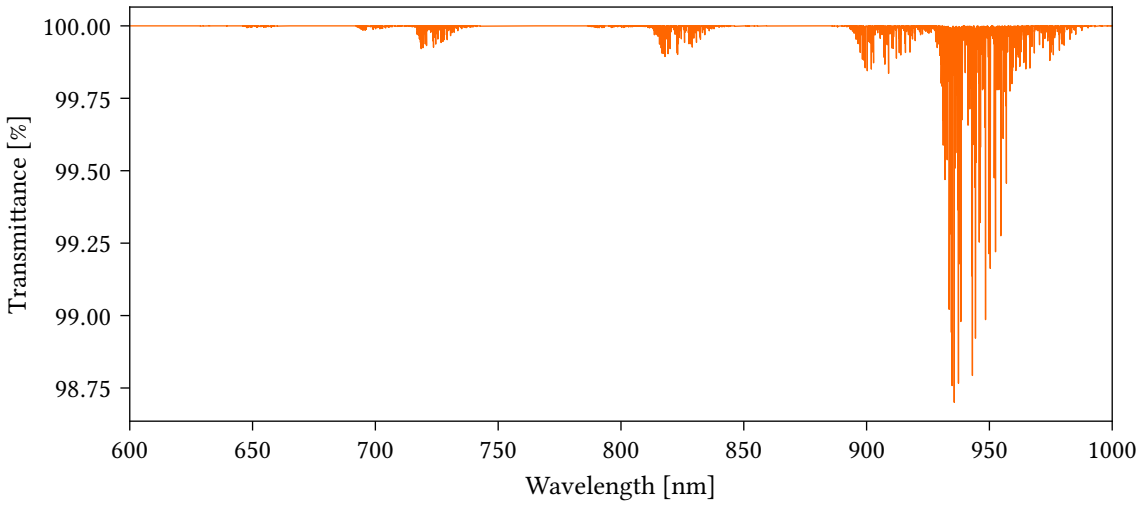

Figure C.1: Transmittance of 21 cm of air, at $P = 985$ mbar, $T = 25°C$ and RH= 40%, between 600 and 1000 nm.

with L [m] the length of the optical path through air, and α_λ [cm^{-1}] the absorption coefficient, where the unit change is done with

$$\alpha_\lambda = \alpha'_\lambda \cdot n_{H_2O} = \alpha'_\lambda \cdot \frac{P_{H_2O}}{k_B T} \cdot 10^{-6} \tag{C.4}$$

with, here, the temperature T in Kelvin. The results for the spectral transmittance are given in Figure C.1, for the ambient conditions measured in the calibration laboratory. In this figure, it can be seen that at these wavelengths, the absorption remains reasonably low. Maximum absorption is found around 950 nm, with the strongest lines absorbing 1.25% of the signal. This remains low, but the effect would increase exponentially if the distance between the DRAG-ON window and the collecting optics was to increase in future layouts of the experimental setup.